



N64-31012
(ACCESSION NUMBER)
127
(PAGES)
CR-54106
(NASA CR OR TMX OR AD NUMBER)

(THRU)
1
(CODE)
25
(CATEGORY)

BEHAVIOR OF THIN ALKALI METAL LAYERS ON REFRACTORY METAL SUBSTRATES

by

L. W. Swanson, R. W. Strayer, C. J. Bennette, and E. C. Cooper

prepared for

NATIONAL AERONAUTICS AND SPACE ADMINISTRATION

OTS PRICE

CONTRACT NAS 3 - 2596

XEROX

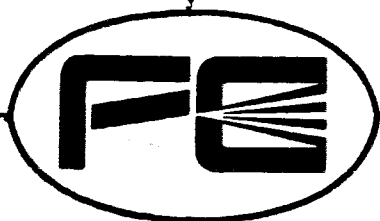
\$

4.00 FS

MICROFILM

\$

0.75 MF



Field Emission Corporation

McMinnville, Oregon

NASA CR-54106

FINAL REPORT

BEHAVIOR OF THIN ALKALI LAYERS
ON
REFRACTORY METAL SUBSTRATES

by

L. W. Swanson
R. W. Strayer
C. J. Bennette
E. C. Cooper

Prepared for

NATIONAL AERONAUTICS AND SPACE ADMINISTRATION

3 June 1963 to 2 June 1964

CONTRACT NAS3-2596

Technical Management
NASA Lewis Research Center
Cleveland, Ohio
Electric Propulsion Office
Y. E. Strausser

FIELD EMISSION CORPORATION
Melrose Avenue at Linke Street
McMinnville, Oregon

TABLE OF CONTENTS

INTRODUCTION	1
OBJECTIVES and DESCRIPTION OF WORK	1
SUMMARY OF RESULTS	1
Studies of Surface Kinetics by Field Emission Techniques	1
Electrical Breakdown Studies	2
Sputtering Studies	3
PAPERS	3
 STUDIES OF CESIUM SURFACE KINETICS BY FIELD EMISSION TECHNIQUES	 5
EXPERIMENTAL TECHNIQUES	5
Field Emission Measurements and Monitoring	5
Description of Experimental Tubes	6
Experimental Procedure	10
WORK FUNCTION VARIATION WITH CESIUM COVERAGE	11
Cesium on Molybdenum, Tungsten, and Rhenium	14
Results from Two Emitter Tube	14
Results from Probe Tube	19
Effect of Oxygen	21
Discussion of Results	24
EFFECT OF TEMPERATURE ON WORK FUNCTION	31
Results on Molybdenum	31
Discussion of Results	32
RESULTS OF THERMAL DESORPTION OF CESIUM FROM VARIOUS REFRACTORY METALS	 33
Cesium Neutral Desorption	34
Cesium Ion Desorption	36
The Effect of Oxygen	38
RESULTS OF SURFACE DIFFUSION OF CESIUM ON VARIOUS REFRACTORY METALS	 43
Recent Results on Molybdenum	45
Discussion of Results	46
THE EFFECT OF ELECTRIC FIELD ON THE EQUILIBRIUM DISTRIBUTION OF CESIUM	 52
Results on Molybdenum and Tungsten	52
Discussion of Results	55
EFFECT OF FIELD ON THERMAL DESORPTION	56
Results on Tungsten	58
Discussion of Results	64
 ELECTRICAL BREAKDOWN STUDIES	 68
EXPERIMENTAL PROCEDURES	68
CURRENT-VOLTAGE MEASUREMENTS	68
Stable Pre-Breakdown Currents	68
Unstable Pre-Breakdown Currents	75
Maximum Currents Preceding Electrical Breakdown	76

TABLE OF CONTENTS, Cont'd.

TRANSITION RADIATION	77
PROTRUSION GROWTH STUDIES	81
SPUTTERING STUDIES BY FIELD ION MICROSCOPY	85
INTRODUCTION	85
Review	85
Application of Field Ion Microscopy to Sputtering Studies	87
EXPERIMENTAL TUBE AND TECHNIQUES	89
Ion Microscope Design	89
Ion Gun Design	89
Procedure	92
PRELIMINARY RESULTS	95
CONCLUSIONS	100
REFERENCES	101
APPENDIX I	105
SOURCE OF MOVEMENT OF SPHERICAL ELECTRODE	105
APPENDIX II	108
SOURCE OF MOVEMENT OF PLANAR ELECTRODE	108
APPENDIX III	110
LIST OF SYMBOLS	110

LIST OF ILLUSTRATIONS

Figure 1.	Diagram of Cs-W two-emitter tube.	7
Figure 2.	Front view diagram of field emission microscope for investigation of cesium and oxygen on tungsten. A, cesium source; B, oxygen source (heatable platinum crucible containing copper oxide); C, emitter assembly; D, electrical connection to conductive coating; E, anode ring; F, cesium reservoir; G, secondary cesium source.	8
Figure 3.	Diagram of "probe tube" which is capable of measuring field emission currents from single crystallographic planes. A, guard ring; B, suppressor grid support; C, collector; D, platinum anode containing a 2.5 mm hole and coated with a fluorescent screen; E, emitter assembly; F, cesium source; G, heatable inner tube for depositing cesium onto source; H, cesium reservoir.	9
Figure 4.	Equilibration sequence showing initial dosage (top) where emitter and shank are half covered, pseudo-equilibration (center) where emitter is covered but shank is not, and final equilibration (bottom) where both emitter and shank are completely and uniformly covered.	12
Figure 5.	Principal field emission pattern changes for cesium adsorption on molybdenum.	15
Figure 6.	Principal field emission pattern changes for cesium adsorption on tungsten.	16
Figure 7.	Principal field emission pattern changes for cesium adsorption on rhenium.	17
Figure 8.	Field emission work function as a function of average cesium atom density on tungsten. Present data from the two-emitter tube are compared with earlier results of Taylor and Langmuir whose atom density at the minimum work function has been normalized to agree with the present value of 1.9×10^{14} atoms/cm ² .	18

Figure 9.	Average work function and work function of the (100) plane as functions of cesium adsorbed on tungsten. Work function of (100) plane obtained from probe tube.	20
Figure 10.	Field emission work function and equilibration temperature as functions of average cesium atom density for clean tungsten and for two degrees of underlying oxygen coverage.	22
Figure 11.	Principal field emission pattern changes for cesium adsorption on tungsten initially covered with a partial chemisorbed layer of oxygen. Tip orientation same as Figure 6.	23
Figure 12.	Work function-cesium atom density data of Figure 8 plotted according to equation 17.	30
Figure 13.	Desorption time t vs $1/T$ for a small coverage increment near $\sigma = 1.17 \times 10^{14}$ atoms/cm ² for cesium on tungsten where the shank was not completely equilibrated.	35
Figure 14.	Variation of neutral desorption energy vs coverage for cesium on tungsten utilizing the $\phi - \sigma$ relationship of Figure 8.	37
Figure 15.	Desorption temperature vs coverage for cesium from tungsten at various underlying oxygen coverages, heating at 60 second intervals.	39
Figure 16.	Work function vs heating for 60 second intervals at the indicated temperatures for oxygen on tungsten.	41
Figure 17.	Typical field emission patterns showing the thermal desorption of oxygen initially deposited on tungsten at 77°K. These patterns were selected from a sequence of patterns that were taken after tungsten emitter had been heated to successively higher temperatures for 60 second periods.	42
Figure 18.	Variations in pattern and work function caused by 60 second heating of a cesium covered substrate at indicated temperatures. Substrate was initially covered with oxygen ($\phi_{ow} = 5.65$ ev) and heated to 493°K.	44

Figure 19.	Variation of $F_d(\theta, T)$ (see equation 47) with fractional monolayer coverage at various temperatures.	51
Figure 20.	Variation of the ratio of cesium coverage at the emitter tip ϕ_t and shank ϕ_s with applied field F .	54
Figure 21.	Data of Figure 20 plotted according to equation 49.	57
Figure 22.	Potential energy diagram for quasi-metallic (i.e., non-ionic) adsorption in the presence of an applied field. The $M+A^+$ curve is an image potential (dashed line) which is altered by the field so as to form a Schottky saddle to the right of the $M+A$ ground state curve. When $V_I - \phi$ is small or negative the ionic curve may be the ground state curve at x_0 and thus lead to ionic adsorption. No polarization effects have been included in the diagram.	59
Figure 23.	Progressive pattern changes during field desorption at a cesium coverage of 0.7×10^{14} atoms/cm ² ($\phi = 2.70$ ev) on a (100) oriented tungsten substrate at 113°K and desorbing field of 41 Mv/cm. Photo (a) taken at $T = 0$.	60
Figure 24.	Field F for onset of ionic desorption at approximately 100°K and work function ϕ as functions of cesium coverage.	61
Figure 25.	Patterns and work functions of the initial and final points used in determining the variation of desorption energy with field. Initial and final cesium coverages are 2.9 and 2.7×10^{14} atoms/cm ² respectively.	63
Figure 26.	Least squares fit of equation 53 to data of Table VI. Dashed line shows variation of E_P^F according to equation 50. Values of x_s calculated according to equations 52 and 54.	66
Figure 27.	Electrical breakdown study tube with variable spacing electrode: A, field emission microscope; B, cesium ampule; C, heatable section of in-seal; D, spherical electrode; E, plane electrode; F, stainless steel bellows.	69

Figure 28.	Electrodes in molybdenum electrical breakdown tube showing molybdenum cup used as cathode shield and enlarged envelope. Other parts of the tube are the same as those shown in Figure 27.	70
Figure 29.	Fowler-Nordheim plots of I-V data obtained at the indicated electrode spacings for an ambient cesium pressure of 2×10^{-6} torr.	72
Figure 30.	Fowler-Nordheim plots of I-V data for both polarities of field at the same gap spacing.	74
Figure 31.	Fowler-Nordheim plot of current-voltage data from clean tungsten electrodes. A represents point where transition radiation was first detected on the anode. At B the radiation has increased in intensity, while the anode has reached a temperature of 970°K . At C the radiation is still visible against an incandescent background (1320°K).	78
Figure 32.	Field emission patterns indicating the growth of protrusions: (A), initial pattern, $I = 10 \mu\text{a}$, $V = 10 \text{ kv}$; (B), pattern after heating at 1600°K for 20 minutes with a positive field of 140 Mv/am at the emitter surface, $I = 10 \mu\text{a}$, $V = 3.4 \text{ kv}$.	82
Figure 33.	Completed field ion microscope with ion gun. (A) Ion gun, (B) Faraday collector, (C) Emitter.	90
Figure 34.	Schematic diagram of xenon ion gun, used in xenon ion sputtering studies.	91
Figure 35.	Exploded view of ion gun. (A) Ion Source (B) Einzel lens.	93
Figure 36.	Helium ion image of a field evaporated tungsten emitter, voltage 14.85 kv .	94
Figure 37.	Tungsten emitter after slight xenon sputtering. Voltage 14.85 kv . Ion beam enters from left.	96
Figure 38.	Tungsten image after sputtering with xenon and helium ions with energies to 10 kv , and slight field evaporation. Voltage 13.50 kv . Ion beam enters from left,	97

- Figure 39. Tungsten image after sputtering, roughly 10^5 impacts at 1 kv energy. A, Ion image immediately after sputtering. B, After small amount of field evaporation. C, Field evaporation of 10 atom layers. D, After removal of 100 atomic layers. Ion beam enters from left. 98
- Figure 40. Tungsten image after sputtering with neutrals with the image field on. A, Ion image before sputtering. B, After roughly 10^3 impacts at 10 kv energy. C, Field evaporation of 2 atomic layers. D, Additional 2 layers. Ion beam enters from left. 99
- Figure 41. a) Cutaway view of tungsten electrode voltage breakdown tube showing, in exaggerated form, the initial position of the spherical electrode (solid line) and the position (dotted line) after movement. 106
- b) Cutaway view of molybdenum tube.

LIST OF TABLES

Table I.	Values of Various Substrate Work Functions at Zero Cesium Coverage ($\sigma = 0$), the Work Function Minimum ($\sigma = \sigma_m$) and the Highest Coverage Investigated ($\sigma = \sigma_\infty$).	14
Table II.	Polarizabilities of Adsorbed Cesium as Determined by Equations (13) and (15).	28
Table III.	Work Function Change $\Delta\phi$ with Temperature for Cesium on Molybdenum.	32
Table IV.	Comparison between Cesium Ion and Neutral Desorption Energies from O-W.	40
Table V.	Variation of the Activation Energy and the Diffusivity Constant of Surface Diffusion with Cesium Coverage on a Molybdenum Substrate.	45
Table VI.	Variation of E_p^F and $\log \gamma_s$ with F in the Coverage Range $\sigma = 2.9$ to 2.7×10^{14} atoms/cm ² .	64
Table VII.	Geometry Changes Due to Heating.	74

INTRODUCTION

OBJECTIVES and DESCRIPTION OF WORK

The general objectives of the work being performed on the present contract are to conduct a research program on the behavior of thin alkali layers on refractory substrates, and from this to obtain fundamental knowledge applicable to solution and control of voltage breakdown across vacuum gaps between alkali-coated electrodes. The work has been divided into three general areas: (1) studies of the surface kinetics of various adsorbate/substrate combinations by field emission techniques when such parameters as temperature, adsorbate coverage, and applied field are varied; (2) an investigation of prebreakdown gap currents and electrical breakdown conditions between clean and cesium-coated refractory electrodes as functions of such parameters as applied voltage, surface electric field, cesium coverage, ambient cesium pressure within the gap, and environmental conditions; and (3) investigation of individual xenon ion sputtering events on clean tungsten by means of field ion microscopy and of cesium ion sputtering of cesium-coated tungsten by field electron microscopy.

SUMMARY OF RESULTS

Reviews of work done on the problems listed above previous to the present contract are given in the final reports for Contracts NASr-19 and NASw-458.^{1, 2} Progress made under the present contract includes the following.

Studies of Surface Kinetics by Field Emission Techniques

Work function dependence upon relative cesium coverage has been determined by field emission techniques for Cs on W, Mo and Re. For these substrates the work function minimums are approximately the same, about 1.50 ± 0.05 ev; likewise the work functions for high coverages are nearly identical, about 1.82 ± 0.03 ev. Variation of average work function versus absolute surface concentration has been measured for cesium on tungsten and is found to agree in shape with earlier thermionic data of Taylor and Langmuir³; however, the surface concentration at the minimum was measured to be 1.9×10^{14} atoms/cm², substantially lower than previously reported values. The work function of the (100) plane of tungsten has been measured and found to differ considerably from the average work function at low coverages, but to approach the latter at high coverages. The presence of oxygen on a tungsten or molybdenum substrate lowers the work function for most cesium coverages (to as low as 1.0 ev at the minimum) and reduces the surface coverage required to attain minimum work function. The dependence of work function upon substrate temperature has

been measured for cesium on molybdenum and found to be an order of magnitude higher than and opposite in sign to the temperature dependence of clean molybdenum; a typical value is $\Delta \phi / \Delta T = -1.5 \times 10^{-4}$ eV/°K for a coverage of 0.1 monolayer. Many of the above results are interpreted in terms of the Helmholtz equation and the mutual depolarization model.

The effect of an electric field upon the equilibrium cesium coverage on an emitter tip was investigated and found to be appreciable, with fields of the order of 10 Mv/cm changing the surface coverage by a factor of two in some cases. The effect may be explained by consideration of the magnitudes of field-dependent terms of the chemical potential at different points on the emitter surface.

The desorption energy for cesium ions from tungsten with a cesium coverage of 2.8×10^{14} atoms/cm² was measured as a function of applied field; it varied from 0.79 eV at 0 field to 0.29 eV at 59 Mv/cm. The desorption field as a function of coverage at constant emitter temperature was also measured; the field is highest at the work function minimum, as expected. The zero field desorption energy for cesium ions from molybdenum was measured and is 2.2 ± 0.1 eV, in reasonable agreement with theory. Thermal desorption of cesium from oxygen-covered tungsten has been investigated further; the results indicate that oxygen increases the thermal desorption activation energy for neutral cesium atoms.

Diffusion rates of cesium on molybdenum have been measured for coverages in the neighborhood of the coverage corresponding to the work function minimum; the results show that the high equilibration temperature at θ_{\min} as measured earlier¹ is not due to an increase in the surface diffusion activation energy, but to a decrease in the diffusivity constant. Many of the surface diffusion results obtained so far, including the existence of two phases, can be interpreted in terms of a model which treats the cesium coating as a localized lattice gas with lateral interactions.

Electrical Breakdown Studies

It has been established that the pre-breakdown current between tungsten electrodes is field emission in nature for currents ranging from 1.0×10^{-10} to 5.0×10^{-6} amperes, for voltages from 1.5 to 30.0 kv, cesium coverages from 0 to more than one monolayer, ambient cesium pressures up to 2.0×10^{-6} torr, clean substrate temperatures from 300°K to 1100°K, electrode spacings from 1.5 to 10.0 mils, and for both polarities of the gap. The origin of these currents has been shown to be surface irregularities where enough localized enhancement of the gross field can be realized to account for appreciable field emission current.

In addition, the pre-breakdown currents between clean molybdenum electrodes were determined under ultrahigh vacuum conditions for electrode

gap spacings from 1.0 to 10 mils and for various degrees of surface roughness. The field emission nature of the gap current was established for currents from 1.0×10^{-10} to 5.0×10^{-5} amperes independent of gap spacing.

As the initial gap current was increased by increasing the gross field, instabilities in the form of a steady increase in current at a constant applied voltage were found to occur. Some of these instabilities could be associated with electrode movement due to the electrostatic stress between electrodes. Despite this problem, current densities of more than 1.0×10^7 amp/cm² and fields up to 6.9×10^7 volts/cm were measured in the molybdenum electrode tube over a wide range of enhancement factors for cesium-free electrodes. In this special case breakdown is a cathode-initiated process related to the resistive heating of the tip of a surface protrusion at very high current densities.

A brief study of the growth of protrusions was made. It has been found that under certain conditions of electric field and temperature, protrusions can be induced to grow on field emission tips. This leads to changes in the geometrical field factor, β , which cause localized enhancement leading to an observed increase in current at a constant voltage. Other investigations have shown that growth of protrusions does occur on gross surfaces under high fields.

Visible radiation in the form of a luminous blue-white spot was detected on the anode at current levels where the field emission I(V) characteristics remained stable and reproducible. This radiation has been identified as optical transition radiation, and is shown not to be a factor contributing to the voltage breakdown process.

Sputtering Studies

Field ion pattern photographs of xenon ion bombardment of a tungsten tip give evidence of xenon atom burial within the tungsten lattice and show extensive damage in the $\{11\}$ regions. The ion patterns also show some indications of focusing effects, and of gross surface roughening and target shape changes.

PAPERS

The following papers covering various portions of past and present work are in various stages of publication:

"Field-Emission Investigation of Thermal Desorption and Surface Diffusion of Cesium on Tungsten," by L. W. Swanson, R. W. Strayer, F. M. Charbonnier, and E. C. Cooper; published as NASA Contractor Report CR-22 (January 1964).

"Visible Radiation from Metal Anodes Preceding Electrical Breakdown," by Carol J. Bennette, Lynwood W. Swanson, and Richard W. Strayer; to be published in the Journal of Applied Physics as a Communication to the Editor.

"The Variations of Work Function with Cesium Coverage on Molybdenum, Tungsten, and Rhenium Substrates," by L. W. Swanson, R. W. Strayer, and F. M. Charbonnier; to be published in the Proceedings of the Twenty-Fourth Annual Conference on Physical Electronics.

"The Effect of Electric Field on Adsorbed Layers of Cesium on Various Refractory Metals," by L. W. Swanson, R. W. Strayer, and F. M. Charbonnier; submitted to the Journal of Physics and Chemistry of Solids.

Papers were also presented at the following professional meetings:

1963 Summer Meeting in the East of the American Physical Society: Buffalo, New York; 24-26 June 1963.

Tenth Annual Field Emission Symposium; Baldwin-Wallace College, Berea, Ohio; 4-6 September 1963.

Twenty-Fourth Annual Conference on Physical Electronics; Massachusetts Institute of Technology, Cambridge, Massachusetts; 25-27 March 1964.

The support given by NASA for the work reported in these papers and the presentation thereof is gratefully acknowledged.

STUDIES OF CESIUM SURFACE KINETICS BY FIELD EMISSION TECHNIQUES

EXPERIMENTAL TECHNIQUES

Field Emission Measurements and Monitoring

The application of field emission microscopy to studies of surfaces have been described in the literature.^{4, 5} The field emission techniques utilized in these investigations have been described in detail previously;^{1, 2} only a brief resume need be given here.

Measurements of the field emission current I as a function of applied voltage V enables one to obtain the work function ϕ of the adsorbate-coated surface and the geometrical ratio β of the electric field F at the emitter surface and the applied voltage. If the resulting I - V data are plotted in the form $\log_{10} I/V^2$ versus $10^4/V$, the slope m of the resulting straight line is, from the Fowler-Nordheim law of field emission,

$$m = \frac{-2.83 \times 10^3 \phi^{3/2}}{\beta} . \quad (1)$$

For a clean surface of known work function ϕ_s is determined directly from equation 1, and the electric field is then given by $F = \beta V$ for any applied voltage V . The work function of a coated surface is obtained from

$$\phi = \phi_s \left(\frac{m}{m_s} \right)^{2/3} , \quad (2)$$

where ϕ_s and m_s are the work function and slope corresponding to the clean surface and ϕ and m are the work function and slope for the coated surface.

The presence, migration, and desorption of the adsorbate are detected and measured through observation of the occurrence and time rate of resulting changes in the field emission pattern. To avoid alteration of the processes under study due to effects of the high electric field required for field emission, the voltage necessary for field emission is applied to the tube in the form of very short pulses at low duty factor, and the field emission pattern is then viewed as a motion picture. This technique⁵ minimizes the perturbing effect of the viewing field on the event under study and allows almost complete freedom in the selection both of the tip temperature and of the magnitude and polarity of the dc voltage gradient which, in addition to pulsed viewing field, may be applied at the tip surface.

Description of Experimental Tubes

The construction of the field emission microscopes employed in this investigation was standard⁴ except for modifications to permit deposition of cesium onto the field emitter made of the desired substrate at a controllable and measurable rate. The temperatures of the emitter and cesium source were controlled by an electronic servo-circuit described elsewhere². Pattern viewing was accomplished by pulse techniques to eliminate any field effects. In order to compare the relative work function ϕ versus adsorbate coverage σ curves for two different substrates, a tube was designed with two emitter assemblies such that both emitters saw an atomic beam of pure cesium of known attenuation (Figure 1). For studying the effect of oxygen a single emitter tube (Figure 2) was employed with an additional oxygen source consisting of "in situ" formed copper oxide contained inside a heatable platinum bucket which liberates pure oxygen when heated to 720°K. A "probe tube" utilized in this work is shown in Figure 3 and is similar to one used previously by Young and Müller⁶.

The $\phi - \sigma$ relationship for cesium on tungsten was determined in the two-emitter tube by employing the cesium detector D of Figure 1 mounted on axis with the source and two emitters so as to measure the cesium flux intercepted by the latter. The cesium detector consisted of a hot tungsten disc (temperature of 1100°K) located at the center of a cylindrical molybdenum collector which was held at -22 volts with respect to the heated disc. In this fashion, the portion of the cesium beam allowed to strike a known area of the heated disc through a small aperture in the collector was completely surface ionized, and from the total ionic charge measured at the collector it was possible to determine the surface density of atoms intercepted by the disc. To calculate the fraction of the beam intercepted by each emitter an r^{-2} attenuation factor was employed for the source to emitter geometry of this tube. The latter was confirmed experimentally by comparing the $\phi - \sigma$ relationships of the two emitters when both consisted of tungsten. Because of the smallness of the emitter and its distance from the source, the cesium beam impinging on the upper half of the emitter was effectively parallel.

Briefly, the probe tube shown in Figure 3 consisted of a field emitter cathode and a platinum disc anode (D) covered by a fluorescent screen with a 2.5 mm diameter hole in the center. The emitter consisted of a single crystal made from zone-melted wire so oriented that emission from the desired crystal plane was in the center of the emission pattern; precise alignment of the pattern with the probe hole was accomplished by a weak magnetic field. In the present study in which electrical data indicated an emitter radius of 1500 Å, the projection of the probe hole back onto the emitter yields a surface area 86 Å in diameter. For a perfectly hemispherical tip 1500 Å in radius the uppermost atom layer on the (100) plane can have a diameter as large as 137 Å; thus, when the probe is well-centered on the (100) plane, it accepts emission from that plane only.

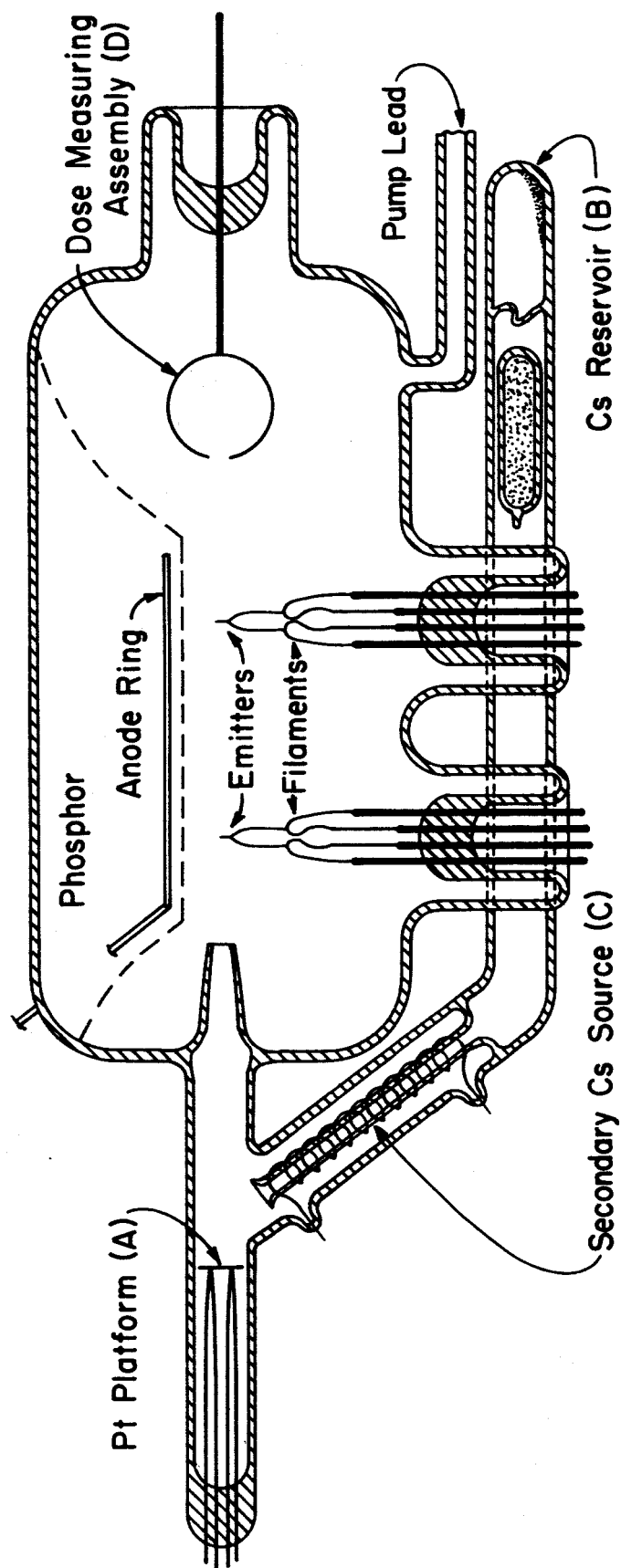


Figure 1. Diagram of Cs-W two-emitter tube.

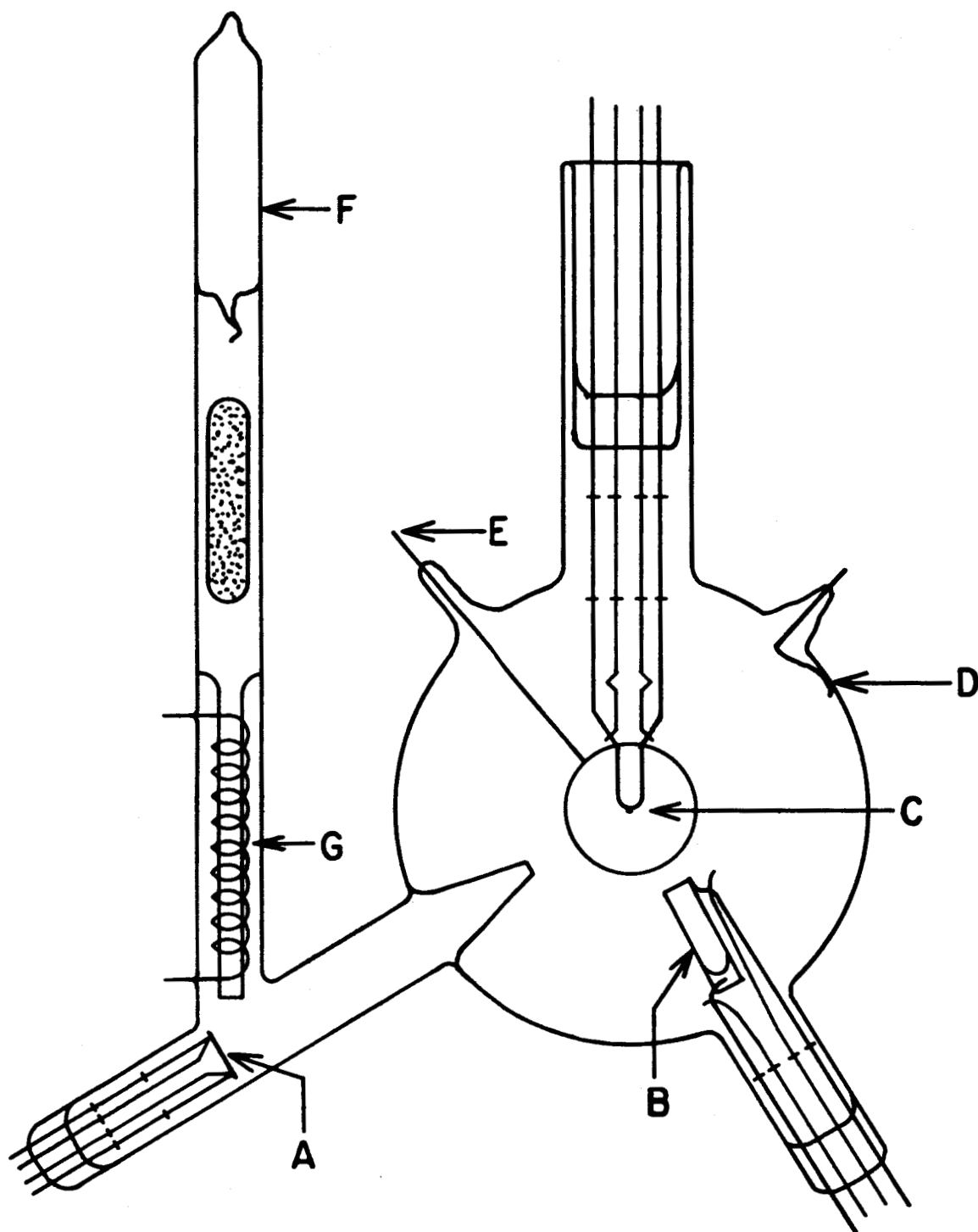


Figure 2. Front view diagram of field emission microscope for investigation of cesium and oxygen on tungsten. A, cesium source; B, oxygen source (heatable platinum crucible containing copper oxide); C, emitter assembly; D, electrical connection to conduction coating; E, anode ring; F, cesium reservoir; G, secondary cesium source.

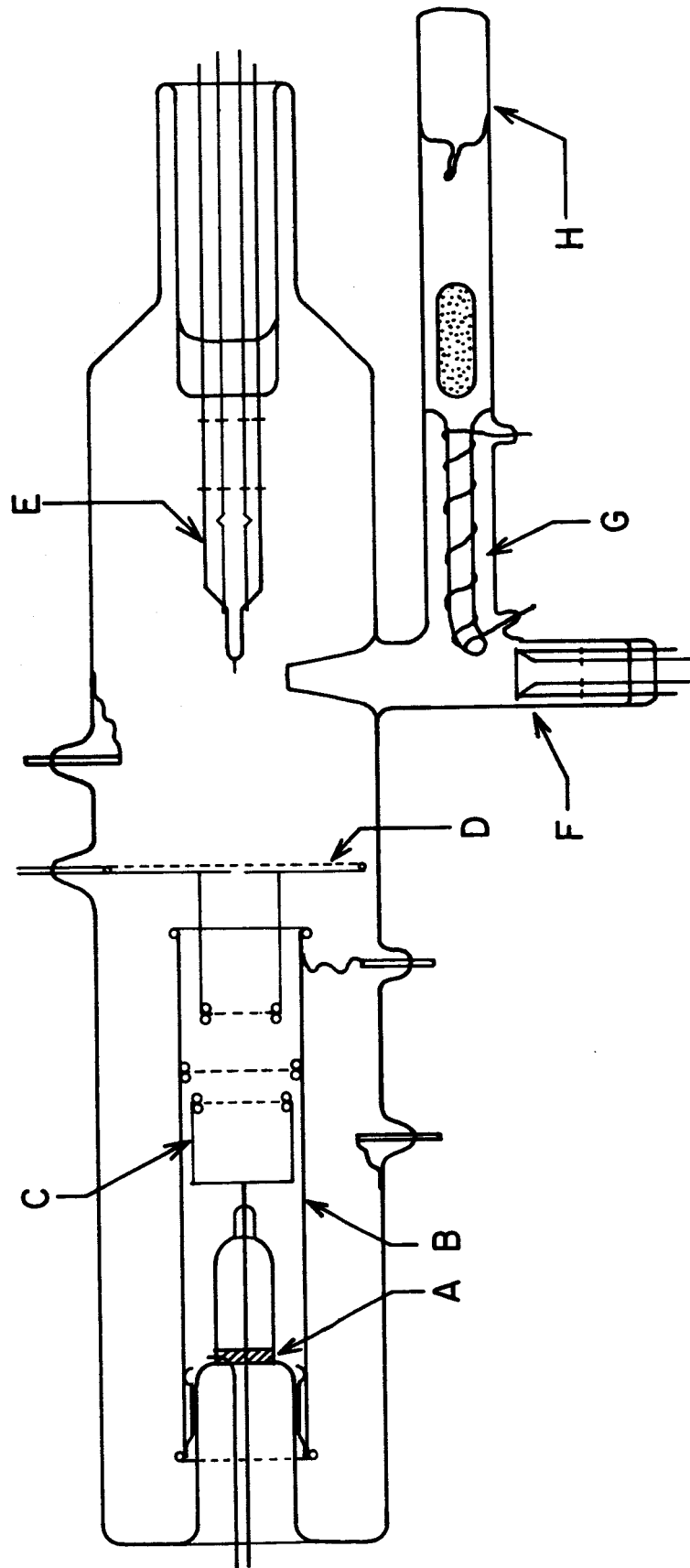


Figure 3. Diagram of "probe tube" which is capable of measuring field emission currents from single crystallographic planes. A, guard ring; B, suppressor grid support; C, collector; D, platinum anode containing a 2.5 mm hole and coated with a fluorescent screen; E, emitter assembly; F, cesium source; G, heatable inner tube for depositing cesium onto source; H, cesium reservoir.

The cesium source (see Figure 1) in each tube consisted of a thin resistively heated platinum disc (A) onto which a substantial amount of cesium could be condensed. The cesium was initially vacuum distilled into a break-off capsule (B) which was normally broken after the tube was sealed off from the vacuum system. After driving the cesium into the inner nozzle (C) by heating the cesium reservoir and connecting arm, the tube was placed in a cryostat cooled by liquid nitrogen. The inner nozzle (C) was then used as a convenient secondary reservoir from which cesium could be periodically sublimed onto the primary source (A), by merely resistively heating the platinum wire surrounding the nozzle.

The combination of an appendage molybdenum or titanium getter bulb and liquid nitrogen cooling of the entire tube envelope provided a vacuum sufficient to allow the tubes to remain several days with no apparent contamination of the emitter even after several oxygen depositions when studying the effect of oxygen; also, immersing the tubes in liquid nitrogen extends the lower limit of the temperature to 77°K and eliminates undesirable loss of tube impedance which occurs at room temperature due to cesium mobility on the tube walls.

Experimental Procedure

The general procedure followed in determining the $\phi - \sigma$ relationship in the probe and two emitter tube was to (1) dose the emitter with the emitter held at 77°K where only immobile adsorption can occur, (2) heat the emitter such that the cesium spreads uniformly and "equilibrates" the entire surface of the emitter after each dose, and (3) make a work function determination from the tube I-V characteristics. In the case of the probe tube both the partial current from the (100) plane and the total current were measured in step (3) and the corresponding work functions determined. In this manner the work function of the clean(100) plane of tungsten was determined to be 4.72 eV, in agreement with earlier measurements.⁵ When measurements of the absolute cesium coverage were being determined, the cesium detector of the tube shown in Figure 1 was employed to measure the amount of cesium per unit area intercepted by each emitter after the dose.

It should be pointed out that several assumptions, most of which are reasonably justifiable, are inferred by the foregoing procedure. Firstly, we assumed the condensation coefficient was unity at 77°K over the range of coverages investigated. Langmuir³ has shown this assumption to be valid at 300°K between 0 and 1 monolayer coverage, therefore, it is reasonable to expect a condensation coefficient of unity even beyond one monolayer since in our case $T = 77^{\circ}\text{K}$. Secondly, thermal desorption of the adsorbed cesium during the heating period required for equilibration over the uncovered portion of the emitter was assumed to be negligible. It can be shown that the average distance y an ad-atom will migrate before being thermally desorbed is related to the difference in activation energy of desorption E_a° and migration E_d° by the following expression,

$$y \approx a \exp (E_a^0 - E_d^0) / 2kT, \quad (3)$$

where a is the site separation. The activation energies of desorption and migration for cesium on tungsten have been determined¹ so that it was possible to choose the proper temperature to give complete equilibration without excessive desorption.

The average change in the surface coverage $\Delta \sigma$ of both the shank and the emitting area due to a dose R atoms per unit area of a cesium beam striking the emitter surface may be determined from the ratio of their respective cross-sectional to total area, assuming that the beam is essentially parallel. For the shank, which can be represented by a cone of half-angle α_c , this ratio is $\frac{\cos \alpha_c}{\pi}$; since $\alpha_c \leq 5^\circ$ for emitters used in this work, $\cos \alpha_c \geq 0.996$ and thus

$$\Delta \sigma \approx \frac{R}{\pi} . \quad (4)$$

For the emitting area, which may be represented by a portion of a sphere with an area between 1/2 and 1/4 of the surface area of a sphere, this ratio is between 1/4 and 1/5; therefore, $\Delta \sigma \leq R/4$. Thus, according to Figure 4, there is a tendency for the cesium concentration over the emitting area of the tip to increase with equilibration time due both to the longer times required for equilibration of the shank and to the higher equilibrated coverage of the shank. Since the emitting area is very small compared to the area of the emitter shank, its coverage will also approach R/π at equilibrium. In practice the equilibration of each dose was carried out until no further increase of cesium concentration in the emitting area was noted as determined by work function variations. The importance of equilibrating the shank can be emphasized by noting that in some instances a 15% change in measured work function was observed between initial equilibration of the dose (as determined from the symmetrical field emission pattern) and complete shank equilibration.

The measurement of I-V characteristics while heating the tip was accomplished by inserting a Keithley Model 600A electrometer in the anode circuit. This allowed measurement of work function while simultaneously controlling the tip temperature by the electronic servo-circuit. The end points employed in rate studies involving surface diffusion and thermal desorption were determined by pattern changes (using pulsed field emission microscopy) and/or changes in surface work function.

WORK FUNCTION VARIATION WITH CESIUM COVERAGE

The field emission microscope has proved to be an important tool for elucidating the behavior of adsorbed layers on both metal and semi-conducting

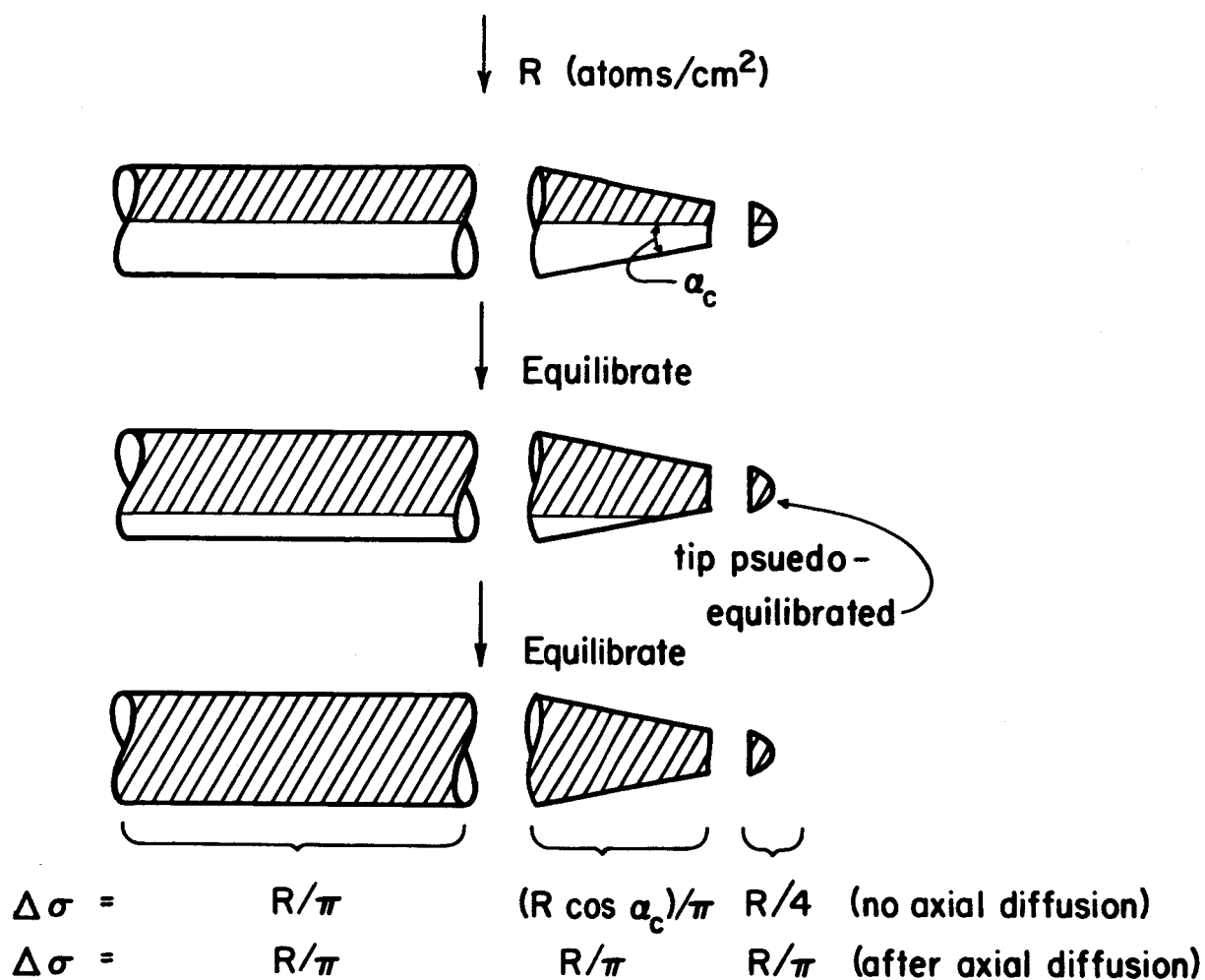


Figure 4. Equilibration sequence showing initial dosage (top) where emitter and shank are half covered, psuedo-equilibration (center) where emitter is covered but shank is not, and final equilibration (bottom) where both emitter and shank are completely and uniformly covered.

substrates. One of the variables frequently measured when investigating the surface kinetics and electron work function of such systems is the surface concentration of the adsorbed layer. Normally, in field emission microscopy it is not possible to measure the surface concentration of the adsorbed layers directly; therefore, an indirect method is employed, which utilizes existing relationships between work function (WF) and adsorbate concentration σ . The WF is readily determined in the field emission microscope by "Fowler-Nordheim" plots of the I-V characteristics, as described previously.

Since field emission determined relationships between ϕ and σ are virtually non-existent, it has been customary in the past to resort to such relationships determined by other methods, usually employing thermionic techniques. In view of this, it was decided to investigate the agreement between thermionic and field emission determined work functions for cesium on tungsten and to consider the effect of different substrates on these relationships. In addition, we investigated the effect of oxygen on the $\phi - \sigma$ relationships.

Some of the problems inherent in much of the existing thermionic work devoted to establishing $\phi - \sigma$ relationships stem from the difficulty in determining absolute values of σ because of uncertain degrees of surface roughness; also, it is difficult to establish the crystal planes contributing to the average value of the WF when dealing with polycrystal-face surfaces because of the excessive weighting toward the low WF planes⁴. Projection microscopy, which is natural to the embodiment of field emission techniques and has also been employed with thermionic techniques⁷, reduces the latter disadvantage; moreover, it is possible to entirely eliminate the averaging problem by using probe methods⁸ which confine the WF measurement to a single crystal face of a polycrystal-face surface. An additional uncertainty in such measurements which utilize polycrystal-face surfaces is the possible non-uniform distribution of the adsorbate over the various exposed crystal faces.

In view of these difficulties, the ideal surface for an investigation of this nature should be a planar, atomically smooth, single crystal surface. Field emitters fulfill part of these requirements by exposing a nearly atomically smooth single crystal surface, but the necessary hemispherical shape of these emitters automatically cause a variety of crystal planes to be exposed. The advantage of the use of probe techniques to overcome the latter difficulty in field emission is partially offset by the inability to confidently state the distribution of the adsorbate over the exposed crystal faces, even though an average value of σ is known.

In spite of these shortcomings of field emission techniques to establish unequivocally $\phi - \sigma$ relationships, certain advantages of this technique plus the need for determining any discrepancies between field emission and thermionic techniques provide sufficient motivation to initiate an investigation of this nature.

Cesium on Molybdenum, Tungsten, and Rhenium

The variation of field emission work function with cesium coverage has been investigated for tungsten, molybdenum and rhenium substrates; for the latter two substrates only ϕ_{av} vs. relative cesium coverage has been determined thus far.¹ In each case the work function has a minimum value ϕ_m at a particular cesium atom density σ_m and increases with cesium coverage to a constant value which is identical to the bulk work function of cesium (1.81 ev). The pertinent results are summarized in Table I where it can be seen that ϕ_m is approximately 1.50 ev, independent of the initial work function of the clean substrate.

TABLE I

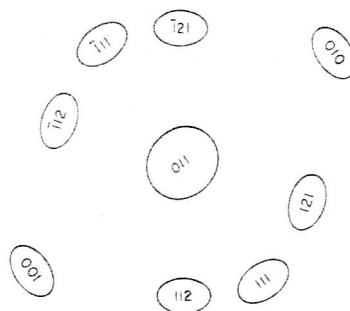
Values of Various Substrate Work Functions at Zero Cesium Coverage ($\sigma = 0$), the Work Function Minimum ($\sigma = \sigma_m$) and the Highest Coverage Investigated ($\sigma = \sigma_{\infty}$).

Substrate	$\phi (\sigma = 0) \text{ ev.}$	$\phi (\sigma = \sigma_m) \text{ ev}$	$\phi (\sigma = \sigma_{\infty}) \text{ ev}$
Molybdenum	4.20	1.50 ± 0.05	1.82 ± 0.03
Tungsten	4.52	1.53 ± 0.05	1.83 ± 0.03
Rhenium	4.85	1.45 ± 0.05	1.80 ± 0.03

The characteristic field emission patterns for the substrates with various amounts of adsorbed cesium are shown in Figures 5 to 7. The following similarities among the patterns for the different substrates were noted: 1) at low cesium coverages the emission is confined to the vicinities of the highest work function planes of the originally clean substrate (i. e., the $\{110\}$ for tungsten and molybdenum and the $\{0001\}$ and $\{10\bar{1}1\}$ for rhenium); 2) in the mid-coverage range the emission is confined strictly to the originally high work function planes of the clean substrate; 3) at coverages greater than σ_m the emission distribution approaches that of the originally clean substrate. The transition between patterns (c) and (d) of Figures 5 to 7 occurs somewhat gradually in the work function range 2.2 to 2.6 ev for the three substrates, whereas the transition between patterns (d) and (e) occurs suddenly at the coverage σ_m . The implications of these pattern changes will be discussed below.

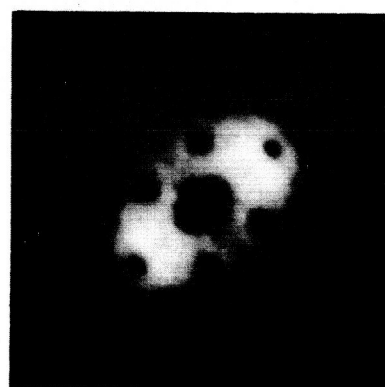
Work Function Change Versus Absolute Cesium Coverage on Tungsten

Results from Two Emitter Tube. - The results of the WF variation with σ obtained from the two-emitter tube are compared in Figure 8 with the earlier results of Taylor and Langmuir³; the latter's results have been normalized such that the work function minima coincide. The excellent agreement in relative shape between the two curves indicates that corrections to field



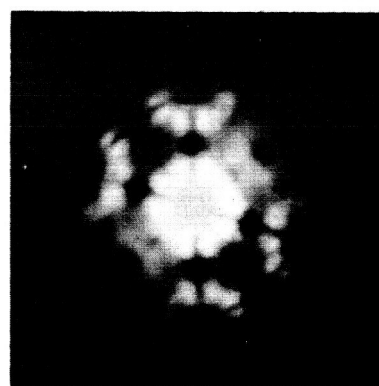
(a)

Principal planes of the (011) oriented body centered cubic structure corresponding to (b)



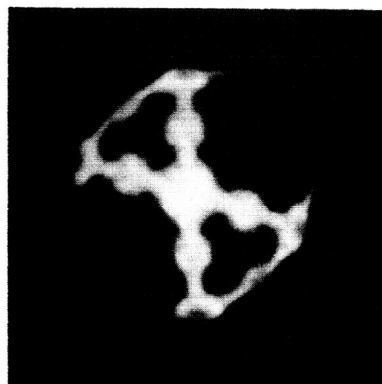
(b)

$\phi = 4.20 \text{ eV}$
Clean Molybdenum



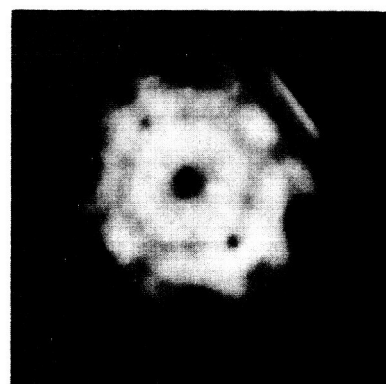
(c)

$\phi = 3.80 \text{ eV}$



(d)

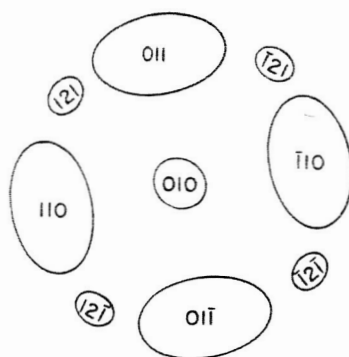
$\phi = 1.62 \text{ eV}$



(e)

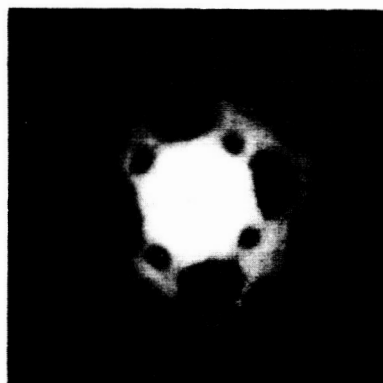
$\phi = 1.80 \text{ eV}$

Figure 5. Principal field emission pattern changes for cesium adsorption on molybdenum.



(a)

Principal planes of the (010) oriented body centered cubic structure corresponding to (b)



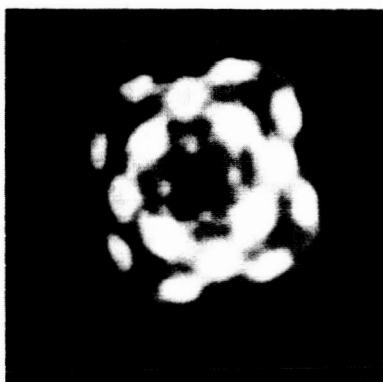
(b)

$\phi = 4.52 \text{ eV}$
Clean Tungsten



(c)

$\phi = 2.84 \text{ eV}$
 $\sigma = 0.6 \times 10^{14} \text{ atoms/cm}^2$



(d)

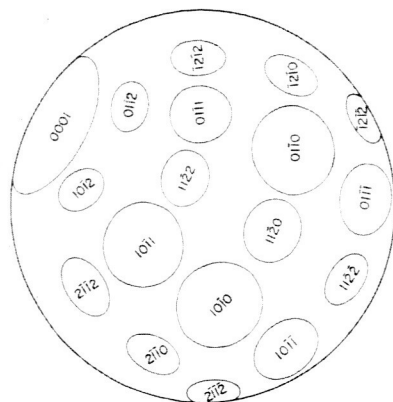
$\phi = 1.71 \text{ eV}$
 $\sigma = 1.45 \times 10^{14} \text{ atoms/cm}^2$



(e)

$\phi = 1.70 \text{ eV}$
 $\sigma = 2.45 \times 10^{14} \text{ atoms/cm}^2$

Figure 6. Principal field emission pattern changes for cesium adsorption on tungsten.



(a)

Principal planes of hexagonal close packed structure corresponding to (b)



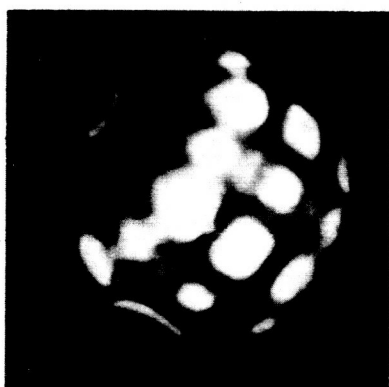
(b)

$\phi = 4.85 \text{ ev}$
Clean Rhenium



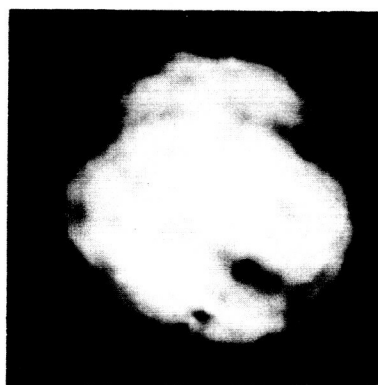
(c)

$\phi = 4.01 \text{ ev}$



(d)

$\phi = 1.59 \text{ ev}$



(e)

$\phi = 1.67 \text{ ev}$

Figure 7. Principal field emission pattern changes for cesium adsorption on rhenium.

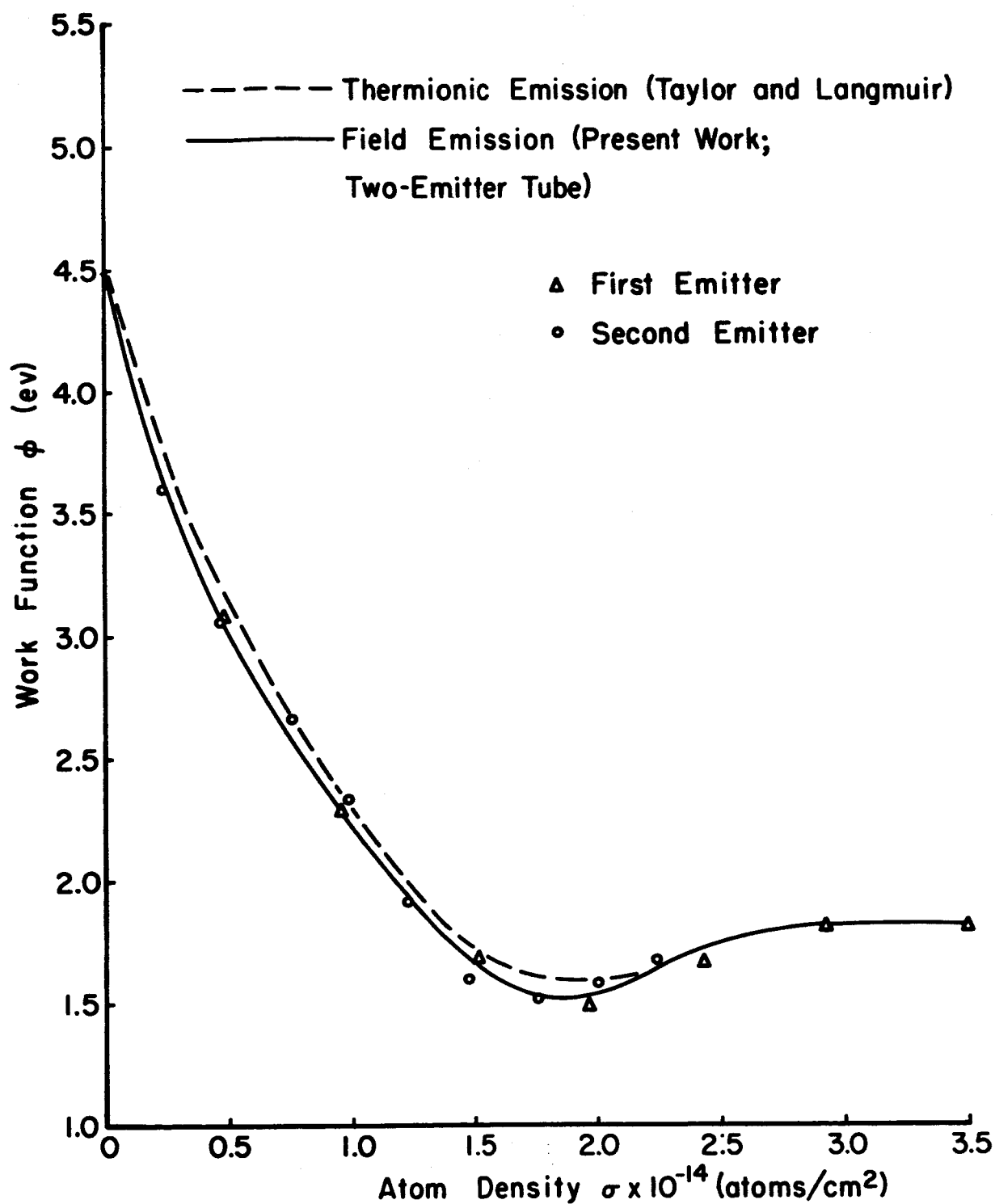


Figure 8. Field emission work function as a function of average cesium atom density on tungsten. Present data from the two-emitter tube are compared with earlier results of Taylor and Langmuir whose atom density at the minimum work function has been normalized to agree with the present value of 1.9×10^{14} atoms/cm².

emission work functions due to dipole discreteness⁹ and field induced dipole moments¹⁰ are insufficient to cause perceptible deviations from thermionic determined work functions. This result is interesting since it suggests that even for a highly polarizable adsorbate the contribution to the work function by the induced dipole moment term $4\pi\sigma aF$, where a is the ad-atom polarizability, is negligible. The implications of this will be discussed in greater detail in a following section, "Discussion of Results."

Some disagreement exists in the literature regarding the exact value of σ_m for cesium on tungsten. Using thermionic methods Becker¹¹ reported a value of 3.8×10^{14} atoms/cm² while Langmuir³ reported 3.2×10^{14} which he adjusted to 2.4×10^{14} by assuming a surface roughness factor of 1.34. The value of σ_m determined by this investigation is 1.9×10^{14} which is substantially lower than previously reported values. In view of the good functional agreement between our results and Langmuir's it seems likely that the discrepancies in σ_m are attributable to uncertainties in surface roughness rather than to fundamental differences between thermionic and field emission techniques. The single crystal emitters used in this study were atomically smooth, not only in the emitting region, but also along the shank as determined by electron micrographs of this region; it is therefore unlikely that errors in σ could occur in this work because of excessive surface roughness of the emitters.

Results from Probe Tube. - The results of the probe tube measurements of ϕ_{100} vs σ are given in Figure 9 along with the corresponding ϕ_{av} vs σ curve. It should be emphasized that the σ values are obtained by assuming uniform coverage over the emitting area and that local variations in σ cannot be directly determined, but only implied.

One of the interesting features of the preliminary results of this study is the indication that the slope of the ϕ_{100} curve is less than the slope of the ϕ_{av} curve at $\sigma = 0$. This is in agreement with observed pattern changes at very low coverage which are confined to the (110) region. Since the work function of the clean (110) plane is ~ 6.0 eV, and since the average work function is weighted toward the (110) region (see Figure 6) at low coverages, it follows that the ϕ_{110} vs σ curve should have a slope which is appreciably greater than average at low coverages. If one assumes that the low coverage part of the ϕ vs σ curves should extrapolate smoothly to $\sigma = 0$ without the occurrence of discontinuities or points of inflections, then it follows from the existing data that some horizontal shifting to the left of the curve for the (100) plane (and probably to the right for the (110) plane curve, when it is measured) will be necessary at least in the low coverage region; this, in turn, implies from the respective directions of shift that in all probability the cesium coverage on the (100) plane is somewhat less than average, while the coverage on the (110) plane is greater than average.

It should also be mentioned that in addition to non-uniformities in the coverage distribution, variations in the ad-atom dipole moment μ with crystal plane may also occur. Although the latter variations should not a priori lead to discontinuities in the ϕ - σ relationships, it is interesting to note that such variations are in the direction suggested by the present data. For example, one expects cesium adsorbed on the (100) plane to possess a smaller dipole moment per ad-atom than it would on the (110) plane for the following

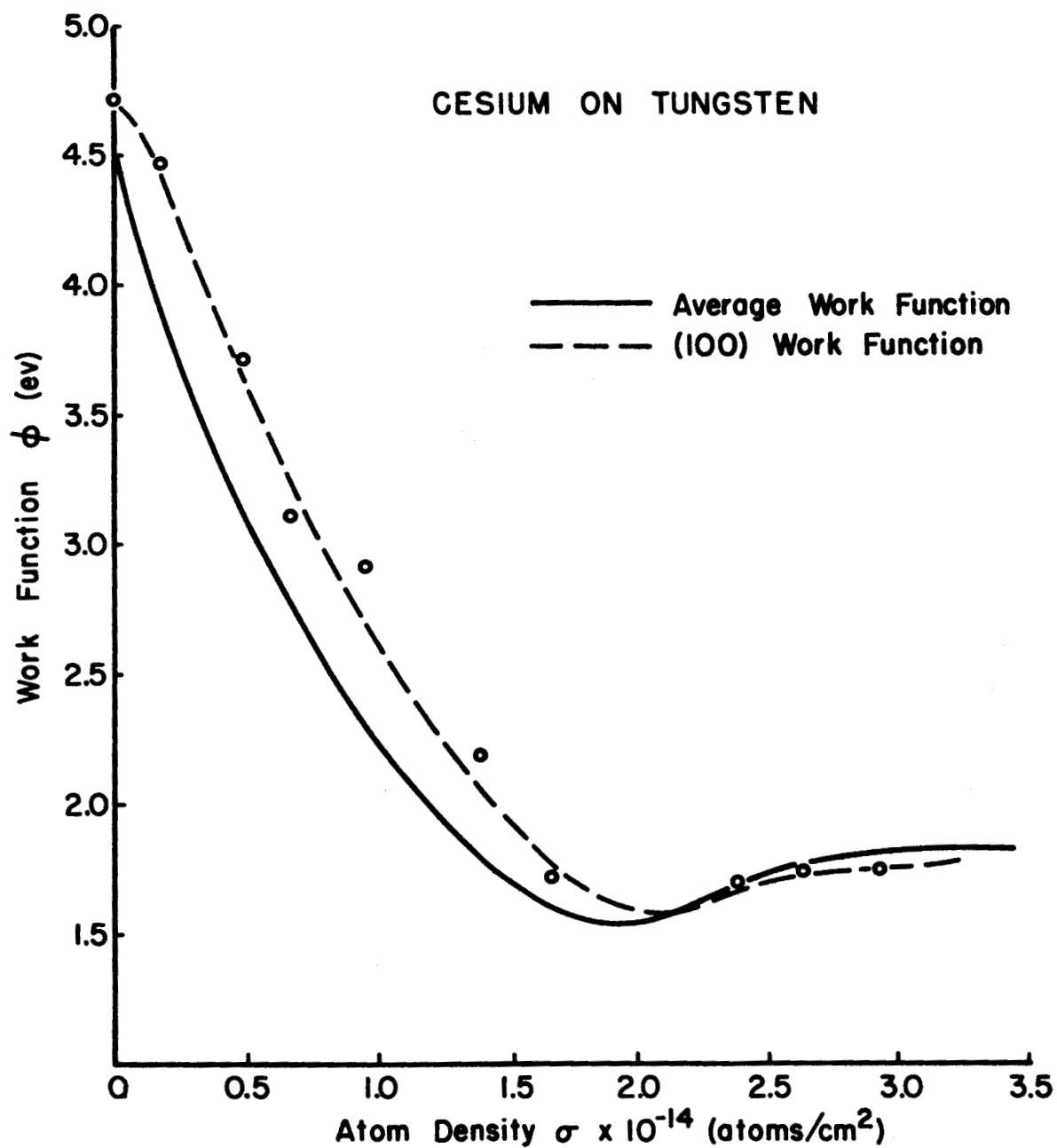


Figure 9. Average work function and work function of the (100) plane as functions of cesium adsorbed on tungsten. Work function of (100) plane obtained from probe tube.

reasons: 1) the surface electric fields due to electron spillover which leads to induced dipole moments on the ad-atom are smaller on the (100) than on the (110) plane, 2) if ionic adsorption occurs at low coverages, it would be more apt to occur on the high work function (110) rather than (100) planes, and 3) the more open structure of the (100) plane allows the ad-atom to seat further into the lattice than on the close packed (110) plane and thereby reduces the effective dipole moment of the ad-atom.

We will show in succeeding discussion that for $\phi > \phi_m$ it is likely that both ϕ and μ become uniform over the emitting surface which is in agreement with the merging of the ϕ_{av} and the ϕ_{100} curves of Figure 9.

Effect of Oxygen

It has been known for some time that oxygen greatly affects the adsorption characteristics of cesium on tungsten.¹¹ We have shown previously¹ that various amounts of underlying chemisorbed oxygen greatly alters the relationships between ϕ and ϕ . To summarize, it was found that both the minimum work function ϕ_m and the coverage ϕ_m at which ϕ_m occurred decreased with increasing amounts of underlying chemisorbed oxygen. Because of uncertainties in the equilibration of the successive cesium doses (not fully appreciated earlier),¹ a few of the $\phi - \phi$ relationships were redetermined with various amounts of underlying oxygen. The results of the effect of chemisorbed oxygen on the $\phi - \phi$ relationships are shown in Figure 10, and the principle pattern changes are shown in Figure 11. It is observed that the functional relationships of the $\phi - \phi$ curves remain unchanged, although a decrease in both ϕ_m and ϕ_m occurs with increasing oxygen coverage. The primary alteration of the pattern changes from that of clean tungsten (see Figure 6) is the enhanced emission from the {112} planes and diminished emission from the {110} planes for $\phi < \phi_m$. For $\phi > \phi_m$ the clean tungsten emission distribution is obtained as before regardless of the amount of underlying oxygen. Similar pattern changes and work function changes have been obtained for cesium and oxygen co-adsorption on molybdenum; for the Cs-O-Mo system, a value of ϕ_m as low as 1.0 ev has been measured, slightly lower than that obtained for the Cs-O-W system.

It is interesting to note the large shift in ϕ_m and profound pattern changes caused by a very small amount of chemisorbed oxygen as shown in curve (b) of Figure 10. Undoubtedly one of the effects of oxygen is to increase the dipole moment of the adsorption complex, and it appears to be most successful in doing so on the {112} rather than the {110} planes.

As mentioned previously¹, the irreversibility of work function and pattern changes with respect to cesium adsorption above 700°K is attributed to a transition of the chemisorbed oxygen to incipient oxide formation, which obviously adds a degree of complexity to the interpretation of the results in the higher temperature range. The apparent explanation of the emission distribution in the low temperature region (i. e., below 700°K) attributes the enhanced work function lowering to those crystallographic regions of the surface which are most capable of stabilizing the Cs-O-M

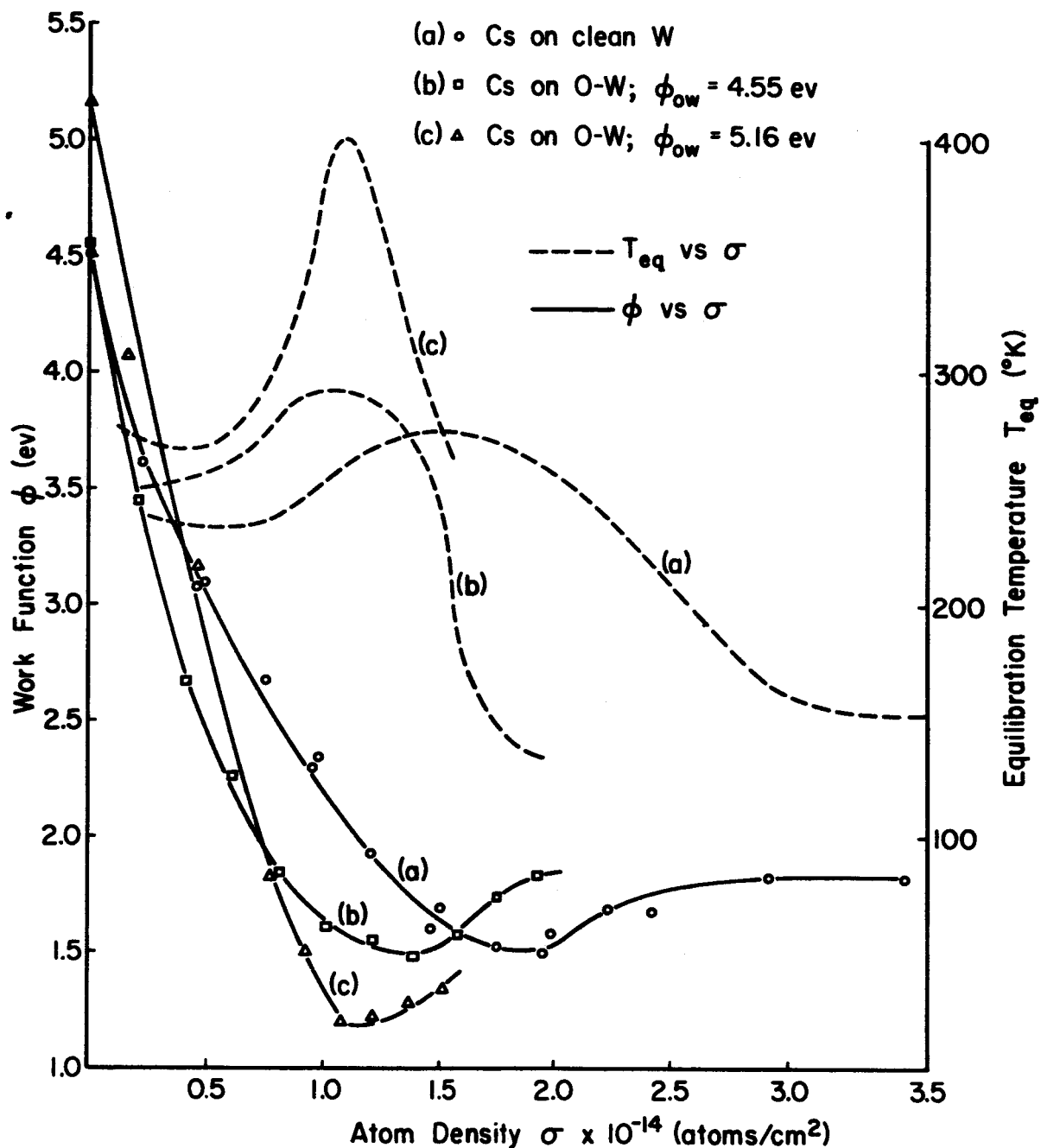
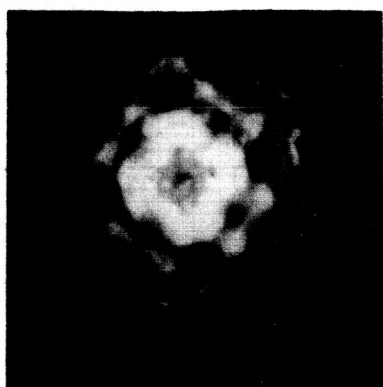
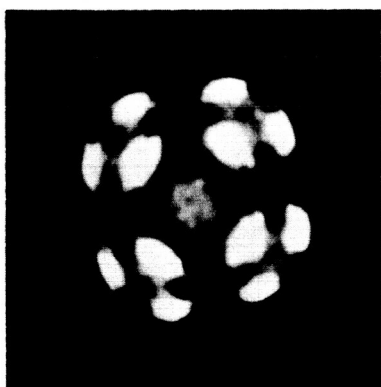


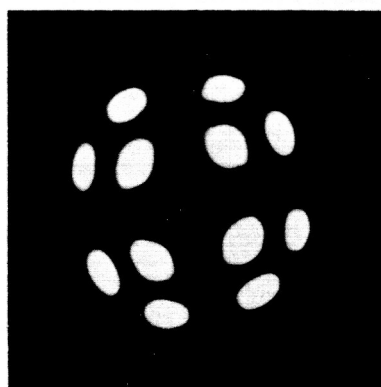
Figure 10. Field emission work function and equilibration temperature as functions of average cesium atom density for clean tungsten and for two degrees of underlying oxygen coverage.



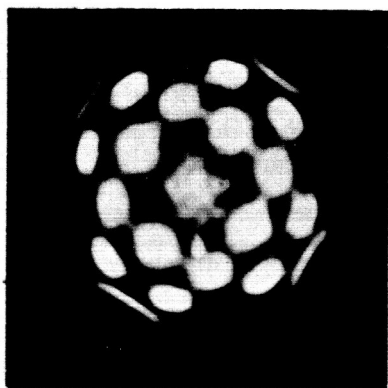
(a)
 $\phi = 5.65 \text{ ev}$
 Oxygen on Clean Tungsten



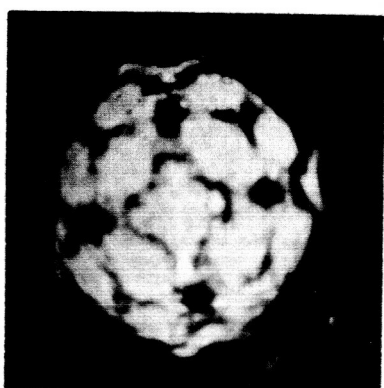
(b)
 $\phi = 2.27 \text{ ev}$



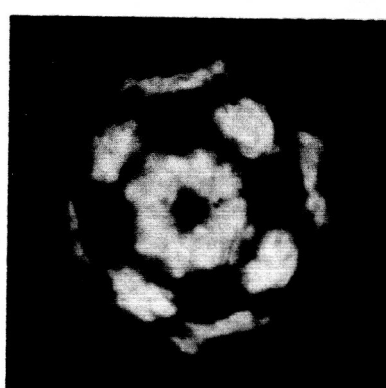
(c)
 $\phi = 1.61 \text{ ev}$



(d)
 $\phi = 1.50 \text{ ev}$



(e)
 $\phi = 1.13 \text{ ev}$



(f)
 $\phi = 1.35 \text{ ev}$

Figure 11. Principal field emission pattern changes for cesium adsorption on tungsten initially covered with a partial chemisorbed layer of oxygen. Tip orientation same as Figure 6.

complex (where M refers to the surface). In the case of clean tungsten simple geometric considerations of the adsorbate radius and substrate lattice constant (assuming hard spheres in each case) show the $\{110\}$ and $\{112\}$ planes to contain the highest site densities for cesium, while the $\{100\}$ planes would have a low site density¹². Indeed, this appears to be the primary motivating force which controls the emission distribution for cesium on clean tungsten for $\theta < \theta_m$. On the other hand, it would be geometrically difficult for the smooth (110) plane of tungsten to stabilize a Cs-O-W complex, whereas such a configuration could be envisaged on the $\{112\}$ and $\{100\}$ planes, since it is possible for the oxygen to seat into the empty voids on these surfaces without greatly disturbing the over-layer of cesium, except through electronic perturbations leading to a higher dipole moment per ad-atom.

The foregoing model can be used to explain why only a relatively small average oxygen concentration is necessary to produce the observed effects on cesium adsorption, by assuming the oxygen atoms to be preferentially chemisorbed on the $\{112\}$ and $\{100\}$ regions at low average coverages. Although experimental evidence for such an assumption is not available, these sites appear to be most favorable for oxygen adsorption on the basis of possessing the largest number of nearest neighbor tungsten atoms per adsorbed oxygen atom.

Discussion of Results

The approach of the measured WF to that of bulk cesium at, or near, the nominal monolayer θ_o regardless of the underlying substrate structure or WF, as observed in this study, has also been observed for other alkali and alkaline earth adsorbates and appears to be a general rule. In addition, in the same coverage region that the WF approaches the bulk cesium value, the emission distribution approaches that of the originally clean substrate as shown in Figures 5 to 7; thus, it follows that $\Delta\theta$ must be nearly identical for each crystal plane of the polycrystal-face emitter in the coverage $\theta \approx \theta_o$. If we assume the relation between $\Delta\theta$ and θ is according to the Helmholtz equation

$$\Delta\theta = 4\pi\theta\mu \quad (5)$$

it follows that for $\Delta\theta$ to be uniform over the surface, μ and θ must not vary from plane to plane for $\theta \approx \theta_o$, since it is unlikely that they could adjust their values such that their product is the same on all crystal planes.

The probe tube results suggest a non-uniform coverage distribution $\theta < \theta_m$, whereas we conclude from the above discussion that a uniform coverage distribution exists for $\theta \approx \theta_o$. In previous work¹ we have given evidence for the occurrence of a change in state (or phase) of the adsorbed cesium at θ_m . It was pointed out that a cesium coverage distribution controlled primarily by the variation in substrate site density from plane to

plane could account for the observed emission distribution for $\phi < \phi_m$. In addition, the transition to a uniform coverage distribution for $\phi > \phi_m$ was attributed to the onset of long-range order motivated by increasing importance of lateral interactions in the high coverage phase.

It is interesting to note that these same observations appear to apply when various amounts of underlying oxygen is present. Thus, the experimentally confirmed rule that many metal adsorbates approach their bulk work function value near ϕ_0 regardless of the structure and work function of the underlying substrate is evidence in support of the theoretical conclusion¹³ that the WF does not depend on the volume structure of a metallic emitter, but only on the structure of the surface layer. This, in turn, implies that a monolayer of adsorbate is sufficient to screen out the electrical effects of the substrate, and the electronic distribution normal to the composite surface is the same as if the substrate were replaced by a solid piece of adsorbate.

The above suggests that ϕ_0 , a surface coverage of one monolayer, be defined as that surface coverage at which the bulk work function of the metal adsorbate is attained. In the case of cesium other evidence¹ (e. g., approach of desorption and surface diffusion rates to their bulk values at ϕ_0) tends to support this view, although it should be realized that these definitions do not allow ascertainment of an exact value of ϕ_0 .

According to Figure 8, the bulk work function of cesium is attained at a coverage of approximately 2.8×10^{14} atoms/cm² which is interestingly close to the atom density of the (100) plane of bulk cesium. It is not clear which plane or planes the reported work function for bulk cesium refers to; most likely it is weighted towards the low work function (111) and (100) planes, rather than the higher work function (110) plane. The atom density of the close-packed (110) plane of bulk cesium is approximately 3.8×10^{14} atoms/cm²; however, it is clear from Figure 8 that the monolayer condition is reached well before this atom density is attained in the adsorbed cesium layer. The reason for the apparent shift of the monolayer condition to lower cesium coverage on addition of underlying chemisorbed oxygen (Figure 10) is not obvious, although the shift may possibly be attributed to an increase in the repulsive part of the lateral interactions which, in turn, lead to an increase in the average distance between adsorbed cesium atoms at the monolayer coverage.

It was mentioned earlier that the close agreement between field and thermionic emission work functions throughout the cesium coverage range inferred a negligibly small contribution by the field-induced work function, normally given by

$$\Delta\phi^F = 4\pi\alpha F_0, \quad (6)$$

where α is the polarizability of the ad-atom and F_0 is the effective field on the ad-atom at the equilibrium distance x_0 from the surface of electric neutrality. Using a conservative value of $\alpha = 20 \text{ \AA}^3$, one calculates a 20%

increase in ϕ at ϕ_m due to the field-induced work function change. A change of this magnitude should have been observed. In order to account for the lack of change, a more critical examination of how $\Delta\phi^F$ enters into the Fowler-Nordheim equation is needed.

The Fowler-Nordheim equation may be written in terms of directly measurable parameters, applied voltage V and emitted current I , as

$$\ln\left(\frac{I}{V^2}\right) = \ln\left[\frac{B}{\phi t^2(\phi, F)}\right] - \frac{b\phi^{3/2}v(\phi, F)}{\beta V}, \quad (7)$$

where $t(\phi, F)$ and $v(\phi, F)$ are tabulated functions¹⁴ taking into account the image correction, B is a function of tube geometry only, and $b = 6.8 \times 10^7$ when I is in amperes, F in v/cm, and ϕ in ev. Equation (7) may also be written as

$$\ln\left(\frac{I}{V^2}\right) = \ln(A) - m/V, \quad (8)$$

where A is the intercept and m is the slope of a "Fowler-Nordheim" plot of the $I(V)$ data plotted in the form $\ln\left(\frac{I}{V^2}\right)$ versus $1/V$. Taking into account

the field-induced work function correction, equation (7) becomes

$$\ln\left(\frac{I}{V^2}\right) = \ln\left[\frac{B}{(\phi + \Delta\phi^F) t^2(\phi + \Delta\phi^F, F)}\right] - \frac{b(\phi + \Delta\phi^F)^{3/2}v(\phi + \Delta\phi^F, F)}{\beta V} \quad (9)$$

Equations (7) and (9) may be simplified somewhat by noting that, to within 1%, $v(\phi, F)$ may be approximated by

$$v(\phi, F) = 0.943 - 0.146 \times 10^6 \frac{F}{\phi^2} \quad (10)$$

over the range of F and ϕ covered in cesium adsorption. Relating F_0 to the applied field F by $F_0 = c_0 F$, where $c_0 = f(\phi, x_0)$, and combining equations (6), (9), and (10) with the assumption that $\Delta\phi^F \ll \phi$ (so that $(\phi + \Delta\phi^F)^{3/2}$ can be expanded), we obtain

$$\ln\left(\frac{I}{V^2}\right) = \ln\left[\frac{B}{(\phi + \Delta\phi^F) t^2(\phi + \Delta\phi^F, F)}\right] + \frac{9.94}{(\phi + \Delta\phi^F)^{1/2}} - \frac{5.66 b \pi \phi^{1/2} c_0 a - 0.943 b \phi^{3/2}}{\beta V} \quad (11)$$

Within the limits of the above approximations the experimental intercept $\ln A$ of the Fowler-Nordheim plot (equation 8) is given by

$$\ln A = \ln\left[\frac{B}{(\phi + \Delta\phi^F) t^2(\phi + \Delta\phi^F, F)}\right] + \frac{9.94}{(\phi + \Delta\phi^F)^{1/2}} - 5.66 b \pi \phi^{1/2} c_0 a. \quad (12)$$

It is now possible to obtain an expression for ac_0 by letting

$$\Delta \ln A = \ln A - \ln A_s,$$

where $\ln A_s$ is the intercept value when σ and, hence, $\Delta\phi$ are zero; the resulting expression for ac_0 is

$$ac_0 = \frac{\log \left[\frac{\phi_s t^2(\phi_s, F)}{(\phi + \Delta\phi^F) t^2(\phi + \Delta\phi^F, F)} \right] + 4.32 \left[\frac{1}{(\phi + \Delta\phi^F)^{1/2}} - \frac{1}{\phi_s^{1/2}} \right] - \Delta \log A}{1.67 \times 10^8 \pi \sigma \phi^{1/2}} \quad (13)$$

At small values of σ , the product ac_0 can be determined from equation (13)

by assuming $\phi + \Delta\phi^F \cong \phi$ since $\phi > \Delta\phi$; at larger values of σ (where this

approximation is less valid) an iteration method can be used to determine

correct values of ac_0 .

Values of ac_0 calculated by the above method are given in Table II and show a general decrease with increasing σ . A method for calculating c_0 has been given elsewhere¹⁵. Briefly, the polarizing field at a distance x_0 (the equilibrium distance of the ad-layer from the surface) is approximately

$$F_0 = F - \left(\frac{\partial \Delta\phi^F}{\partial x} \right)_{x_0} \quad (14)$$

The expression for $\Delta\phi^F$ given in equation (6) is the value at $x = \infty$ and should be multiplied by a factor $k(x, \sigma)$ in order to be valid at finite x ; this factor ranges from 0 to 1 and arises from the fact that $\Delta\phi^F$ does not attain its full value at finite value of x due to dipole discreteness. In order to analytically incorporate this effect in the steps leading to equation (11), one must apply the correction to the electric potential expression in the unintegrated tunneling coefficient for field emission; since this is outside the scope of this investigation we have assumed $k(x, \sigma) = 1$, which is more nearly true at large values of σ . Multiplying the right side of equation (6) by the factor $k(x, \sigma)$, it is possible to combine equations (6) and (14) to obtain the following expression for c_0 :

$$F_0 = \frac{F}{1 + 4\pi \sigma a \left(\frac{\partial k}{\partial x} \right)_{x_0}} = c_0 F. \quad (15)$$

It is now possible to eliminate c_0 by combining equations (13) and (15) and obtain values for a which are also given in Table II. The values for

$\left(\frac{\partial k}{\partial x} \right)_{x_0}$ as a function of σ were determined by a method described elsewhere.¹⁵

TABLE II

Polarizabilities of Adsorbed Cesium as Determined by Equations (13) and (15)

$\sigma \times 10^{-14}$ (Atoms/cm ²)	Cs on W			$\sigma \times 10^{-14}$ (Atoms/cm ²)	Cs on Mo		
	$\Delta \log A$	$a_{c_o}(A^3)$	$a(A^3)$		$\Delta \log A$	$a_{c_o}(A^3)$	$a(A^3)$
2.2	1.11	4.17	5.04	2.86	0.89	2.45	2.85
1.64	0.87	7.65	9.59	2.58	0.70	4.10	5.17
1.49	0.85	7.25	8.65	2.28	0.61	6.02	8.14
1.47	0.86	6.92	8.15	2.14	0.62	7.00	9.70
1.48	0.54	9.79	12.50	1.86	0.42	10.00	14.86
1.40	0.23	12.00	15.79	1.60	0.54	9.33	12.21
1.35	0.11	12.95	17.08	1.03	0.15	10.68	12.14
1.05	0.22	10.40	11.83	0.53	-0.25	15.90	16.90
0.91	0.01	12.20	13.69	0.20	-0.33	25.19	25.47
0.60	-0.22	15.32	16.30	0.18	-0.23	22.76	22.95
0.41	-0.33	19.11	19.80				
0.15	-0.22	23.24	23.38				

The values of a so calculated are close to the gas phase atomic value at low coverage and decrease toward values approaching that of the ionic state at high coverage. This result is surprising and generally contrary to contemporary qualitative ideas of the bonding state, since it suggests a high degree of ionic contribution at high, rather than low coverages. It is possible, however, that the ionicity of the adsorbed state may not be accurately given by a values so determined. For example, if metallic (or atomic) bonding is incurred throughout most of the coverage range, it is possible that only at low coverages where lateral interaction is negligible that atomic values of a are realized; as the ad-atom density approaches that of bulk cesium, overlap of lateral wave functions is large and a (as measured by an external field) of a surface layer with electrical structure of bulk cesium loses its meaning. Before a detailed interpretation of these results is appropriate, it will be necessary to examine in greater detail the validity of the assumptions leading to equations (13) and (15).

In conclusion, it can be stated that two major problems in relating \emptyset vs σ data obtained from polycrystal-face surfaces to existing theories¹⁶⁻¹⁸ are 1) uncertainties in local variations in σ , and 2) reversals in emission distribution so that average \emptyset values of the clean substrate are no longer valid in determining $\Delta\emptyset$. In view of this, one must exercise caution in relating much of the existing \emptyset - σ data to the several existing theories. However, if these points are kept in mind, some interesting results are obtained from a comparison of the data with a suitably applicable theory.

One of the earliest theories¹⁹ explaining the work function minimum is based on the mutual depolarization of neighboring ad-atoms and is given by the following expression:

$$\Delta\phi = \frac{4\pi\mu_0\phi}{1 + 9a\phi^{3/2}}, \quad (16)$$

where a is the polarizability of the ad-atom and μ_0 is the dipole moment at zero coverage. Figure 12 shows the data of Figure 8 plotted according to the following alternative form of equation 16:

$$\theta^{3/2} = \frac{3}{2} \Delta\phi_m \frac{\theta}{\Delta\phi} - \frac{1}{2} \quad (17)$$

where $\theta = \frac{\phi}{\phi_m}$ and $\Delta\phi_m$ is the maximum work function change. In

addition, one can obtain expressions for $\Delta\phi_m$ and ϕ_m in terms of a and μ_0 as follows:

$$\phi_m = (2/9a)^{2/3} \quad \text{and} \quad \Delta\phi_m = 1.503\mu_0/a^{2/3}.$$

If the simple depolarization model is valid, according to equation (17) the slope and intercept of the plot shown in Figure 12 should be 4.40 eV and -0.50 respectively; the measured values of the slope and intercept of the segment of straight line determined by the data for $\phi > \phi_m$ are 4.20 eV and -0.43 respectively which are in reasonable agreement with theory. The corresponding values of a and μ consistent with equation (17) are $88.6 \times 10^{-24} \text{cm}^3$ and $12.0 \times 10^{-18} \text{e.s.u.}$ respectively. This value of a is considerably higher than that suggested above from analysis of the Fowler-Nordheim equation in this coverage range; further study will be necessary to determine which is the correct analysis of a . In further support of this model it may be argued that the deviation from equation (17) noted at $\phi < \phi_m$ in Figure 12 is expected and due to the onset of both non-uniform coverage and a shift in emission to the high work function planes which invalidate $\Delta\phi$ values based on the average work function of the clean substrate.

In spite of the above evidence for the simple depolarization model, at least in the limited coverage region where the coverage is probably uniform and the emission distribution that of the clean substrate, it is unlikely that one model will hold over the entire coverage range. For example, the classical depolarization model cannot be expected to hold at coverages very near ϕ_0 since the overlap of neighboring ad-atom electronic clouds will require a quantum mechanical analogue. It is apparent that further investigations of work function change, particularly utilizing probe techniques, will be necessary to provide sufficient data amenable to detailed theoretical analysis.

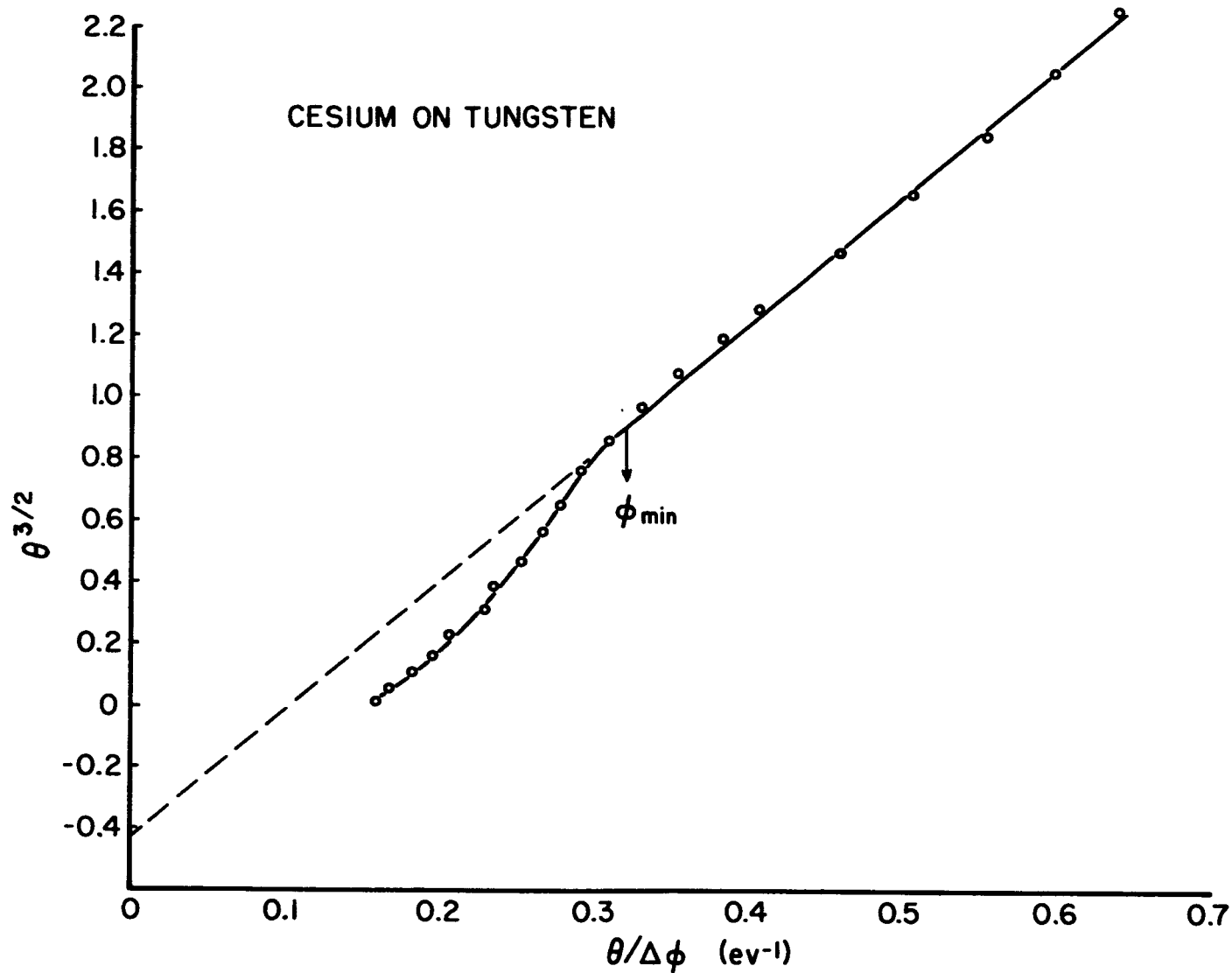


Figure 12. Work function - cesium atom density data of Figure 8 plotted according to equation 17.

EFFECT OF TEMPERATURE ON WORK FUNCTION

Results on Molybdenum

Increasing the temperature at any cesium coverage from 77°K to the temperature where thermal desorption begins to occur causes no appreciable change in the emission distribution. This result is evidence that over most of the desorption temperature range (i.e., 77°K to 900°K) the adsorbed cesium (at a given coverage) does not greatly alter its coverage distribution with temperature; thus, it is unlikely that variations in ϕ with temperature can be attributed to local variations in ϕ .

At a fixed cesium coverage, it was found that ϕ does decrease with increasing temperature. The temperature dependence of ϕ for cesium on molybdenum at two coverages was determined by analyzing the I-V data taken at various temperatures according to the following relation¹⁴, which contains the approximate correction for the Boltzman tail to the Fermi distribution in the temperature range employed:

$$I(T, F) = P(T) A F^2 \exp(-b\phi^{3/2}/F), \quad (18)$$

where A is a slowly varying function of ϕ and emitting area, and

$$P(T) = \pi p / \sin \pi p, \quad (19)$$

in which p is a complicated function of T, F, and ϕ , and is given approximately by

$$p \approx 9.3 \times 10^3 T \frac{\phi^{1/2}}{F}, \quad (20)$$

where T is in degrees K, F in v/cm and ϕ in ev.

The results summarized in Table III indicate an approximate value for $\Delta\phi/\Delta T$ of $-1.3 \times 10^{-4} \text{ ev}/^\circ\text{K}$ in the temperature range investigated: within the experimental scatter this value appears independent of the cesium coverage range investigated.

TABLE III
Work Function Change $\Delta\phi$ with Temperature for Cesium on Molybdenum

$\phi \times 10^{-14}$ (atoms/cm ²)*	$\phi_{77^\circ\text{K}}$ (ev)	$T_1 - T_2$ (°K)	$\Delta\phi$ (ev)	$\frac{\Delta\phi}{\Delta T} \times 10^4$ (ev/°K)
0.24	3.49	77-152	-0.012	-1.59
0.24	3.49	77-203	-0.019	-1.48
1.20	1.96	77-270	-0.029	-1.49
1.25	1.91	77-270	-0.018	-0.86
1.30	1.87	77-162	-0.009	-1.03
1.30	1.87	77-209	-0.019	-1.46

* Values of ϕ assumed from Figure 8.

Discussion of Results

The values of $\Delta\phi/\Delta T$ are at least an order of magnitude higher than and opposite in sign to the values reported for clean molybdenum in the same temperature range²⁰. Similar results to those reported here have also been obtained for sodium on tungsten by Bosworth²¹ employing contact potential methods.

Further evidence that the temperature coefficient of the work function is not due to local variations in ϕ is given by the fact that below 160°K cesium is immobile on molybdenum. Bosworth postulates an increase in the ad-atom dipole moment as the primary cause of the decreases in work function with temperature. Our results tend to substantiate this explanation or a similar one such as a temperature dependent variation of the surface electronic distribution. For example, if the ad-atoms exist in a polar ground state (see Figure 3 of Reference 22), it is possible for a slow transition to an ionic state to occur at elevated temperatures, thus decreasing the negative charge about the ion.

RESULTS OF THERMAL DESORPTION OF CESIUM FROM VARIOUS REFRACTORY METALS

Considerable insight concerning the specific interactions of a particular adsorbate-substrate system can be derived from a knowledge of the activation energy of desorption of the adsorbate and its variation with surface coverage. In previous work¹ the results of the variation of the thermal desorption energy of electrically neutral cesium with surface coverage has been reported for molybdenum, tungsten and rhenium substrates. It was found that the activation energy of desorption at zero cesium coverage increased with substrate work function and decreased monotonically with increasing cesium coverage for each substrate to a value slightly below the heat of vaporization of bulk cesium (ca 0.69 eV). It should be pointed out that the kinetic methods used in field emission microscopy to obtain activation energies of desorption yield binding energy akin to a thermodynamic differential heat of desorption (assuming no activation energy of adsorption) rather than an integral heat of desorption; this means that the surprisingly low measured values of the activation energy of desorption of cesium near monolayer coverage does not imply a small binding energy for all the adsorbed cesium, but only for a differential amount of the total coverage.

Analysis of the thermal desorption energies of cesium at zero coverage for each of the three substrates indicated the following empirical relationship between activation energy of neutral desorption and average substrate work function ϕ_s :

$$E_a^0 = 2\phi_s - 6.0. \quad (21)$$

We are currently extending these measurements to platinum substrates in order to test the validity of the above empirical relationship over the widest possible range of substrate work function (4.20 to 5.30 eV) and substrate lattice structure (bcc, hcp and fcc).

From the relationship between the activation energy for ion desorption E_p^0 and for neutral desorption,

$$E_p^0 = E_a^0 + V_I - \phi, \quad (22)$$

it is possible to state the empirical relationship of equation (21) in terms of E_p^0 as follows:

$$E_p^0 = \phi_s - 2.1. \quad (23)$$

A further check of the universality of the empirical relationship noted in equation (21) and re-expressed in equation (23) can be made by measurement of E_p^0 at zero cesium coverage for the various substrates. On the basis of the average work function of clean molybdenum, tungsten and

rhodium being 4.20, 4.52 and 4.85 eV respectively, the values of E_p^0 calculated from equation (23) are 2.10, 2.42 and 2.75 eV also respectively. It is possible from field emission microscopy to determine E_p^0 in the cesium coverage range where the relation between the ionization potential V_I of cesium and the work function $\phi(\theta)$ of the composite surface satisfies the condition $V_I - \phi(\theta) \leq 0$. Normally, the emitter is held a few volts positive so that ions are collected at the cathode.

In earlier work¹ we have also investigated the effect of an underlying layer of chemisorbed oxygen on the desorption characteristics of cesium from tungsten. It was found that oxygen not only lowered the work function throughout the coverage range, but also the binding energy at a given work function was increased as the amount of chemisorbed oxygen was increased. In the present investigation we have extended these studies to an additional oxygen coverage to confirm the trends noted earlier; also, the recent results of ϕ vs. cesium atom density for various amounts of underlying chemisorbed oxygen shown in Figure 10 have allowed a qualitative determination of the variation of desorption rates with cesium coverage under these conditions.

Cesium Neutral Desorption

It was shown earlier that the activation energy for neutral cesium desorption from tungsten, molybdenum and rhodium decreased monotonically with increasing coverage to desorption energies slightly less than the heat of vaporization of bulk cesium. In the past we have written the expression for the rate of desorption $-d\theta/dt$ in the following form:

$$\frac{-d\theta}{dt} = \theta \nu \exp(-E_a^0/kT), \quad (24)$$

where $E_a^0(\theta)$ is the coverage dependent desorption energy and ν a pre-exponential factor which in the past has been observed to decrease from 10^{13} to 10^6 sec^{-1} with increasing coverage. However, more recent results suggest the decrease in pre-exponential factor may be largely due to incomplete equilibration of the cesium layer in the shank region of the emitter as discussed earlier in connection with the measurement of ϕ vs. θ . Figure 13 shows a plot of desorption time vs. $1/T$ for a small coverage increment near $\theta = 1.17 \times 10^{14} \text{ atoms/cm}^2$ for cesium on tungsten where the shank was not completely equilibrated. The sharp break in the Arrhenius plot is indicative of a two step process involving different activation energies. The values of the activation energies of the two straight line segments are very close to measured desorption and diffusion activation energies in this coverage region. Apparently at low temperatures the rate of desorption is controlled primarily by diffusion into the emitting region of the tip, while at higher temperatures diffusion paths are sufficiently short so that thermal desorption is rate controlling. This can be more quantitatively stated by employing equation (3) and assuming that the diffusion path y is less than 2000 Å (approximately

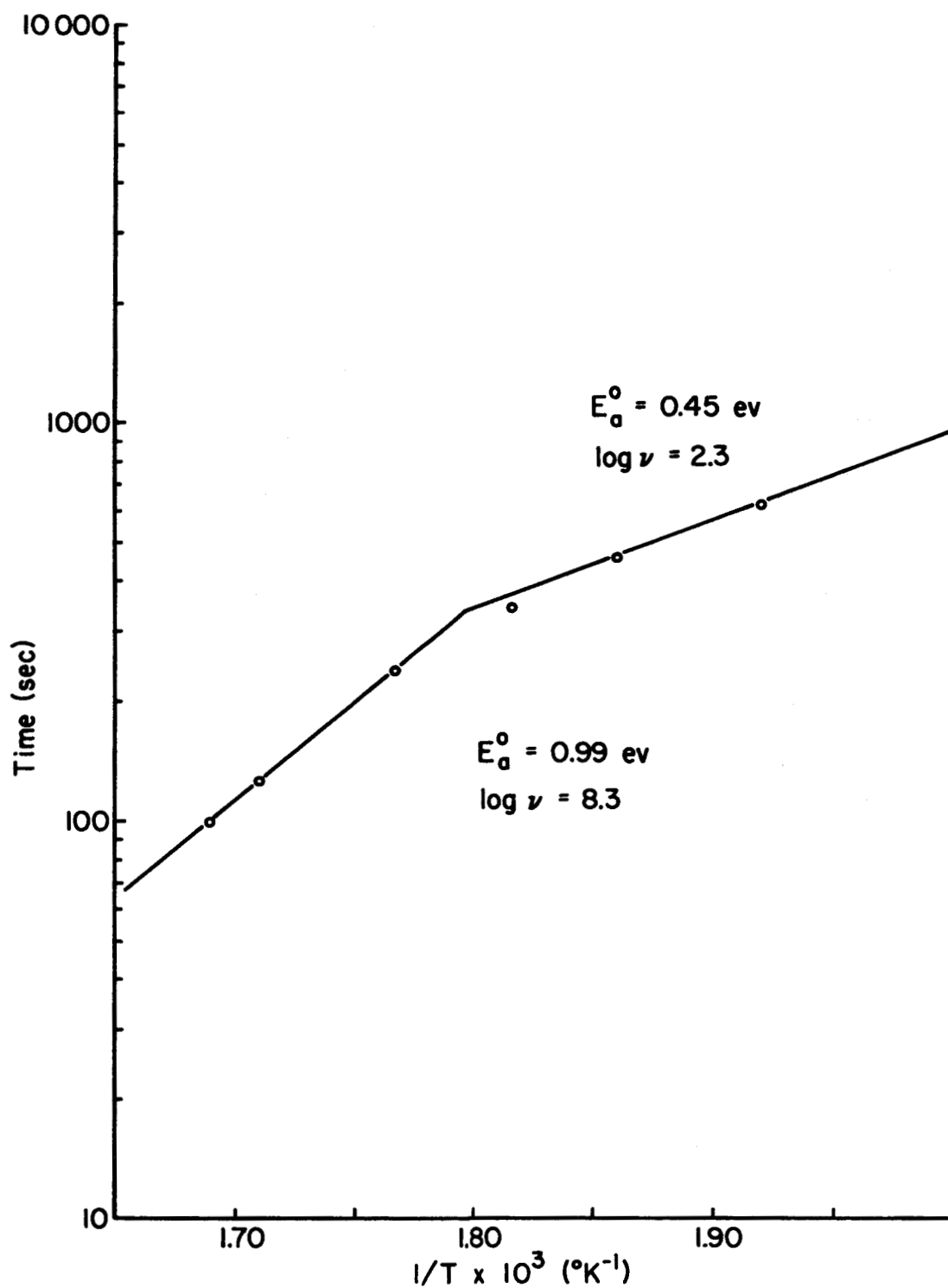


Figure 13. Desorption time t vs $1/T$ for a small coverage increment near $\sigma = 1.17 \times 10^{14} \text{ atoms/cm}^2$ for cesium on tungsten where the shank was not completely equilibrated.

equal to the tip radius) and using a value of $a = 5 \text{ \AA}$; accordingly a value of $E_a^0 - E_d^0 = 0.58 \text{ eV}$ is obtained at $T = 560^\circ\text{K}$ (the point of intersection of the two straight lines of Figure 13). Since the difference between the two activation energies given in Figure 13 is 0.54 eV , in close agreement with that calculated by equation (3), it is apparent that the model is correct and that unequilibrated cesium in the shank region of the emitter can complicate the measurement of desorption energies.

That the problem of incomplete equilibration of the cesium layer can alter the pre-exponential factor ν of equation (24) was confirmed by measuring the activation energy for desorption of cesium from tungsten at a coverage of $\theta = 2.7 \times 10^{14} \text{ atoms/cm}^2$ where care was taken to insure complete equilibration of the cesium layer by excess dosing of the emitter followed by a low temperature spread and thermal desorption to the initial point of the rate run. An activation energy of 0.80 eV and a pre-exponential of 10^{12} sec^{-1} was determined. In past work when shank equilibration was not established, much lower values of ν were obtained in this coverage region. Figure 14 shows a revised graph of the variation of neutral desorption energy vs. coverage for cesium on tungsten based on recent data and utilizing the $\theta - \phi$ relationship of Figure 8. It can be seen that the desorption energy decreases monotonically with increasing coverage as noted previously¹; however, it does not go below the heat of vaporization of bulk cesium, which is 0.69 eV .

Cesium Ion Desorption

At very low cesium coverages, such that $\theta(\phi) > V_I$, it has been possible to utilize the field emission microscope to measure ionic desorption energies by applying a negative bias to the pulse field emission viewing voltage. This has been performed previously for cesium on tungsten¹, and more recently for cesium on molybdenum, obtaining values of 2.4 ± 0.1 and $2.2 \pm 0.1 \text{ eV}$. These results are within experimental error of those predicted by the empirical relationship between E_p^0 and ϕ_s given in equation (23) and thus confirm the relationship at least for these two substrates.

If one assumes adsorption is totally ionic at the terminal coverage, the following theoretical expression can be derived

$$E_p = \phi_s - I + \frac{e^2}{4x_p} \quad , \quad (25)$$

which relates the ionic adsorption energy to the equilibrium bond distance x_p of the adsorbate. Using the cesium ionic radius in equation (25) the following expression is obtained:

$$E_p = \phi_s - 2.16, \quad (26)$$

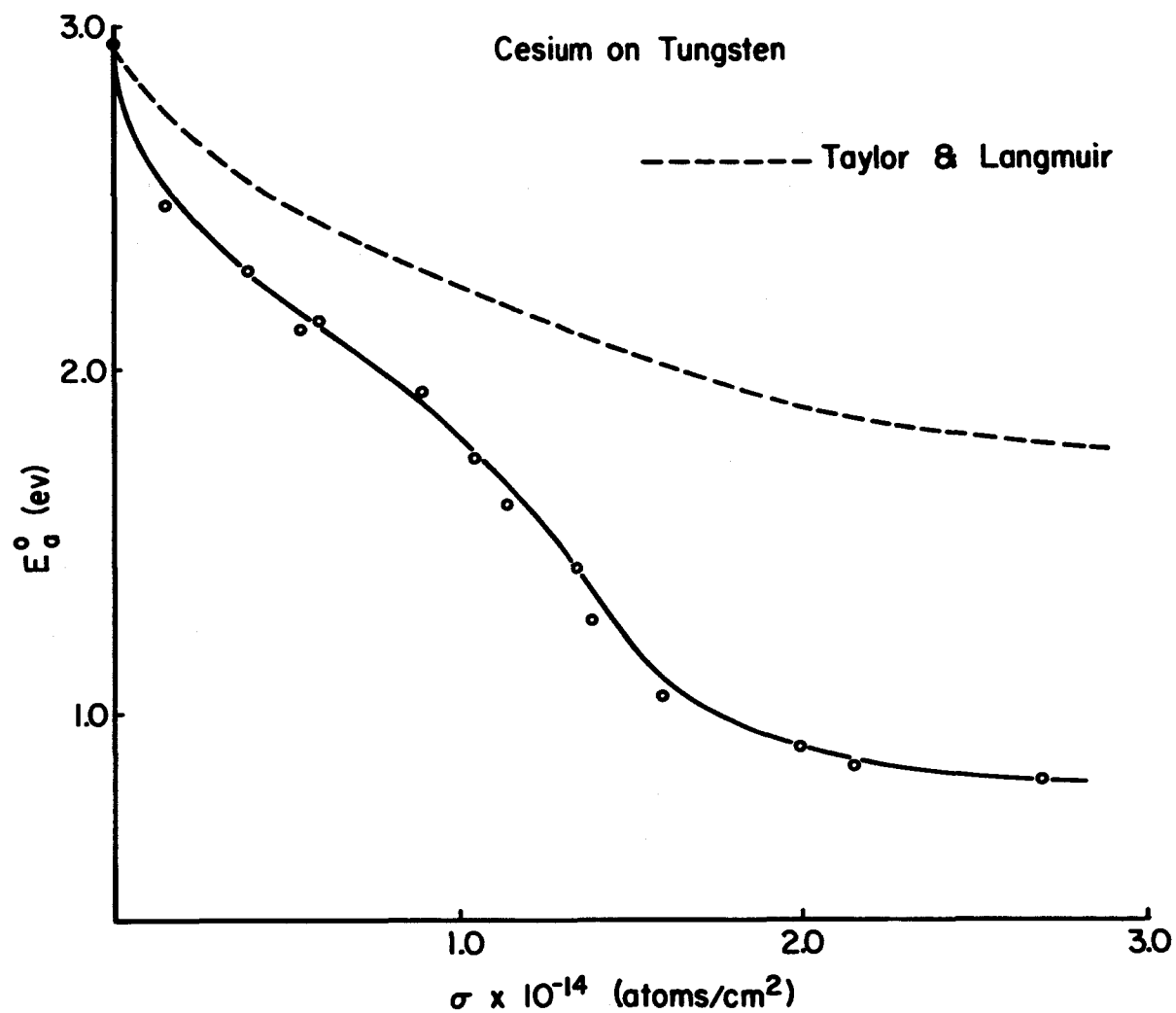


Figure 14. Variation of neutral desorption energy vs coverage for cesium on tungsten utilizing the $\phi - \sigma$ relationship of Figure 8.

which is in excellent agreement with the empirically determined relationship of equation (23). This result suggests the generally expected conclusion that the bond between cesium and refractory substrates is mainly ionic at the terminal coverage. However, it must be emphasized that the ionic character of the bond at low cesium coverage does not necessarily exist at higher degrees of cesium coverage; in fact, most of the evidence compiled thus far suggests that the adsorbed cesium is largely atomic in nature at coverages in excess of 0.15 monolayer.

The Effect of Oxygen

The previously reported studies¹ of the desorption of cesium from tungsten at initial oxygen coverages corresponding to initial work functions (ϕ_{ow}) of 4.62 and 5.65 eV have been extended to include additional initial oxygen coverages corresponding to ϕ_{ow} of 4.55 and 5.16 eV. Variation of cesium coverage with temperature (using results of Figure 10), starting with an initially cesium-covered tip, was determined for the latter two underlying oxygen coverages. The results shown in Figure 15 can be interpreted as follows: the temperature at a given cesium coverage is roughly proportional to the activation energy of desorption; therefore, the curves all show a monotonic decrease in the desorption energy of neutral cesium with increasing coverage. The interesting feature of these results is the apparent reversal of the magnitudes of the desorption energies in the mid-coverage range. For example, at low cesium coverage it appears that the substrate with the highest oxygen content binds the cesium most tightly at a given cesium coverage, whereas at high cesium coverages the reverse is true. It should be mentioned, however, that for temperatures above 700 to 900°K (depending on oxygen coverage) the adsorption and desorption of cesium from an oxygen-covered tungsten substrate, which had been previously heated to approximately 500°K prior to cesium desorption, is no longer completely reversible as judged by pattern and work function changes. This is attributed to the onset of irreversible tungsten oxide formation.

In one experiment involving thermal desorption of cesium from oxygen-covered tungsten ($\phi_{ow} = 5.16$ eV), the tip was biased so as to allow cesium ions to be desorbed; the desorption, which occurred at $T = 905^\circ\text{K}$ and an initial cesium coverage of 0.37×10^{14} atoms/cm², was allowed to proceed to complete removal of cesium as judged by work function and pattern changes. The work function and pattern obtained after complete cesium removal were identical to those obtained from the initial oxygen-covered tungsten surface prior to cesium deposition. These results and the general reversibility of the cesium adsorption at temperatures below which incipient oxide formation occurs provide conclusive evidence that cesium can be desorbed in either neutral or ionic form without disturbing the underlying chemisorbed oxygen layer. Thus, if a Cs-O-W complex occurs on certain crystallographic planes of the surface the Cs-O bond is broken without disturbing the bonding between the oxygen and tungsten surface.

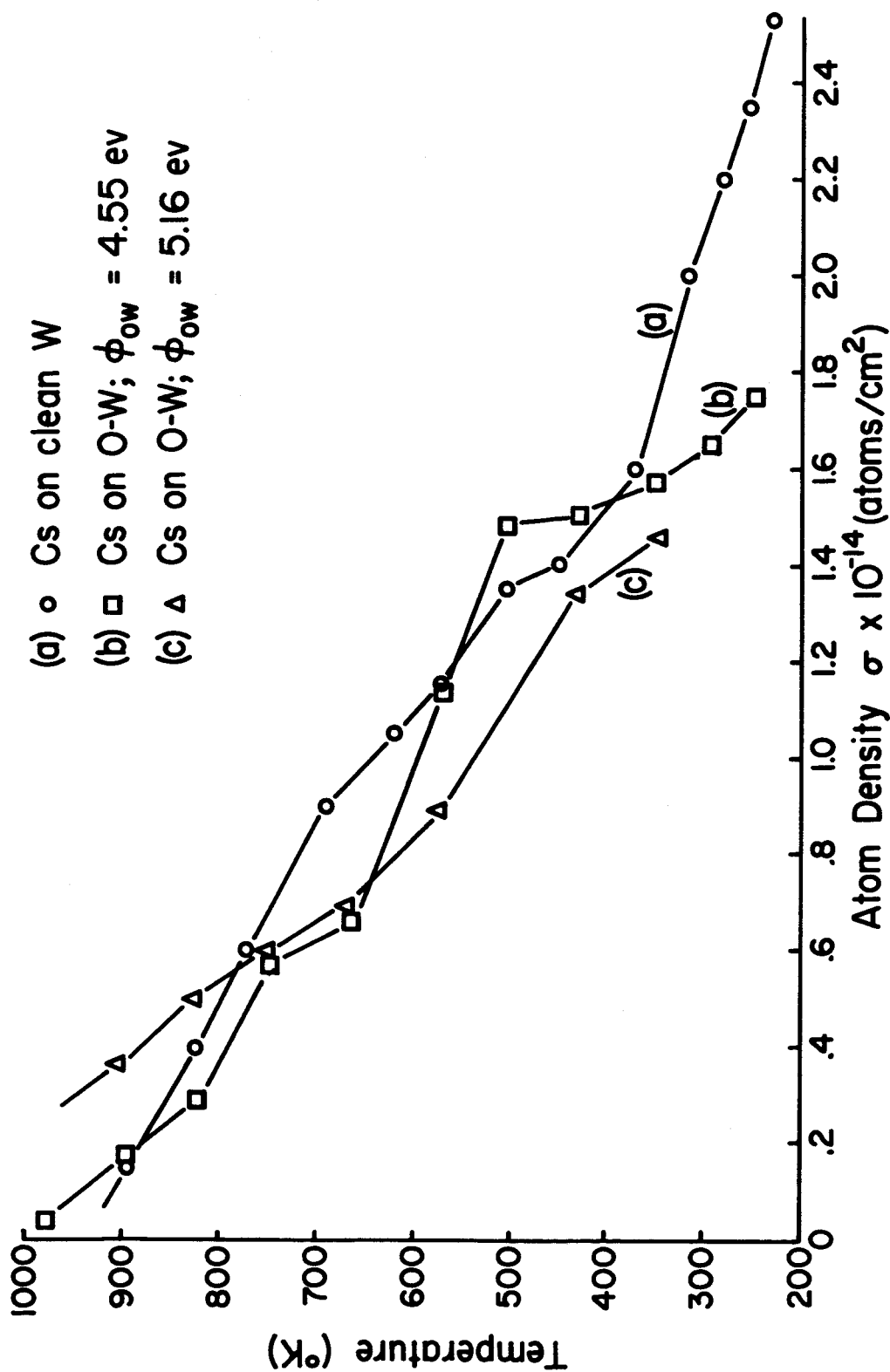


Figure 15. Desorption temperature vs coverage for cesium from tungsten at various underlying oxygen coverages, heating at 60 second intervals.

Utilizing the results of Figure 15 in connection with equation (24), it was possible to make a rough estimate of the activation energy of neutral desorption for various underlying oxygen coverages. These results are given in Table IV at cesium coverages σ_c corresponding to $V_I - \phi = 0$; also in a similar fashion estimates of the desorption energy for ions were made. According to equation (22), since $V_I - \phi = 0$, the difference $E_p^o - E_a^o$ should also equal 0. This appears to be approximately true, although it must be remembered that the temperatures involved in the latter measurements are all above 700°K and thus in the region where the complicating onset of incipient oxide formation occurs.

In order to shed more light on the specific role of oxygen in the complex Cs-0-W system, it was felt that a brief study of the 0-W system should be made. Inasmuch as extensive studies of this system by field emission microscopy have been reported^{23,24}, this study was brief and primarily devoted to an investigation of the pattern and work function changes under various conditions of oxygen concentration and temperature. Figure 16 shows the variation of ϕ with temperature of an initially heavily oxygen-covered tungsten surface. It can be noted from Figure 16 that a temperature in excess of 1800°K is necessary to completely remove the adsorbed oxygen and that the measured field emission work function drops below that of clean tungsten (4.52 ev) and then approaches it from below. Figure 17 shows the corresponding change in the field emission pattern as oxygen is thermally desorbed from the tungsten surface. It is interesting to note that photo (d) of Figure 17 shows an emission distribution remarkably similar to clean tungsten in spite of the obvious presence of a large coverage of oxygen.

TABLE IV

Comparison between Cesium Ion and Neutral Desorption Energies from 0-W

$\phi_{ow}(\text{ev})$	$\sigma_c \times 10^{-14}(\text{atoms}/\text{cm}^2)$	$E_p^o(\text{ev})$	$E_a^o(\text{ev})$
4.52 (clean)	0.16	2.40	2.48
4.55	0.13	2.34	2.55
5.1	0.26	2.65	2.66

The apparent reduction of work function below that of clean tungsten observed in the high temperature desorption of oxygen is generally believed to be an artifact of the surface due to the formation of oxide build-up; this causes a change in the field factor which, by the determination of work function from the Fowler-Nordheim equation, manifests itself in an apparent decrease in work function.

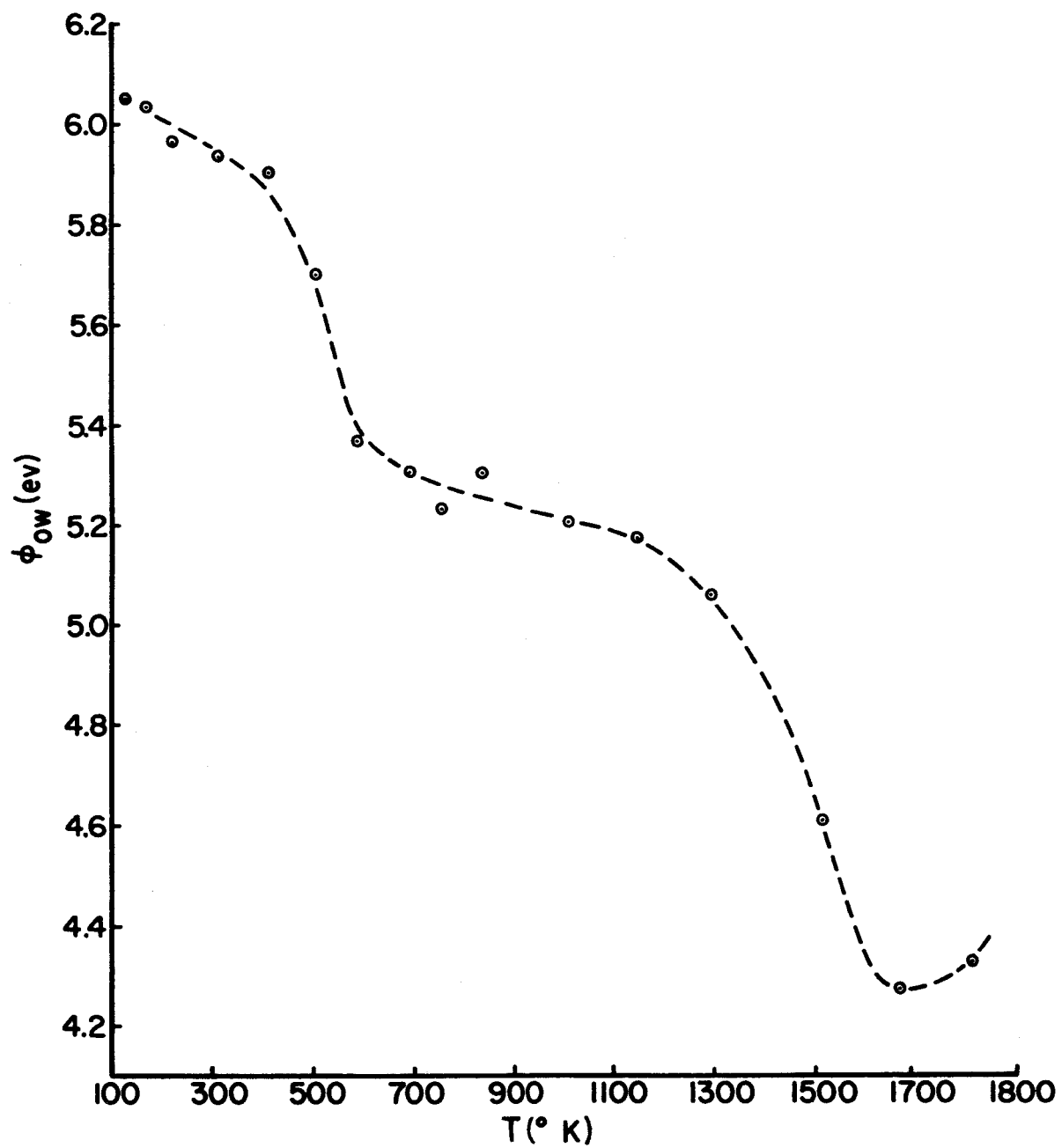
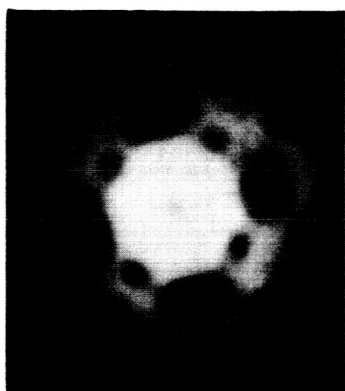
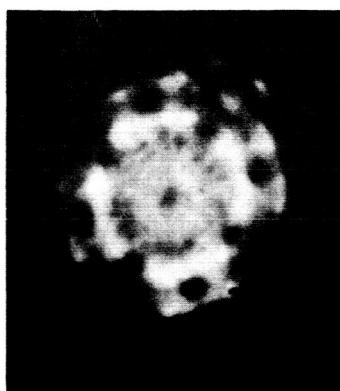


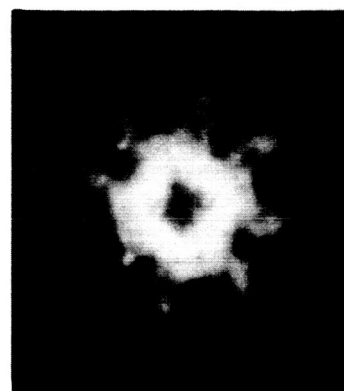
Figure 16. Work function vs. heating for 60 second intervals at the indicated temperatures for oxygen on tungsten.



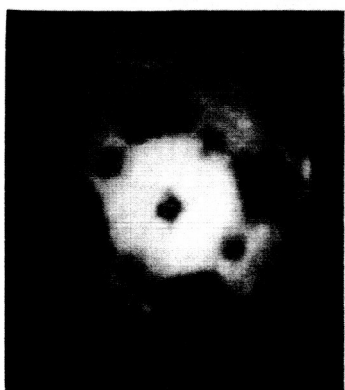
(a)
Clean Tungsten



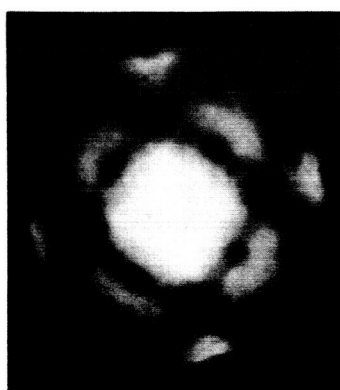
(b)
 $\theta = 6.10 \text{ ev}$
 $T = 130^\circ \text{ K}$



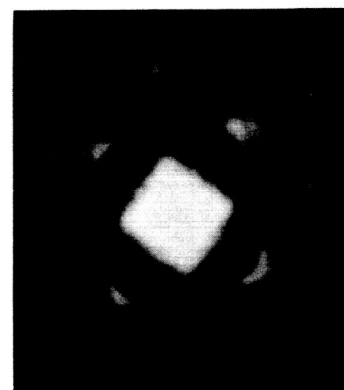
(c)
 $\theta = 5.70 \text{ ev}$
 $T = 507^\circ \text{ K}$



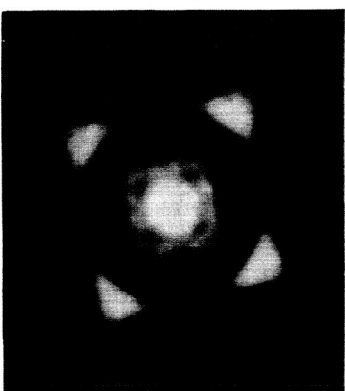
(d)
 $\theta = 5.37 \text{ ev}$
 $T = 591^\circ \text{ K}$



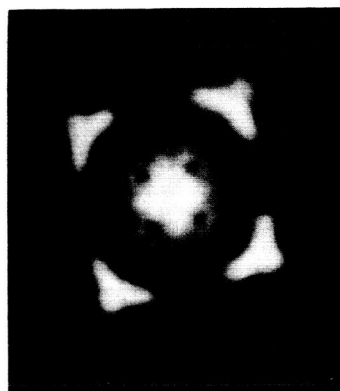
(e)
 $\theta = 5.20 \text{ ev}$
 $T = 1010^\circ \text{ K}$



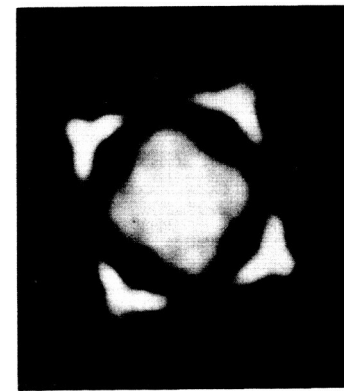
(f)
 $\theta = 5.06 \text{ ev}$
 $T = 1294^\circ \text{ K}$



(g)
 $\theta = 4.61 \text{ ev}$
 $T = 1511^\circ \text{ K}$



(h)
 $\theta = 4.27 \text{ ev}$
 $T = 1662^\circ \text{ K}$



(i)
 $\theta = 4.33 \text{ ev}$
 $T = 1809^\circ \text{ K}$

Figure 17. Typical field emission patterns showing the thermal desorption of oxygen initially deposited on tungsten at 77° K . These patterns were selected from a sequence of patterns that were taken after tungsten emitter had been heated to successively higher temperatures for 60 second periods.

Finally, a comparison of the pattern changes between cesium on oxygen-covered tungsten and oxygen on tungsten allows one to determine the temperature at which cesium is completely removed from the 0-W surface and one is left an oxidized tungsten surface. The similarities between photo (g) of Figure 17 and photo (h) of Figure 18 clearly indicate the latter to be completely free of cesium at 1328°K, while still retaining some adsorbed cesium at 1082°K.

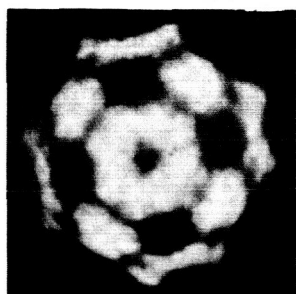
RESULTS OF SURFACE DIFFUSION OF CESIUM ON VARIOUS REFRACTORY METALS

The surface diffusion studies of cesium on molybdenum, tungsten, and rhenium substrates at various initial cesium coverages and with several values of applied electric field have been performed and reported previously¹. Such studies are also currently being extended to platinum substrates. Interesting information concerning the effect of substrate atomic structure on surface diffusion rates heretofore not available has been obtained by utilizing the unique features of the field emission microscope, which allow study of surface diffusion on various crystallographic planes of a particular substrate. Briefly, it was found that at low cesium coverages activation energies of surface diffusion were large (e.g., about 0.76 ev on the {100} regions of tungsten) on the atomically rough planes of a particular substrate and small (e.g., as low as 0.36 ev on the {110} regions of tungsten) on the atomically smooth planes.

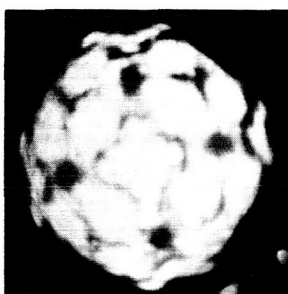
It has been reasoned¹ from the experimental results that two mechanisms of surface migration are operative depending on the coverage range. For example, at low degrees of coverage ($\theta < 1$) migration rates are governed by the potential barriers encountered in site to site migration and therefore vary with the atomic detail of the surface under consideration. On the other hand, at high degrees of coverage ($\theta > 1$) migration occurs at lower temperatures and with lower activation energies and is governed by second layer cesium migration over a chemisorbed layer, thus making this migration mode less sensitive to the substrate atomic structure.

It was found¹ that the temperature required for migration of a controlled amount of cesium over a previously partially covered surface reached a maximum when the underlying cesium-covered surface corresponded to the minimum in work function (see Figure 10). Also it was observed¹ that a single dose of cesium diffused across the field emitter by what appeared to be a separation into two sharply divided high and low concentration phases when the initial coverage of the half-covered tip exceeded 0.7 monolayer.

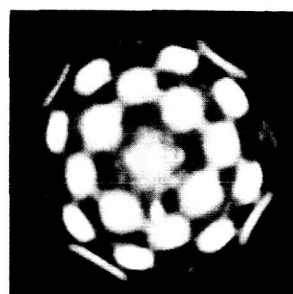
A crude theoretical model of the adsorbed cesium layer incorporating both attractive and repulsive lateral forces given earlier indicated the likelihood of a two dimensional phase change or transition to a state of long



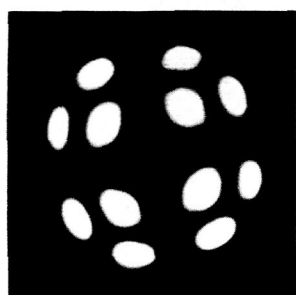
$T = 345^{\circ}\text{K}$
 $\phi = 1.351 \text{ eV}$
 (a)



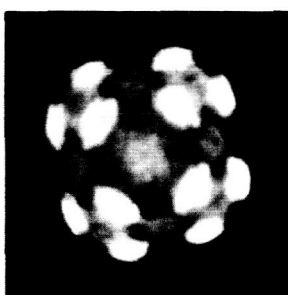
$T = 515^{\circ}\text{K}$
 $\phi = 1.13 \text{ eV}$
 (b)



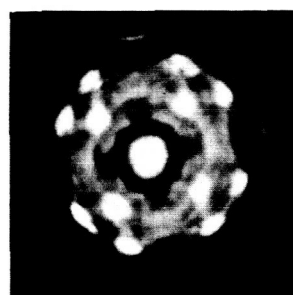
$T = 575^{\circ}\text{K}$
 $\phi = 1.495 \text{ eV}$
 (c)



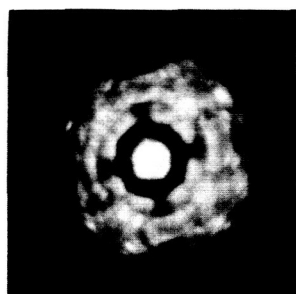
$T = 656^{\circ}\text{K}$
 $\phi = 1.61 \text{ eV}$
 (d)



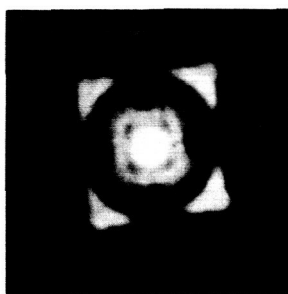
$T = 732^{\circ}\text{K}$
 $\phi = 2.27 \text{ eV}$
 (e)



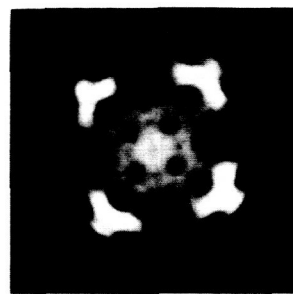
$T = 963^{\circ}\text{K}$
 $\phi = 3.51 \text{ eV}$
 (f)



$T = 1082^{\circ}\text{K}$
 $\phi = 4.52 \text{ eV}$
 (g)



$T = 1328^{\circ}\text{K}$
 $\phi = 4.86 \text{ eV}$
 (h)



$T = 1546^{\circ}\text{K}$
 $\phi = 4.565 \text{ eV}$
 (i)

Figure 18. Variations in pattern and work function caused by 60 second heating of a cesium covered substrate at indicated temperatures. Substrate was initially covered with oxygen ($\phi_{\text{ow}}=5.65 \text{ eV}$) and heated to 493°K .

range order. Besides the striking visual evidence of the phase change seen in the field emission patterns, it is now also possible to use the concept of a phase change to explain the maximum in the temperature required for surface diffusion which occurs at σ_m for the various substrates investigated. The latter will be discussed in the succeeding sections.

Recent Results on Molybdenum

In order to ascertain whether the maximum in the temperature for surface diffusion at σ_m is due to a maximum in the activation energy of surface diffusion, experiments were conducted to measure the activation energy for complete equilibration of a small dose of cesium with various underlying coverages of cesium already present. These experiments were performed on a molybdenum substrate in three different coverage ranges by first equilibrating the cesium layer at the desired coverage and then depositing a small dose on one side of the field emitter and measuring the time required to completely spread this latter dose at a particular temperature. The emitter was then heated in order to thermally desorb the excess cesium back to the original starting coverage and the preceding sequence repeated several times at other temperatures. The data was analyzed according to the following expression

$$\text{Log } \tau_s = \text{Log } \frac{y^2}{D_o} + E_d^o \times 10^4 / 1.98T \quad (27)$$

where τ_s is the time in seconds required for the cesium to travel a distance y (which in this case is about 8000 Å), and where D_o is the diffusivity and E_d^o , the activation energy in ev. The constants measured for equation (27) in the various coverage ranges are given in Table V.

TABLE V

Variation of the Activation Energy and the Diffusivity Constant of Surface Diffusion with Cesium Coverage on a Molybdenum Substrate

Coverage Range ($\sigma \times 10^{-14}$ atoms/cm ²)	E_d (ev)	Log y^2/D_o
0 - 0.1	0.43 ± 0.02	-6.6 ± 0.3
1.3 - 1.4	0.43 ± 0.02	-5.2 ± 0.3
1.9 - 2.3	0.37 ± 0.02	-5.9 ± 0.3

The results show that the maximum observed earlier in the temperature for equilibration at $\sigma_m = 1.9 \times 10^{14}$ atoms/cm² is not due to an increase in the activation energy, but rather to a decrease in the diffusivity D_o .

Discussion of Results

We have previously¹ pictured the adsorbed cesium as an imperfect two-dimensional gas in the temperature and coverage ranges where surface diffusion is rapid and thermal desorption is negligible. In this temperature range the emission distribution and, hence, the coverage distribution appeared independent of temperature so that work function measurements normally made at 77°K, where cesium is immobile on all substrates studied, reflect accurately the coverage distribution at higher temperatures where mobility is appreciable. In picturing the cesium as a two-dimensional gas we assumed the adsorbed cesium to be non-localized, i.e., possessing two degrees of translational freedom parallel to the surface. As pointed out by Tompkins²⁵ it is possible for an ad-atom to be localized but still execute lateral mobility by a series of jumps over the finite potential barrier separating adjacent sites. Whether the ad-atoms are localized to a particular site or non-localized and possess free two-dimensional translation will lead to slightly different equations of state of the ad-layer (see reference 26 for a more complete discussion of this).

For the purpose of illustrating theoretically the possibility of a phase change at a critical coverage and temperature, we formerly¹ used a two-dimensional equation of state which resembled a three-dimensional van der Waals equation of state. Such an equation of state can be derived simply by first writing the canonical partition function Q for a system of N non-localized ad-atoms moving independently in an area, S , in terms of the single particle (microcanonical) partition function q as

$$Q = q^N / N! \quad (28)$$

where

$$q = S / \lambda_a^2, \quad \lambda_a = h / (2 \pi m k T)^{1/2} \quad (29)$$

In order to derive the two-dimensional van der Waals equation of state we make two modifications in q , both arising from intermolecular forces. First, we assume the ad-atoms to be hard spheres so that the total area S in equation (29) should be replaced by the free area S_f available to the N ad-atoms which we consider to be

$$S_f = S_0 - S, \quad (30)$$

where S_0 is the total area occupied at the monolayer condition. Second, we assume each ad-atom moves independently in a uniform potential field provided by the surface interactions and the other ad-atoms, with the latter being distributed in a random manner. Therefore, a Boltzman factor,

$e^{-w/2kT}$, is inserted to take care of the intermolecular potential field w in which a given ad-atom is moving; the expression for q thus is written as

$$q = \frac{(S_o - S)}{\lambda_a^2} e^{-w/2kT} . \quad (31)$$

The factor two in the exponential is inserted because each pair interaction w has to be shared between two ad-atoms in summing over all pair-wise interactions. Recalling from statistical thermodynamics the following relation between pressure f (two-dimensional in this case) and Q :

$$f = kT \left(\frac{\partial \ln Q}{\partial S} \right)_{T,N} ; \quad (32)$$

then from equations (28) to (32) we obtain the following expression for f

$$f = NkT/(S_o - S) - \frac{N}{2} \left(\frac{\partial w}{\partial S} \right)_N . \quad (33)$$

Since $S/N = 1/\sigma$ and $\sigma/\sigma_o = \theta$, equation (33) may be written in the form

$$f = \frac{\theta \sigma_o kT}{1 - \theta} + \frac{\theta^2 \sigma_o}{2} \left(\frac{\partial w}{\partial \theta} \right)_N . \quad (34)$$

The analogy with the van der Waals equation can be made by noting that the S_o of equation (33) is comparable to the co-volume term in the three-dimensional case, and the last term of equation (33) is a correction to the spreading pressure due to mutual interactions. It is well known that the van der Waals equation of state predicts a first order phase change by a discontinuity in its f vs S plot; this will be the case in equation (33) if an attractive force term is included in w .

There are strong reasons to believe that in the temperature and coverage range that has been considered in the current investigations the proper model of the adsorbed cesium layer is not one of freely (i.e., non-localized) mobile atoms, but rather a localized ad-layer with restricted mobility. In this model an ad-atom moves a distance y by a series of hops from one lattice site to another, where the time spent between sites separated by a distance " a " is small compared to the total time required. For example, from equation (27) and the results of Table V it can be shown that the time τ_g required to travel one lattice site distance (assumed to be about 5Å) at a temperature of 250°K is approximately 10^{-4} seconds. If, on the other hand, the ad-atoms behave as a freely mobile two-dimensional gas, the time τ_g required to travel the same distance " a " would be

$$\tau_g = \frac{a}{v_d} = \frac{a(2M)^{1/2}}{(\pi kT)^{1/2}} = \frac{5.05}{T^{1/2}} \times 10^{-11} \text{ sec.} \quad (35)$$

where v_d is the two dimensional velocity and M the atomic weight of cesium. At a temperature of 250°K , $\tau_g \approx 10^{-12}$ sec.: thus it is clear that under these conditions only 10^{-8} of the total time τ_s is spent between sites and the rest of the time is attributed to residence time on the site.

In view of the highly localized nature of the ad-layer under the existing experimental conditions, it would be more proper to use two-dimensional lattice gas statistics developed by Hill²⁶ as the correct model. By considering N ad-atoms distributed among N_0 sites, the expression for the canonical partition function for localized adsorption is

$$Q = N_0! q^N / N! (N_0 - N)! \quad (36)$$

In this case q is more properly the single particle partition function of an ad-atom possessing three degrees of vibrational freedom rather than two degrees of translational and one degree of vibrational freedom perpendicular to the surface as was inferred in equation (28). Equation (36) is valid for the case of no interaction between ad-atoms, and in order to account for lateral interactions it is necessary to resort to approximations.

Since we are interested only semi-quantitatively in the behavior of the ad-layer and how the expected lateral interaction might lead to a phase change, we shall employ the Bragg-Williams approximation²⁶ for a two-dimensional lattice gas with lateral interactions. This approximation assumes a random distribution of ad-atoms among the available sites and considers the pair-wise mutual potential energy of nearest neighbors w_1 in terms of the average number of nearest neighbors, \bar{N}_{11} . The net result is the multiplication of equation (36) by a Boltzman term giving a partition function of the form

$$Q = N_0! q^N e^{-\bar{N}_{11} w_1 / kT} / N! (N_0 - N)! \quad (37)$$

From the above equation and equation (32) the expression for the spreading pressure becomes

$$f = - \sigma_0 kT \ln (1-\theta) + \theta^2 \sigma_0 \left(\frac{\partial \bar{N}_{11} w_1}{\partial \theta} \right)_N \quad (38)$$

A functional similarity can be seen between the foregoing expression for f and equation (34) by noting that at low θ the first term in each case approaches $\theta \sigma_0 kT$. In view of the fact that neither of the two approximate expressions for Q can be considered valid for high coverages (i.e., when the condensed phase is formed), we conclude that for low degrees of coverage the localized and non-localized model lead to similar resultant thermodynamical expressions.

In the past we considered two lateral interaction potential energies consisting of a repulsive term w_r , caused by Coulomb repulsion of adjacent dipoles, and an attractive term w_a , involving London or dispersion forces.

The average repulsive potential energy per pair of ad-atoms obtained²⁷ from elementary electrostatics by summing over all pair-wise interactions of a uniform square array of ad-atoms with dipole moment μ and site separation a is

$$w_r = 9.03 \frac{\mu^2}{a^3} \theta \quad (39)$$

By allowing for mutual depolarization which causes μ to vary with θ , the complete expression for w_r becomes

$$w_r = \frac{9.03 \mu_0^2 \theta}{a^3 \left(1 + \frac{9a\theta}{a^3}\right)^2} \quad (40)$$

where μ_0 is the dipole moment at zero coverage and α is the polarizability of the ad-atoms. In the above derivation it is implied that the ad-atoms are localized to definite sites with the probability of occupancy equal to θ . If the ad-atoms are considered as non-localized it would then be proper to make the substitution

$$\sigma = \frac{\theta}{2} \quad \text{in equation (40).}$$

It is now possible to show any expected variations in the diffusion coefficient due to a two-dimensional phase transformation by writing the two-dimensional flux J_d in terms of the gradient of the chemical potential μ_s of the adsorbed layer as follows

$$J_d = \frac{-D \sigma}{kT} \left(\frac{\partial \mu_s}{\partial x} \right)_T \quad (41)$$

and recalling from statistical thermodynamics that the relation between the chemical potential and the canonical partition function is

$$\frac{\mu_s}{kT} = - \left(\frac{\partial \ln Q}{\partial N} \right)_{T, S} \quad (42)$$

For the purpose of this calculation the localized layer partition function equation (37) will be employed, although it should be emphasized that the non-localized layer partition function would lead to the same functional relationships at low degrees of coverage.

The expression for $\bar{N}_1 w_1$, the average interaction energy between nearest neighbors, was evaluated as follows: (1) a square lattice was assumed so that at $\theta = 1$ each ad-atom has four nearest neighbors; (2) the expression for the van der Waals attractive interaction was considered only important for the c_1 nearest neighbors and is written

as

$$\bar{N}_{11} w_a = \frac{c_1 N \theta}{2} \left(\frac{E_b}{6} \right) \quad (43)$$

where the factor $c_1 N \theta / 2$ is the average number of nearest neighbor pairs and E_b is the heat of vaporization of cesium which is divided by 6 in order to normalize the latter to a per bond basis; (3) the lateral energy due to dipole repulsion is a long range interaction and realistically must include contributions from both nearest neighbors and more distant ad-atoms. Equation (40) gives such an expression based on a random distribution of ad-atoms in a square lattice and for N ad-atoms contributes an interaction term of the form

$$\bar{N}_{11} w_r = \left(\frac{N}{2} \right) \frac{0.03 \mu_o^2 a^3}{(a^3 + 9a\theta)^2} \quad (44)$$

The sum of equations (43) and (44) gives the total lateral interaction energy $\bar{N}_{11} w_l$ which, when combined with equations (37) and (42), yields the following expression for the chemical potential of the ad-layer as a function of θ and T

$$\mu_s = kT \ln \frac{\theta}{(1-\theta)q} + \frac{9.03 \theta \mu_o^2 a^3}{(a^3 + 9a\theta)^2} - \frac{81 \theta^2 a \mu_o^2 a^3}{(a^3 + 9a\theta)^3} - \frac{2}{3} \theta E_b \quad (45)$$

Finally, by differentiating the above expression with respect to x , letting θ be the variable, and inserting the result into equation (41), we obtain the following for J_d

$$J_d = -D F_d(\theta, T) \frac{d\sigma}{dx}, \quad (46)$$

where $F_d(\theta, T)$ is a complicated dimensionless function which multiplies the diffusion coefficient; thus, the complete expression for the diffusion coefficient is

$$D = F_d(\theta, T) D_o e^{-E_d^o/kT}. \quad (47)$$

It is evident from equation (47) that any discontinuities in the chemical potential due to a phase change will show up in the diffusion coefficient as a variation in the pre-exponential term when the temperature dependency of D is examined. This does not necessarily rule out concomitant variations in E_d^o as well, which have been assumed constant throughout. Physically, the factor $F_d(\theta, T)$ can be viewed as a sort of entropy term which arises from the correlation (or long range order) in the migrating ad-layer necessarily brought about when proceeding from a dilute to a condensed phase.

The variation of the $F_d(\theta, T)$ term with θ at various temperatures is shown in Figure 19 where the following constants were used: $a = 20\text{\AA}^3$, $\mu_o = 5 \times 10^{-18}$ e.s.u., $\sigma_o = 3.56 \times 10^{14}$ atoms/cm², $a = 5\text{\AA}$, and $E_b = 0.69$ ev.

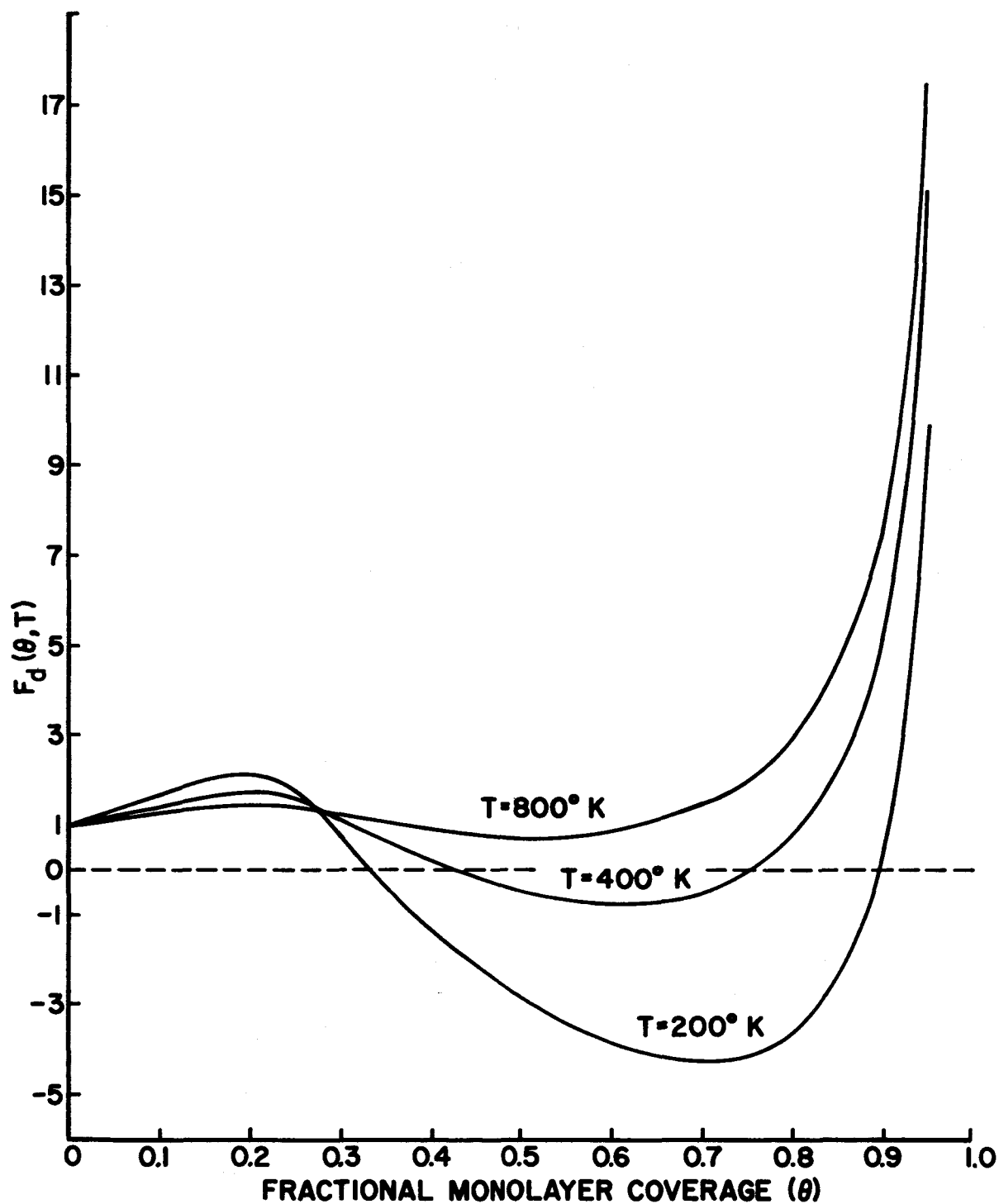


Figure 19. Variation of $F_d(\theta, T)$ (see equation 47) with fractional monolayer coverage at various temperatures.

The prediction of a negative diffusion coefficient can be traced to the attractive van der Waal forces which predominate at higher coverages and are responsible for the formation of the condensed phase. The negative diffusion coefficient prediction stems from the same functional relations that produce the loops in the f vs S plots below the critical temperature and probably would not occur if an exact expression for Q could be evaluated. Nonetheless, it is likely that $F_d(\theta, T)$ would still decrease to a minimum as θ increases even if an exact expression for Q were employed. The rapid rise in $F_d(\theta, T)$ as θ approaches unity is due (in this model) to statistical repulsion as all of the available sites become occupied and, again, would be expected in the case of an exact expression for Q . One would also expect an additional short range repulsive force (not included in the model) as θ approaches unity due to core repulsion.

In conclusion, the remarkable similarities between the experimentally determined equilibration temperature vs coverage curve (see Figure 10 of this report and Figures 4 and 5 of reference 1) and the theoretical predictions of the variation of D with θ a la equation (47) lend further support to the suggested model of the ad-layer and to the validity of the lateral interactions considered. Additional experimental support for this view is given in the results of this section which show that the maximum in the equilibration temperature at θ_m is due to a variation of the pre-exponential factor of equation (47) as predicted by the foregoing model.

THE EFFECT OF ELECTRIC FIELD ON THE EQUILIBRIUM DISTRIBUTION OF CESIUM

While attempting to measure the effect of temperature on field emission work function above 250°K as described earlier, it was discovered that a rapid change in the cesium coverage at the field emission tip occurred which ultimately reached an equilibrium value depending on the magnitude of the electric field. Inasmuch as such a phenomenon might well have an important bearing on voltage breakdown mechanisms, as well as possibly providing further insight into the understanding of the behavior of cesium on refractory metal substrates, it was decided to investigate the observed effect in somewhat greater detail.

Results on Molybdenum and Tungsten

It was not initially obvious whether the change in cesium coverage at the tip was due to the electric field or to the emission current through a Nottingham heating mechanism at the tip. Calculations showed, however, that the latter possibility could be ruled out on the basis of the inability of any appreciable tip heating to occur at the current levels where the effect was noted. That the effect was primarily a field effect was established by noting that the cesium coverage was altered with the reverse field as well; however, in the latter case the effect was reversed, that is, the cesium coverage at the tip increased with increasing field.

The time required to establish a given equilibrium distribution corresponded to the approximate times for migration of cesium a distance of the order of several tip radii. At 300°K the relaxation time, for example, was roughly 30 seconds depending on the coverage range under investigation. If the heating was continued after the rapid change in the coverage at the tip, σ_t , a relatively slow change in σ_t occurred with time. This slow change might be caused by the somewhat longer time required for the cesium coverage in the shank region immediately behind the tip to reach its equilibrium value, because of the longer distances involved and the diminished field in that region. The effect was completely reversible throughout the range of variables investigated; the field could be relaxed and the cesium coverage at the tip would return to its initial coverage with approximately the same time constant observed in initially establishing the field-induced coverage distribution. In some cases where the initial coverage was not re-established quantitatively, it was felt that insufficient time was allowed for rearrangement of the cesium over the total tip and shank surfaces.

On the basis of the above experimental observations, we conclude that simultaneous desorption of the adsorbed cesium was not occurring during these observations. This can, of course, be justified theoretically inasmuch as the range of variables of field strength, temperature and coverage studied were generally well within the region where thermal and field desorption were negligible.

The results obtained to date are shown in Figure 20 and consist of the measurement of the coverage ratio at the tip to that of the shank as a function of field strength for molybdenum and tungsten substrates in various coverage ranges. The coverage at the emitter was determined by utilizing the known relationships between work function and coverage. The former was measured as a function of field after time rate of change of the emission current at a particular field became negligible. The unequal coverage distribution was effectively "frozen in" by reducing the temperature to 77°K while the electric field remained fixed, since at this temperature diffusion is negligible. A work function measurement taken at 77°K yielded the coverage corresponding to the particular value of electric field, since the field emission current change on cooling was small compared to the total change and could be accounted for by the previously mentioned small temperature effect on work function and by the normal thermal enhancement of field emission. Because the field is not completely uniform over the entire emitting region of the tip, but decreases about 15% with angular separation from the tip apex to the edge of the emitting region, it is possible that a slight field-induced concentration gradient may be frozen in over the latter region and may alter somewhat the experimental $\phi - \sigma$ relationships used to determine tip coverage. However, in view of the smallness of the field variation over the emitting region it is unlikely that this effect is large, particularly so since it was not obvious from the field emission patterns that an excessive concentration gradient was formed over the emitting region by the field effect.

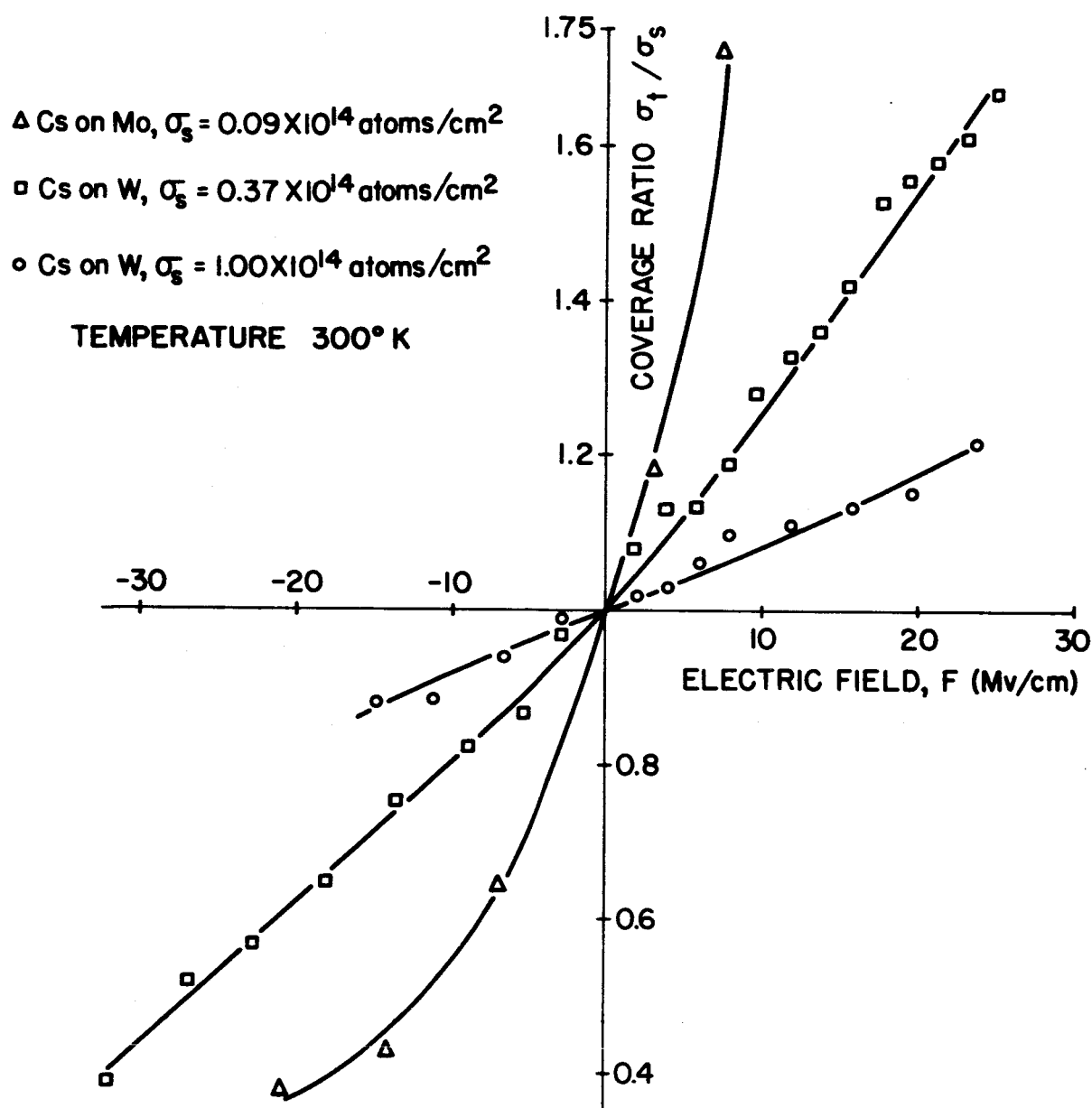


Figure 20. Variation of the ratio of cesium coverage at the emitter tip σ_t and shank σ_s with applied field F .

The coverage on the zero field region of the shank, ϕ_s , should not be altered by the change in coverage at the tip because of the large ratio of the former to the latter which is of the order of 10^6 . Therefore, we assumed that the coverage in the near zero field region of the shank was unchanged when the shank and tip regions were completely equilibrated for a given field in the emitting region of the tip.

The limits of the range of field strengths accessible to this study are limited by excessive field emission on the negative side and field desorption on the positive side. The upper limit of temperature is dictated by the onset of excessive thermal desorption at the particular coverage range under consideration. The high field limits for the positive fields shown in Figure 20 were carried out to the point where field desorption became apparent. Fortunately, the onset of field desorption is quite rapid and can be determined easily since it quickly leads to a runaway process until the entire high field region of the tip is free of cesium; the reason for this will be discussed in a later section.

Finally, it should be mentioned that at temperatures where the cesium layer was immobile (i.e., temperatures below 200°K) no effect of field on the cesium coverage was observed. Also, when pulsed fields of low duty factor ($< 10^{-4}$) are applied, no change in the cesium distribution was observed throughout the entire temperature range of cesium adsorption and desorption.

Discussion of Results

The results of the effect of field on the cesium coverage clearly indicated the process to be thermodynamically motivated and kinetically controlled by the rate of surface migration. The application of a field apparently alters the chemical potential in the high field region while not affecting the chemical potential in the zero field region on the shank. Since thermodynamic equilibrium requires equal chemical potential in both the high and zero field regions of the emitter, the surface concentration of cesium re-arranges until the thermodynamic imbalance is removed. These considerations can be expressed more quantitatively by postulating the following first order interactions between the applied field and the cesium layer: (1) the interaction between the field and dipole moment of the ad-atom contributes a term $\pm\mu F$ to the potential energy of the ad-atom depending on the relative sign of the dipole moment and field; (2) the applied field can induce an additional dipole moment on the polarizable ad-atom and contributes an additional term $\frac{a}{2} F^2$. Thus, the contribution to the potential energy, w_F , of an ad-atom due to the high field is

$$w_F = - |\mu| F - \frac{a}{2} F^2 . \quad (48)$$

In order to determine the relation between the change in cesium coverage

with field we use equation (45) as the expression for the chemical potential of the ad-layer and add equation (48) to the chemical potential expression for the high field region of the tip. For equilibrium to exist within the ad-layer between the high and zero field regions the chemical potentials must be equal; this then leads to the following relation between the coverage in the high field region, σ_t , and the zero field region, σ_s :

$$kT \ln \left[\frac{\sigma_t}{\sigma_s} \left(\frac{\sigma_o - \sigma_s}{\sigma_o - \sigma_t} \right) \right] = E_a^o(\sigma_t) - E_a^o(\sigma_s) + \frac{a}{2} F^2 + |\mu| F \quad (49)$$

where $E_a^o(\sigma_t)$ and $E_a^o(\sigma_s)$ should be approximately equal to the coverage dependent zero field desorption activation energies. Equation (49) can be further simplified by noting that over most of the field and coverage range investigated, the $\frac{a}{2} F^2$ term can be neglected when compared with other terms of equation (49).

The validity of the above model can be tested by letting $\Delta E = E_a^o(\sigma_t) - E_a^o(\sigma_s)$ and plotting the data of Figure 20 in the form $kT \ln \left[\frac{\sigma_t}{\sigma_s} \left(\frac{\sigma_o - \sigma_s}{\sigma_o - \sigma_t} \right) \right] - \Delta E$ vs F ; the slope of the resulting straight line yields a value for μ . Figure 21 shows the data plotted in this fashion for cesium on tungsten, using the $E_a^o(\sigma)$ data of Figure 14; reasonably good straight lines are obtained from which values for μ of 3.7 and 4.3×10^{-18} esu were determined at cesium coverages of 1.00 and 0.37×10^{14} atoms/cm² respectively. Throughout the field and coverage range investigated $\Delta E \gg kT \ln \left[\frac{\sigma_t}{\sigma_s} \left(\frac{\sigma_o - \sigma_s}{\sigma_o - \sigma_t} \right) \right]$ so that the values of μ hinge critically on the accuracy of $E_a^o(\sigma)$ data. Values of μ determined at these coverages by the Helmholtz equation are generally a factor of 2 greater than those determined by the field effect. Since both methods of determining μ involve averages whose weighting factors are different, the order of magnitude agreement between the μ values determined by the two methods lends support for the mechanism suggested by equation (49).

The reason for the much smaller field effect at the higher cesium coverage as shown in Figure 20 is probably due to a decrease in average μ with increasing σ which stems from the larger contribution of mutual depolarization effects at higher coverage. Thus, only mobile adsorbates exhibiting large dipole moments would be expected to show an appreciable variation of the equilibrium coverage with applied field.

EFFECT OF FIELD ON THERMAL DESORPTION

Increasing the value of negative applied field from 6.0 to 13.0 Mv/cm causes a decrease in the activation energy of desorption E_a^F of neutral cesium from tungsten at zero coverage from 2.95 to 2.86 ev which is almost within experimental error. Assuming $\mu = 10 \times 10^{-18}$ esu at low coverage, one would predict a decrease in E_a^F of 0.1 ev due to the μF interaction in

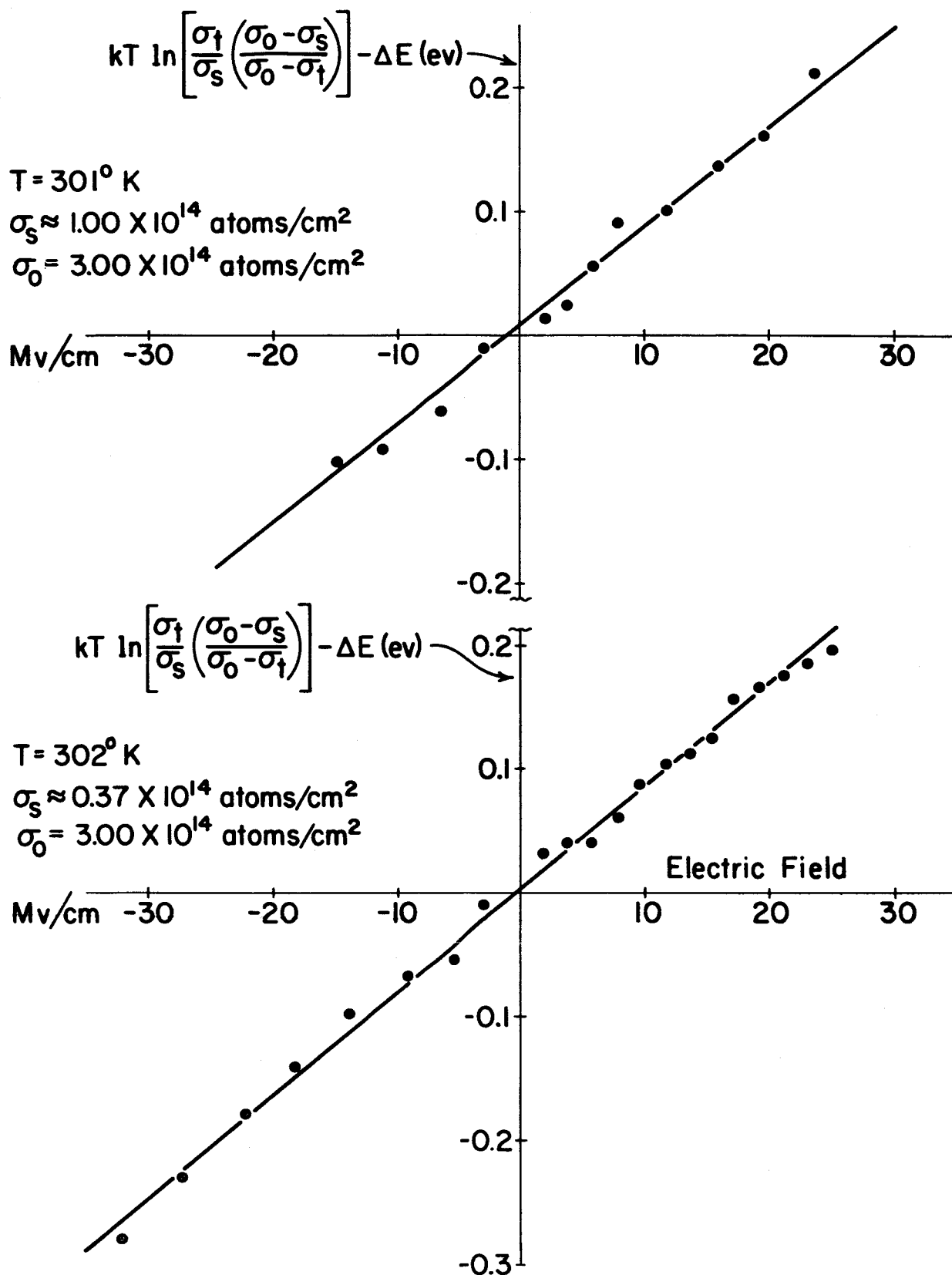


Figure 21. Data of Figure 20 plotted according to equation 49.

agreement with the direction and magnitude of the observed change.

The effect of positive field on thermal desorption (better known as field desorption) has been investigated for a variety of systems^{28,15} including cesium on tungsten at low coverage²⁹, and recently treated theoretically²² for various types of adsorption. We have carried out such a study for cesium on tungsten semi-quantitatively over the coverage range 0 to 1 monolayer and quantitatively at high coverages (i.e., $\sigma = 2.9 \times 10^{14}$ atoms/cm²).

Results on Tungsten

Including only the reduction of the Schottky saddle for desorption of ions and neglecting all other field interactions, it can be deduced from Figure 22 that the variation of desorption energy E_p^F of a singly charged ion +e with positive field is

$$E_p^F = E_a^0 + V_I - \phi - e^{3/2} F^{1/2}, \quad (50)$$

where E_a^0 is the zero field desorption energy for neutral atoms. The rate constant k_p for field desorption is therefore given by

$$k_p = \nu s \exp(-E_p^F / kT), \quad (51)$$

where ν is the usual frequency factor and s is a complicated function involving transition probabilities and/or entropy effects.

The changes in the field emission pattern during cesium desorption from a partially covered (100) oriented tungsten emitter shown in Figure 23 indicate that desorption occurs successively from planes with locally decreasing ϕ ; this means variation in ϕ from plane-to-plane override variations in E_a^0 in equation (50) in determining the local activation energies and hence rates of field desorption. Also, the selectiveness of removal indicates that desorption occurs from an immobile cesium layer under these conditions.

Figure 24 gives the fields required to initiate desorption over a range of cesium coverages. The maximum in desorption field occurs near the work function minimum in agreement with equation (50) provided that the decrease in ϕ with σ is larger than the combined decrease in E_a^0 and other omitted terms in equation (50). In general, the known variations of E_a^0 and ϕ with σ confirm these explanations. On the other hand, the relatively large change in desorption field between 1.20 and 1.35×10^{14} atoms/cm² cannot be explained by changes in ϕ and E_a^0 alone, but must involve significant contributions from other terms, since compensating changes occur in ϕ and E_a^0 in this coverage range. Evaluation of E_p^F as a function of field in this coverage range was attempted by analyzing the temperature dependence of the rates of field desorption according to equation (51).

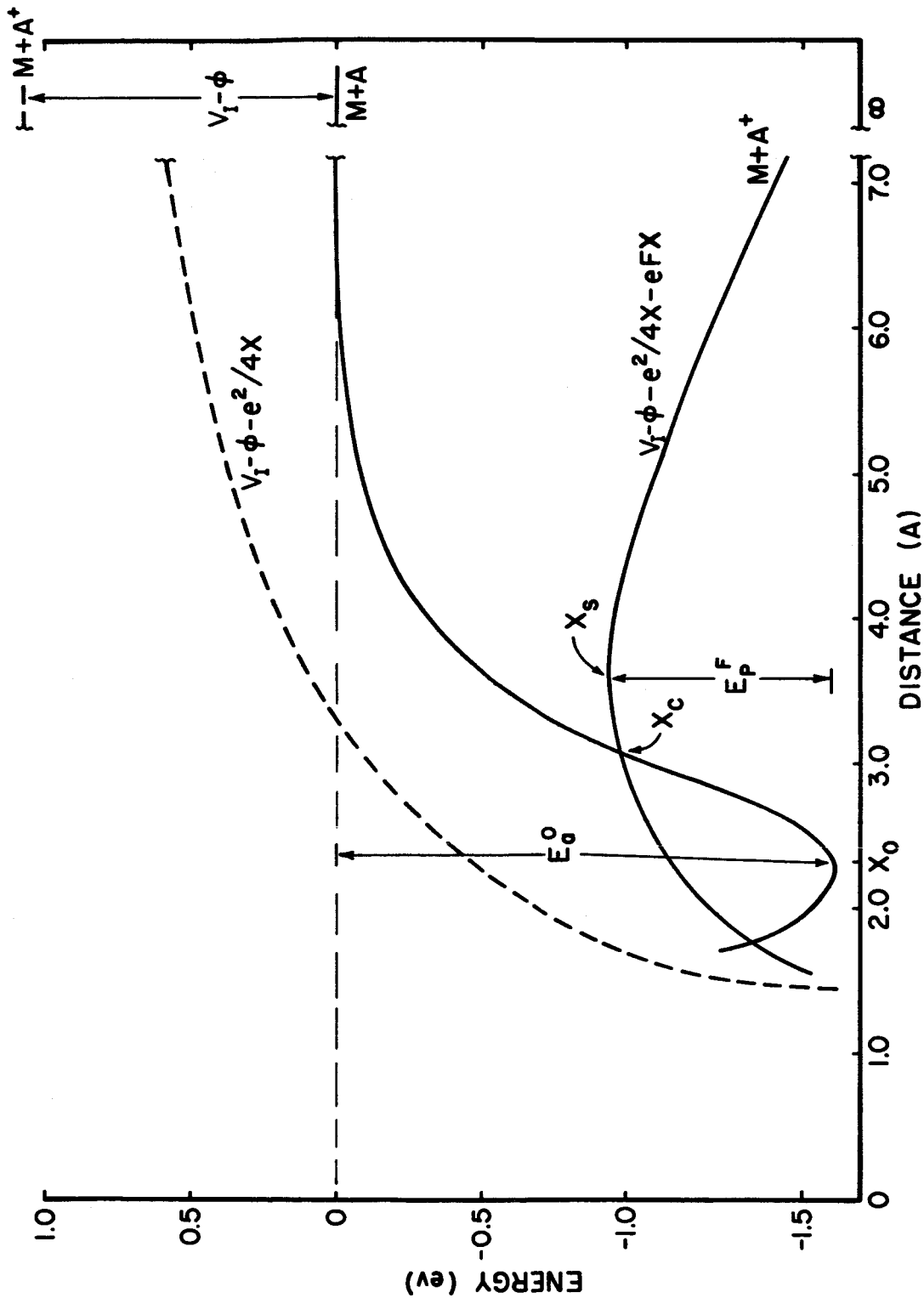
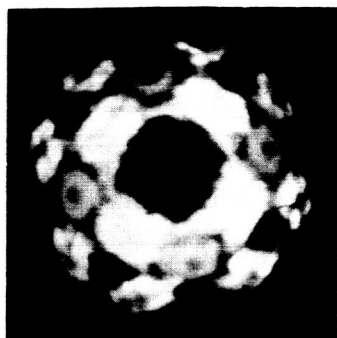
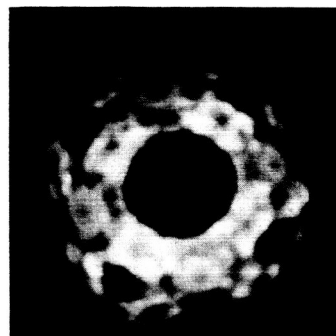


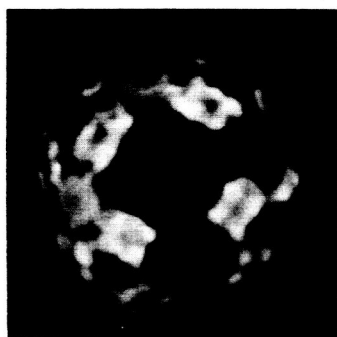
Figure 22. Potential energy diagram for quasi-metallic (i.e., non-ionic) adsorption in the presence of an applied field. The $M+A^+$ curve is an image potential (dashed line) which is altered by the field so as to form a Schottky saddle to the right of the $M+A$ ground state curve. When $V_I - \phi$ is small or negative the ionic curve may be the ground state curve at X_0 and thus lead to ionic adsorption. No polarization effects have been included in the diagram.



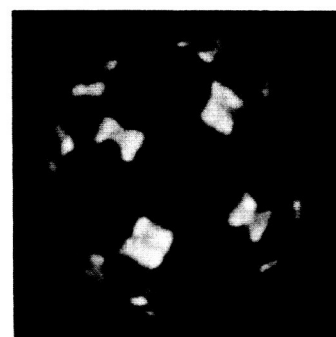
(a)



(b)



(c)



(d)

Figure 23. Progressive pattern changes during field desorption at a cesium coverage of 0.7×10^{14} atoms /cm² ($\phi = 2.70$ eV) on a (100) oriented tungsten substrate at 113° K and desorbing field of 41 Mv/cm. Photo (a) taken at $t = 0$

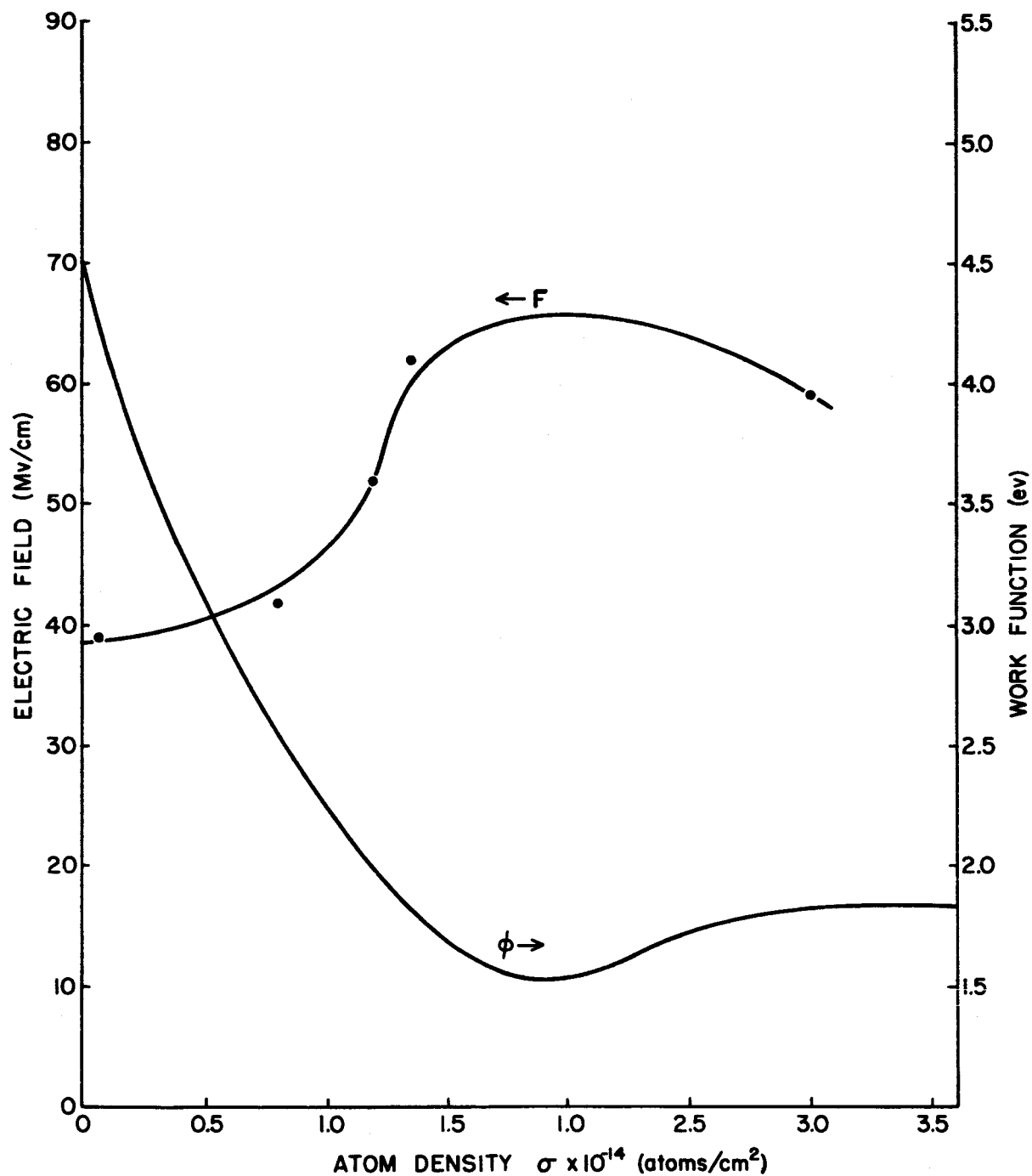
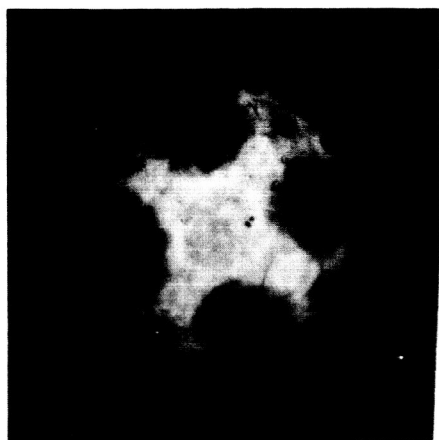


Figure 24. Field F for onset of ionic desorption at approximately 100° K and work function ϕ as functions of cesium coverage.

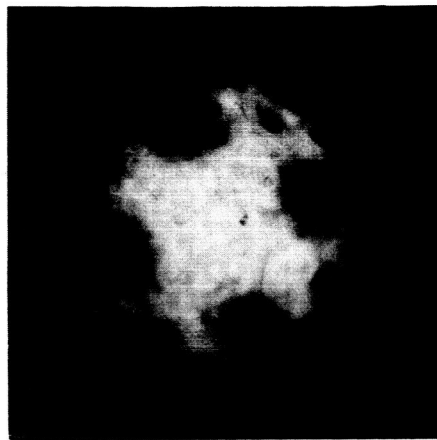
Such measurements were unsuccessful because of a rapid regenerative increase in the field desorption rates causing the coverage to change nearly instantaneously to zero, thus making rate studies extremely difficult and perhaps impossible. This difficulty is probably related to the highly reversed emission distribution and rapid local increase in ϕ with decreasing ϕ throughout this coverage range. Thus, as can be seen in Figure 23(a), measurements of coverage change that rely on variations in pattern or field emission current sample changes occurring first on the emitting $\{110\}$ and $\{112\}$ planes. This can be illustrated by the pattern sequence in Figure 23, which was obtained in the low coverage extreme of the region under consideration and where it was possible to terminate the field desorption process before it proceeded to complete cesium removal. The desorption of cesium from the (100) plane, which occurs first, does so with no perceptible change in total emission current. At somewhat higher coverages the relative emission from the $\{100\}$ and $\{111\}$ regions is too low to give even pattern information, so that considerable undetected field desorption occurs from these regions before the strongly emitting (and hence, low work function) $\{110\}$ and $\{112\}$ planes are suddenly field desorbed to completion.

For cesium coverages in excess of 1.9×10^{14} atoms/cm² (the coverage corresponding to the work function minimum) the rate of field desorption decreases with decreasing coverage due primarily to the reversal in the dependence of ϕ on ϕ , thus making it possible to measure E_p^F as a function of F . Such measurements were carried out in the coverage and work function interval 2.9 to 2.7×10^{14} atoms/cm² and 1.81 to 1.78 eV respectively. This coverage interval brackets the atom density (2.73×10^{14} atoms/cm²) of the (100) plane of bulk cesium and, therefore, should be considered close to monolayer coverage. The field emission patterns corresponding to the initial and final coverages over which the desorption rates were measured are shown in Figure 25 and indicate field desorption to occur primarily from the higher work function $\{110\}$ regions of the emitter in accordance with equation (50) if the anisotropies in ϕ exceed those of E_a^0 .

The results obtained are given in Table VI and show a general decrease in E_p^F with increasing F , although the trend is not monotonic. It is interesting to note that the decrease in $\log \nu$ s with increasing field, noted in previous field desorption studies involving other adsorbates^{28,15}, and also for cesium on tungsten at low coverages²⁹, was not observed in the high coverage results reported here. In order to eliminate the possibility of complicated effects on the pre-exponential factor of equation (51) due to field desorption from a mobile layer^{28,30}, the measurements were confined to a field and temperature range such that field desorption occurred from an effectively immobile layer. It can be concluded from the normal and constant $\log \nu$ s values over the investigated field range that the transition from the ground adsorbed state to the ionic state at x_c (see Figure 22) is rapid and not altered by field.



(a)
Initial point
 $\theta = 1.81 \text{ eV}$



(b)
Final point
 $\theta = 1.78 \text{ eV}$

Figure 25. Patterns and work functions of the initial and final points used in determining the variation of desorption energy with field. Initial and final cesium coverages are 2.9 and 2.7×10^{14} atoms/cm² respectively.

TABLE VI

Variation of E_p^F and $\text{Log } \nu_s$ with F in the Coverage Range
 $\sigma = 2.9 \text{ to } 2.7 \times 10^{14} \text{ atoms/cm}^2$

$E_p^F(\text{ev})$	$\text{Log } \nu_s$	$F(\text{Mv/cm})$	$T(^{\circ}\text{K})$
0.791 ± 0.021	12.68 ± 0.41	---	252-276
0.507 ± 0.014	15.83 ± 0.49	30.9	135-145
0.455 ± 0.016	14.45 ± 0.63	33.9	128-141
0.386 ± 0.018	12.58 ± 0.42	35.9	125-135
0.323 ± 0.021	10.47 ± 0.83	37.9	121-133
0.332 ± 0.015	11.03 ± 0.62	39.9	116-130
0.362 ± 0.013	12.62 ± 0.54	39.9	116-127
0.393 ± 0.031	14.46 ± 0.60	42.9	117-125
0.366 ± 0.013	13.26 ± 0.56	42.9	114-123
0.371 ± 0.013	13.87 ± 0.55	46.2	111-119
0.325 ± 0.011	12.51 ± 0.50	48.9	106-115
0.326 ± 0.014	13.08 ± 0.67	52.9	103-110
0.291 ± 0.021	11.90 ± 1.02	55.9	100-107
0.287 ± 0.021	12.58 ± 1.05	58.9	95-101

Discussion of Results

According to the simplified model depicted in Figure 22 and the considerations leading to equation (50), the position of the Schottky saddle is given by

$$x_s = \frac{1}{2} \left(\frac{e}{F} \right)^{1/2} \quad (52)$$

and is approximately 2.4 Å at the highest field investigated. Since this is less than the atomic radius of cesium, it is unlikely that the expression for

x_s is valid and suggests that more detailed field interactions must be considered. Least squares analysis of the data of Table VI according to equation (50) with the inclusion of a μF and $\frac{1}{2}(a_a - a_i)F^2$ term,

$$E_p^F = E_a^O + V_I - \phi - e^{3/2} F^{1/2} + |\mu| F + \frac{1}{2}(a_a - a_i)F^2 \quad (53)$$

where a_a and a_i are the polarizabilities of the atomic and ionic states, leads to values for μ , $a_a - a_i$, and $E_a^O + V_I - \phi$, which are 1.14×10^{-18} esu, 65 A^3 , and 2.32 eV respectively. The resultant fit of equation (53) to the data is shown in Figure 26; equation (50) is also plotted showing its failure to fit the data. The calculated value for $E_a^O + V_I - \phi$ term based on the measured E_a^O and ϕ values is 2.25 eV ; the μ and a values are reasonable if a polarizable atomic (i.e., quasi-metallic) ground state²² is assumed.

A more comprehensive investigation of the theory of field desorption²² shows that additional F and x dependent terms should be considered; in summary they are: 1) evaluation of ϕ_c rather than ϕ_∞ ; 2) inclusion of a field-induced work function change $\Delta\phi_c^F = 4\pi\sigma_a F$ evaluated at x_c ; 3) derivation of effective fields for the terms involving F ; 4) an additional term correcting for the polarization of the ad-layer by the ion formed at x_c . Inclusion of these corrections in equation (50) leads to the following:

$$E_p^F = E_a^O + V_I - \phi_c + \Delta\phi_c^F + \mu F_o + \frac{a_a}{2} F_o^2 - \frac{a_i}{2} F_s^2 - \frac{e^2}{4x_s} - eF_s x_s - \frac{12.5a_a e^2 x_s^2}{(y^2 + x_s^2)^3}, \quad (54)$$

where y is the lateral distance between ad-atoms and the subscripts o , c , and s refer to distances from the surface noted in Figure 22. The origin and method of calculation of these terms are given in reference 22 where the ad-atom is treated as a polarizable point dipole. Equation (54) was solved for x_s (the position of the Schottky saddle) by assuming $x_c \approx x_s$ and employing the following values for the various constants: $a_a = 50 \text{ A}^3$, $a_i = 3 \text{ A}^3$, $\mu = 2.8 \times 10^{-18} \text{ esu}$ (determined from $\mu = \Delta\phi/4\pi\sigma$), and $x_o = 2.6 \text{ A}$ (bulk atomic radius). The values of x_s consistent with the respective E_p^F and F are given in Figure 26 and yield x_s values considerably larger than those evaluated by equation (52) which decrease with increasing field. Throughout the field range covered, the $\Delta\phi_c^F$ term is the predominate polarization correction due to the large value of a . Inclusion of the polarization and field-dipole interactions yields a value of $x_s = 9.8 \text{ A}$ at the highest field in contrast to the unlikely value of 2.4 A with the omission of such corrections. Thus, it appears appropriate to depict adsorbed cesium (at this coverage) in a polarizable (quasi-metallic) ground state at x_o , with a transition to an ionic state at $x > x_c$ in the presence of a field.

It should be emphasized that picturing an adsorbed metallic layer as discrete particles, so that one may speak of atomistic properties such as

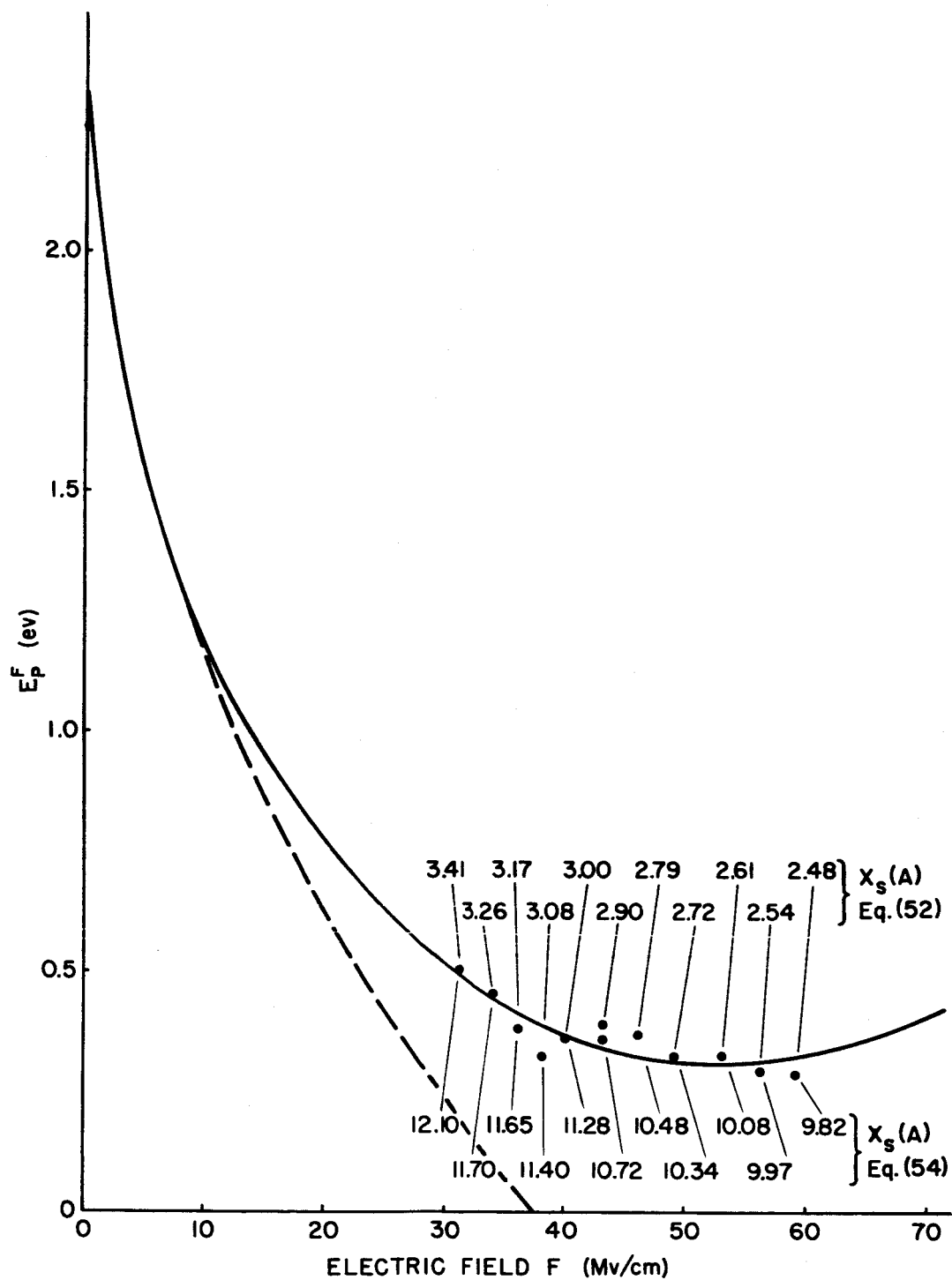


Figure 26. Least squares fit of equation 53 to data of Table VI. Dashed line shows variation of E_F^F according to equation 50. Values of x_s calculated according to equations 52 and 54.

α and μ , is somewhat approximate. This is particularly true at lateral separations approximating bulk value so that overlap of wave functions between ad-atoms becomes appreciable. In such cases the field desorption mechanism must approach that of field evaporation from the bulk adsorbate. Further understanding of the proper value of α to use in equation (54) is also important, since it has been seen that various methods of evaluating it (particularly at high coverages) lead to widely different results.

ELECTRICAL BREAKDOWN STUDIES

The initial studies of the pre-breakdown currents between clean and cesium-covered tungsten electrodes have been essentially completed and preliminary studies of the pre-breakdown currents between molybdenum electrodes have been initiated; the results are reported below. In addition, a preliminary investigation has been made of conditions leading into electrical breakdown.

EXPERIMENTAL PROCEDURES

The experimental tube with tungsten electrodes shown in Figure 27 has been described previously¹. It is a diode consisting of a spherical and a planar electrode with variable spacing. A small field emission microscope attached to the main tube monitors the vacuum conditions inside the tube and gives an indication of the type and degree of contamination on the electrode surfaces. Vacuum conditions within this tube were very good since the change in work function on the surface of the field emitter of less than 1% was observed over a period of several hours. A rough estimate based on this information indicates that the pressure of active gases within the tube was less than 10^{-10} torr.

In order to prevent leakage currents along the glass walls during operation of the tube at elevated cesium pressures, the lower part of the tube was heated to 370°K. An optical microscope was focused in the gap in order to study visible effects, and an oscilloscope was used to monitor fluctuations in current.

The molybdenum electrode tube, similar in design to the tungsten electrode tube has a larger envelope and a different supporting structure for the spherical electrode. There is also a molybdenum cup that is used as a cathode shield to prevent emission from the supporting structure. The electrodes are shown in Figure 28.

CURRENT-VOLTAGE MEASUREMENTS

Stable Pre-Breakdown Currents

Pre-breakdown gap currents between clean and cesium-coated tungsten electrodes were measured during the present and preceding contracts as functions of the following parameters: electrode gap spacings from 1.5 to 10.0 mils, surface work functions from 1.2 to 5.1 ev (depending upon the amount of cesium and/or oxygen on the surface), ultrahigh vacuum (pressures

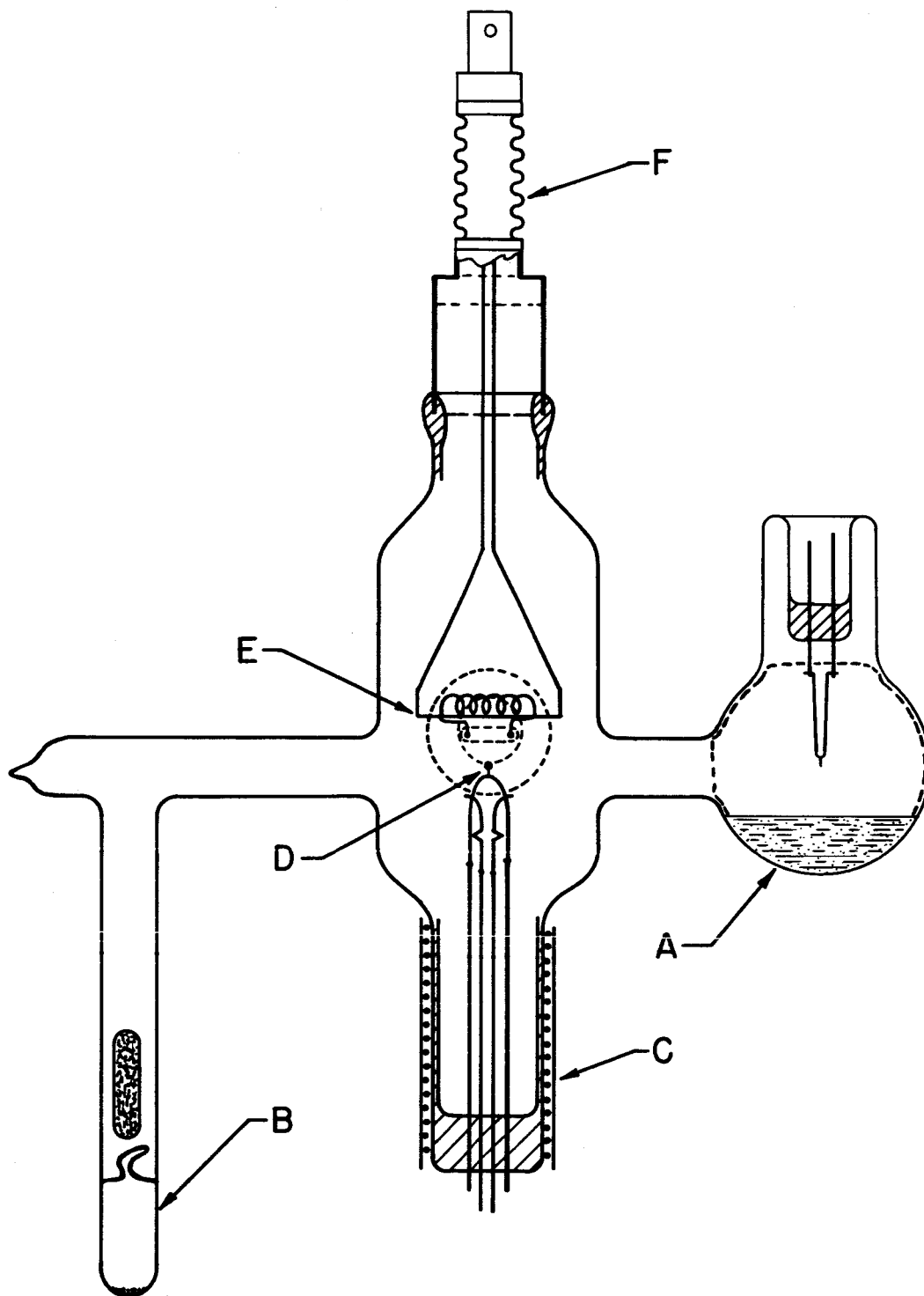


Figure 27. Electrical breakdown study tube with variable spacing electrodes: A, field emission microscope; B, cesium ampule; C, heatable section of in-seal; D, spherical electrode; E, plane electrode; F, stainless steel bellows.

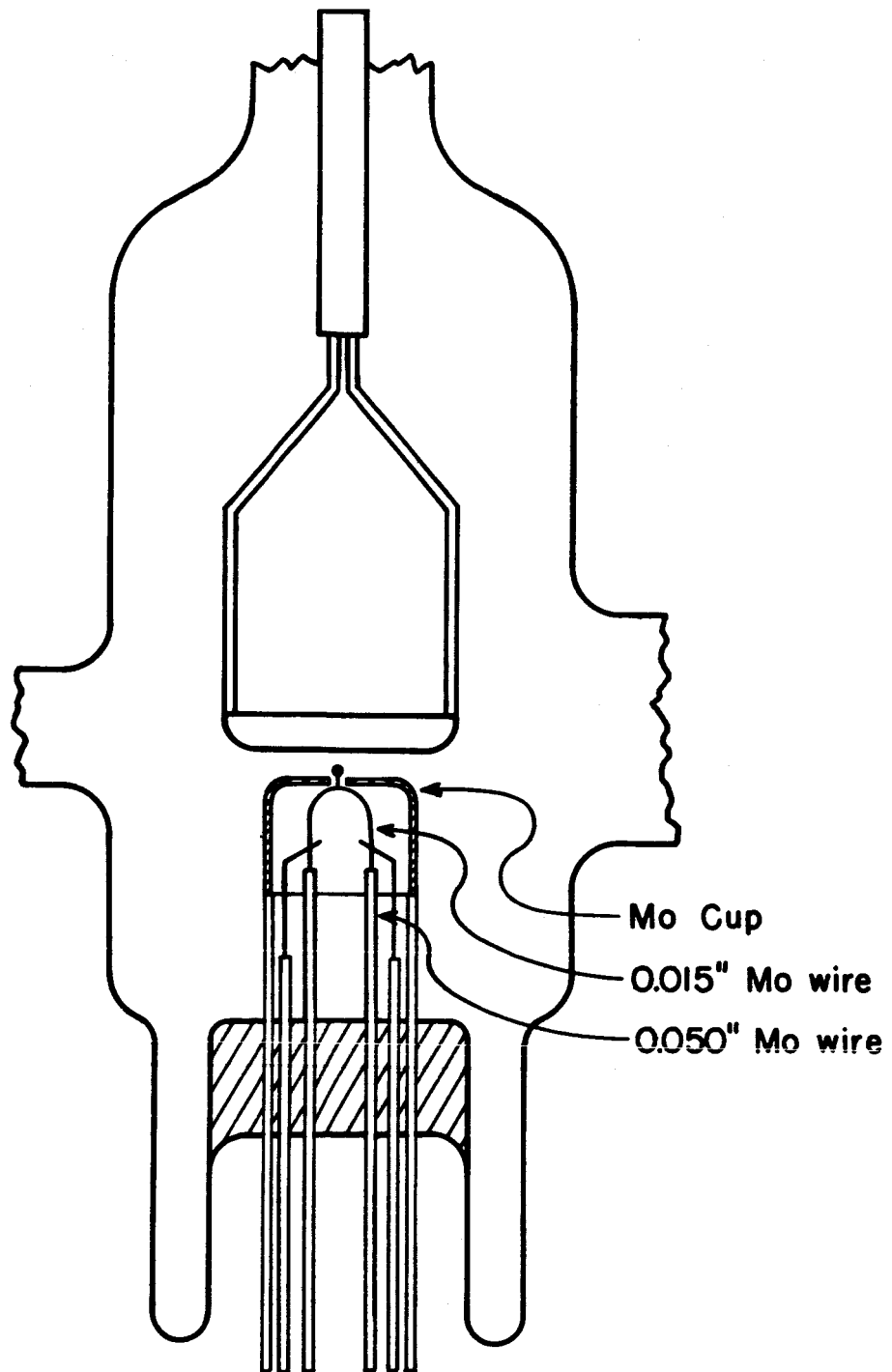


Figure 28. Electrodes in molybdenum electrical breakdown tube showing molybdenum cup used as cathode shield and enlarged envelope. Other parts of the tube are the same as those shown in Figure 27.

less than 10^{-10} torr) and ambient cesium pressures up to 2.0×10^{-6} torr, temperatures of the clean substrate between 293°K and 1000°K, both polarities of electric field, and various degrees of surface roughness. In addition, the pre-breakdown currents between clean molybdenum electrodes were determined under ultrahigh vacuum conditions for electrode gap spacings from 1.0 to 10 mils and for various degrees of surface roughness.

For gap currents between 1.0×10^{-10} and 5.0×10^{-5} amperes, under the conditions mentioned above, the field emission nature of the gap current was proven by the linearity of Fowler-Nordheim plots of the gap current and gap voltage relationship under all conditions investigated. This linearity is illustrated in Figure 29 for a cesium pressure of 2.0×10^{-6} torr at various gap spacings and in Figure 30 for both polarities of field at a given gap spacing; similar plots showing the effects of changing other parameters appear in previous reports^{1, 31}. Adsorption of cesium and/or oxygen affects the pre-breakdown gap current primarily through the changes caused in the work function of the electrode surfaces, as shown in Figure 10. The effect of increasing the cesium vapor pressure within the gap is to increase the cesium coverage on the electrodes for a given temperature; for a cesium vapor pressure of 2.0×10^{-6} torr with electrodes at room temperature the cesium coverage is greater than 1 monolayer. Our data indicate that for gap spacings investigated here, which are very much less than the mean free path of electrons in the cesium gas, the cesium pressure, over the range investigated, affects the pre-breakdown gap currents only through the changes in work function that it causes. At higher cesium pressures, higher gap currents, or long gap spacings, other mechanisms may become important and will be investigated.

In determining degrees of surface roughness, it is expedient to define an enhancement factor γ as the ratio of electric field F at the tip of some protrusion on the surface to the average field F_{av} on the supporting electrode, $\gamma = F/F_{av}$; it is essentially that factor by which surface roughness reduces the maximum voltage which can be sustained by a vacuum gap when field emission or some other field-dependent process is the limiting factor. In these experiments a wide range of values of enhancement factor from 6 to 340 have been measured depending upon the past history of the electrodes.

There are many ways in which surface roughness may be reduced, such as polishing, etching, sputtering, heating; however, each of these methods must be used with extreme care, since under some circumstances they may also cause roughness. For example, it has been shown that for tungsten protrusions with very sharp tips at temperatures below the melting point the primary mechanism causing changes in radii is surface migration^{32, 33}. In the absence of applied stresses surface migration tends to dull the protrusions; however, except by very prolonged heating at extremely high temperatures, it is difficult to obtain radii larger than a few microns by heating only³⁴. This means that a

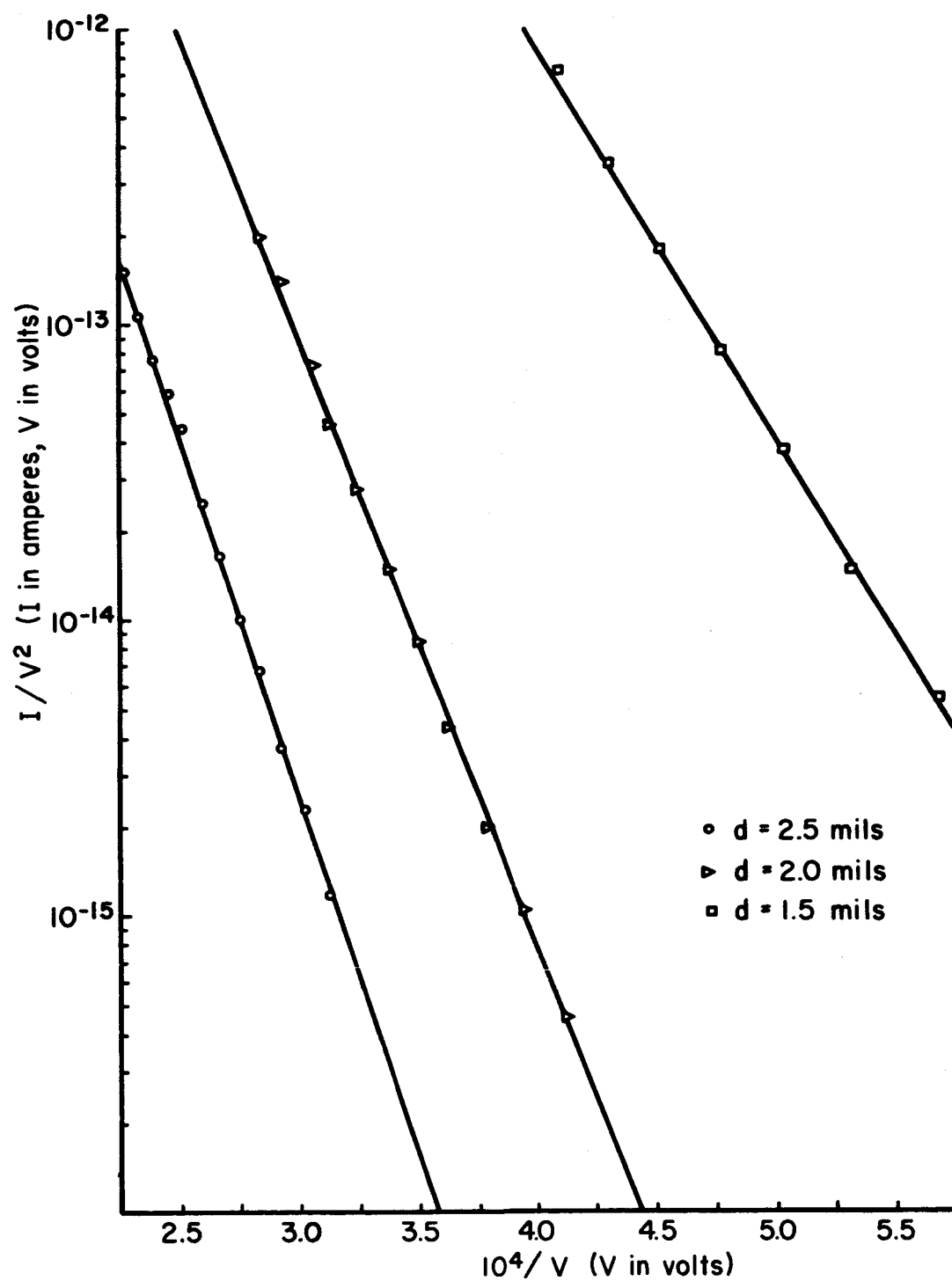


Figure 29. Fowler-Nordheim plots of I-V data obtained at the indicated electrode spacings for an ambient pressure of 2×10^{-6} torr.

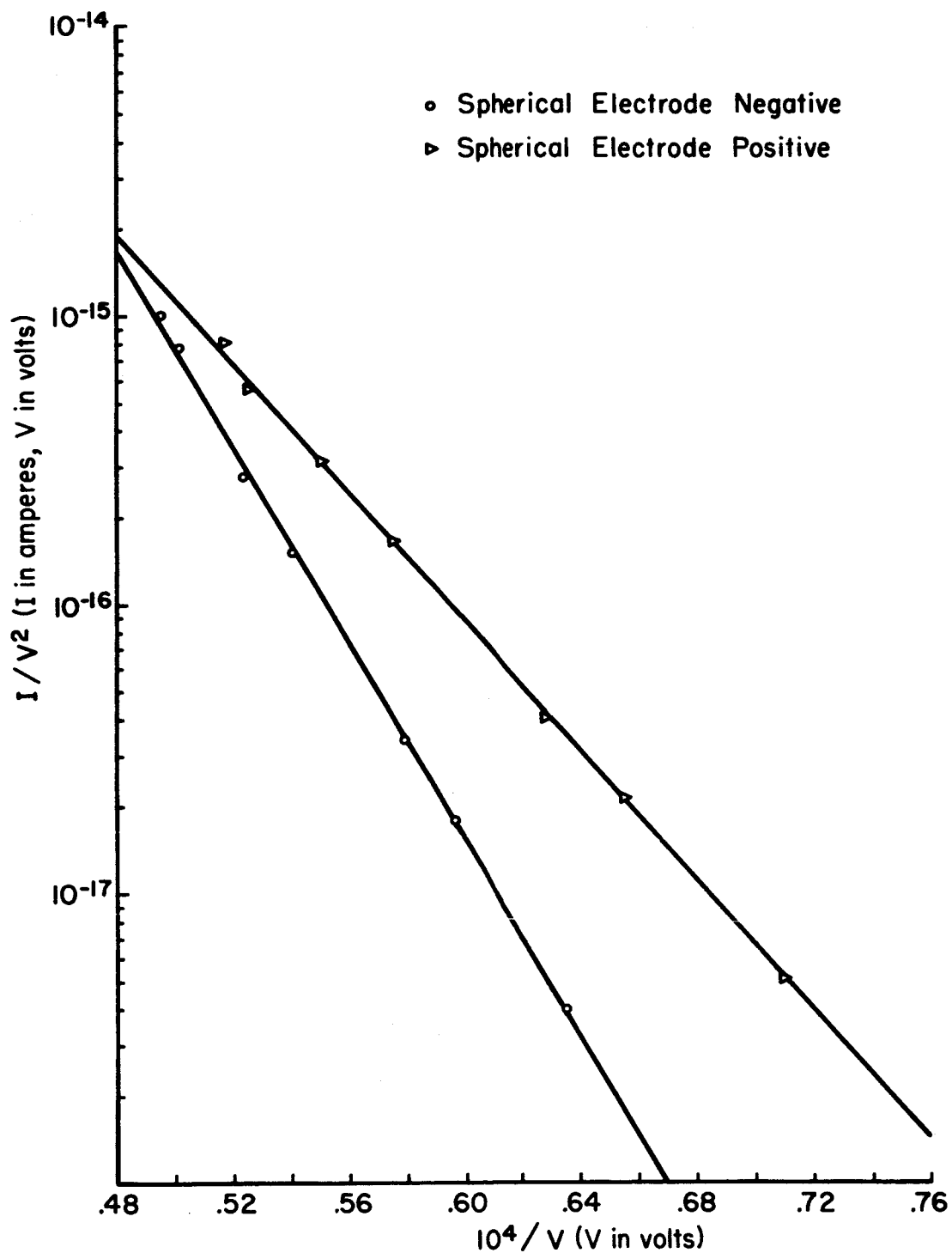


Figure 30. Fowler-Nordheim plots of I-V data for both polarities of field at the same gap spacing.

reduction in the field enhancement factor due to heating will occur if the tungsten protrusions have tip radii less than a micron, but that very little change will occur if the radii are larger than a few microns.

In the tungsten electrode experimental tube, enhancement factors of 100 on the sphere were lowered to the order of 10 by heating the sphere to a temperature close to 3000°K. The importance of the heating temperature can be seen from data taken on both the sphere and the plane electrodes after an arc had occurred, and presented in Table VII. The sphere could be heated to 3000°K, while the plane could be heated only to about 1600°K without causing excessive heating of the tube walls and consequent increase in tube pressure; the sphere had both lower enhancement factors and larger emitting radii. The differences in the shape of the Fowler-Nordheim plots of Figure 30 for the two polarities of field are just due to the differences in enhancement factors on the two electrodes.

An example of how heating can increase the enhancement factor was observed in operation of the molybdenum electrode tube, which had a molybdenum cup shielding the cathode support. (See Figure 28). The cup had been machine polished, then electrolytically etched to insure minimum roughness. In spite of this, very high enhancement factors were measured for emitting protrusions on the Mo cup. It has been found in very recent work performed at this laboratory³⁵ that surfaces which have been machine polished, then etched until they are microscopically smooth, will roughen when they are heated in vacuum. The apparent cause of the roughness is the relief of stress introduced during the cold working of the metal. A technique that virtually eliminates this roughness is to machine polish, heat the electrode in vacuum to relieve the stresses introduced during the cold working, then remove the resulting roughness by electrochemical means. This technique will be used to reduce surface roughness in future experimental tubes. In the present experiments, elimination of emission from the Mo cup was achieved by decreasing the cathode sphere to anode spacing and by increasing the sphere enhancement factor. It is interesting to note that even with extremely high enhancement factors only stable field emission pre-breakdown currents were measured.

TABLE VII
Geometry Changes Due to Heating

Electrode	γ	Emitting Area (cm ²)	Apex Radius (cm)
Sphere after arc	25.0	1.5×10^{-11}	2.2×10^{-6}
Sphere heated to 3000°K for 10 sec.	11.0	2.2×10^{-9}	2.7×10^{-5}
Plane after arc	20.0	3.65×10^{-12}	1.1×10^{-6}
Plane heated to 1400°K for 180 sec.	16.3	5.4×10^{-12}	1.3×10^{-6}

Unstable Pre-Breakdown Currents

When the initial gap current was increased above some critical value, instabilities were observed in the form of an increase in current for a constant applied voltage under all conditions investigated; these instabilities were found to be related to changes in the geometry. In many cases, reducing the voltage caused the gap to recover slowly to reproduce its initial Fowler-Nordheim behavior. If a large resistor (50 to 1000 M Ω) was placed in series with the high voltage power supply, the current, which could be monitored with an oscilloscope in parallel with the current meter, was found to oscillate with a frequency determined primarily by the geometry of the tube and an amplitude dependent upon the dc current level. The initiating current level for these oscillations was somewhat dependent upon cesium coverage, although their frequency was independent of cesium coverage.

In the tungsten electrode experimental tube a mechanical oscillation of the spherical electrode and its supporting structure was detected visually, simultaneously with the current oscillation. To eliminate this mechanical oscillation, the supporting structure for the spherical electrode in the molybdenum electrode tube was shortened and redesigned for maximum stability. In addition, a shield was built to keep electrons from the walls in the lower part of the tube. Although the structure was thought to be stable, similar oscillations, but of a higher frequency, were detected when the current reached some critical value. An optical microscope focused on the gap revealed that the large planar electrode which was presumably well supported was moving vertically, causing a variation in gap spacing.

Since field emission current is an exponential function of the applied field, a slight change in gap spacing causes a relatively large change in emission current. Investigation revealed that there was no symmetrical oscillation, but merely a random instability in the current when the series resistor was less than several megohms, the value depending upon the electrode stability within the tube. It seems most likely that the oscillatory motion was connected with the changing voltage drop across the resistor associated with the current change, such as follows: As the electrode began to move towards gap closure the field at the tip of an emitting protrusion was increased, causing an increase in the current across the resistor sufficient to cause an ohmic drop in voltage which, in turn, lowered the field enough to allow the electrode to return to its initial position. When this happened, the current dropped and the voltage increased enough for the procedure to repeat, thus leading to an oscillatory motion. With smaller values of resistance the voltage drop was insufficient to allow the electrode to relax and the electrode continued to move towards gap closure until an arc occurred.

Although it had previously been assumed¹ that the magnitude of the force due to the electrostatic stress between the sphere and the plane were too small to account for the apparent changes in β , it can be shown (see

Appendix I) that for a slightly non-symmetrical alignment of the spherical electrode and its support, the force in the direction parallel to the plane is large enough to account for the movement of the spherical electrode in the tungsten experimental tube. In the molybdenum experimental tube, the additional electrostatic stress between the planar cathode shield and the planar electrode is shown to be of sufficient magnitude to account for movement of the larger electrode (see Appendix II).

It is interesting to note the size and apparent stability of the electrodes in the molybdenum experimental tube (Figure 28). In order to calculate the magnitude of the force necessary to move the planar electrode, weights were attached and a spring constant of 41 gm/mil was determined for the structure. As the voltage is increased for a given value of gap spacing, some critical amount of movement, roughly a few percent of the initial gap spacing, will occur so that as the gap decreases, the stress will increase and lead to a regenerative process. At the very narrow gap spacings, even a few percent change in spacing would be optically undetectable although the resulting increase in current of twenty to fifty percent could be shown to be related to a geometrical change in tube geometry. Caution should therefore be exercised when determining whether the geometrical changes indicated by the current-voltage relationships are due to localized geometrical changes in emitting protrusions or whether they are actually due to geometrical changes of the gross surfaces. Further study to isolate each of these effects seems to be indicated.

Maximum Currents Preceding Electrical Breakdown

Despite the difficulty with electrode stability mentioned in the preceding section, it was possible to measure the stable current-voltage characteristics between clean molybdenum electrodes under certain conditions to within an order of magnitude in current of the current level at which an arc occurred. The maximum current before an arc could also be measured, even though at constant voltage the electrode was moving, and the field at the tips of emitting protrusions was increasing. The results indicate that the breakdown is a cathode-initiated process, the result of resistive heating of the tip of an emitting protrusion, as described by Dyke et al.^{36,37}.

If the emitting protrusion is in the shape of a cone, it can be shown that the temperature of the cone will increase as the current density becomes quite high, until the tip is heated to its melting point. This maximum current density can be calculated for a cone of known geometry and, for a temperature of 3000°K, is approximately

$$J_{\max} \cong 170 \frac{a_c}{r} \quad , \quad (55)$$

where a_c is the interior half-angle of the emitter cone measured in degrees, and r is the emitter radius in cm. At the gap spacings investigated, a good

approximation of the geometry of an emitting protrusion can be obtained from the values of the enhancement factor, γ , which is related to the field at an emitting tip in the following way,

$$F = \gamma V/d . \quad (56)$$

It has been reported earlier¹ that a value of the enhancement due to a spheroidal boss on one of two parallel planes can be derived from the resulting potential field and expressed as a function of h/r where h is the height of the protrusion and r is the apex radius. It was also pointed out that the field enhancement factor is dependent on the shape of the boss, not on its absolute size. A value of r can be found by calculating the effective emitting area from the relationship $JS = I$ where S is the effective emitting area of the protrusion tip. Knowing the value of r and of h/r , a value of the half-width of the base of the protrusion H can be determined. If the enhancement factor is high (for example greater than 100) an approximation to the value of the cone angle can be determined by assuming that the shape of the protrusion is almost conical with an interior half-angle $\alpha_c = \cot^{-1}(h/H)$.

Using the above approximations the maximum current density measured under reasonably stable current conditions for a surface whose enhancement factor was calculated to be 140 was found to be $J = 1.09 \times 10^7$ amps/cm² at an enhanced field of 6.9×10^7 volts/cm. For this emitter a value of J_{\max} was calculated and found to be 3.2×10^7 amps/cm, which corresponds to a maximum current of 6.5×10^{-4} amps, a value very close to the final value of current recorded before an arc occurred. Similar calculations for surfaces with enhancement factors as high as 235 offer corroborative evidence that the breakdown between clean electrodes can be attributed to a cathode-initiated process.

TRANSITION RADIATION

Visible radiation from both clean and cesium-coated electrodes has been observed. In each case a small spot of blue light was observed on the anode when the anode current density reached a critical value of about 0.1 ma/cm². As the current was increased by increasing the gross field, the intensity of the radiation increased. Since other workers in the electrical breakdown field have reported similar radiation^{38,39}, a brief investigation of the properties of this radiation was made. The radiation was found to have the following properties: (1) it is plane-polarized in the plane containing the normal to the surface being bombarded and the direction of observation; (2) it has a continuous spectrum; (3) its intensity is very low except for the shorter wavelengths, being noticeably most intense for blue light; (4) its intensity increases with increasing electron energy and current; (5) its intensity is independent of the temperature of the electrode surfaces, the pressure within the tube, up to 2.0×10^{-6} torr, and the degree of contamination of the anode surface. These features are characteristic of transition radiation, as shown experimentally by Boersch et al⁴⁰, and are not

associated with either bremsstrahlung or radiation from surface ionization or heating processes, as had been suggested by others³⁸.

Transition radiation, described initially by Lilienfeld⁴¹ in 1919, has been treated theoretically in several ways. The classical approach of Frank and Ginsburg⁴², and others⁴³, shows that radiation will occur when a moving charged particle, such as an electron, traverses a boundary between two media of different optical properties, in particular a vacuum-to-metal boundary. According to one treatment⁴³ the emission of radiation is due to a changing dipole field formed by the moving point charge and its images in the two media. Using physical arguments, Ferrell⁴⁴ has described a very similar phenomenon which he calls plasma radiation; it is photon emission due to the decay of the conduction electron plasma which has been excited by fast electron impact. These two theoretical interpretations have been generalized by Ritchie and Eldridge⁴⁵, and others⁴⁶, and are found to be similar in many respects. The important result of Ferrell's work is the prediction of a peak in the radiation intensity near the plasma frequency of the particular metal. This result has been confirmed experimentally for a number of metals⁴⁷⁻⁵⁰.

Under the conditions investigated here transition radiation does not contribute to electrical breakdown, since it is first seen at current levels well below the unstable current region and where the current is stable, reproducible, and due to field emission only. Further evidence of this was found in an experimental tube containing a comb of thirty closely spaced field emitters bombarding a molybdenum plate from a distance of about one centimeter. It was found that blue radiation became visible on the anode when the current reached 10^{-6} amperes, and was still visible at 5×10^{-3} amperes when the whole anode had turned dull red ($T = 1320^\circ\text{K}$) due to bombardment heating. The linearity of a Fowler-Nordheim plot of the current-voltage data over this current range is shown in Figure 31, indicating field emission is the only electron emission process involved and that no significant ion currents were present. The reproducibility of the I-V data tends to nullify the existence of ion currents or changes in geometry due to excessive electrode heating.

Comparison of experimental results with theory offer corroborative evidence that the emission of radiation is not a factor contributing to voltage breakdown. For a metal foil whose thickness is infinite compared to the wavelength of the emitted radiation, Ritchie and Eldridge⁴⁵ express the number of photons emitted per unit solid angle in the direction from the foil normal specified by the angle δ , per unit frequency interval at the angular frequency ω , per incident electron for the non-relativistic case as:

$$n(\delta, \omega) = \frac{Z^2 a_f \beta_r^2 \sin^2 \delta (1 - \beta_r^2)}{\pi^2 \omega} |C|^2 \quad (57)$$

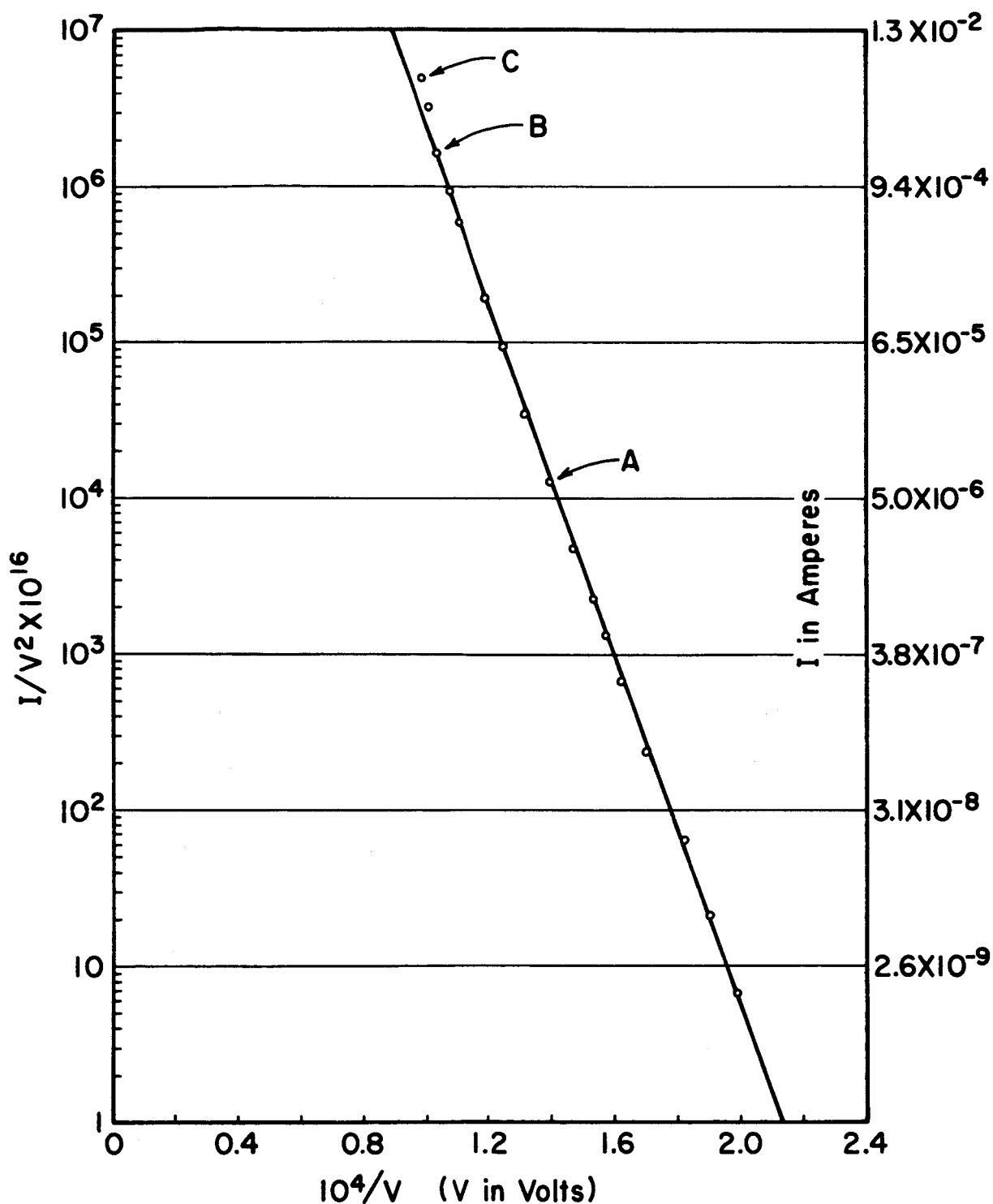


Figure 31. Fowler - Nordheim plot of current - voltage data from clean tungsten electrodes. A represents point where transition radiation has increased in intensity, while the anode has reached a temperature of 970°K . At C the radiation is still visible against an incandescent background (1320°K).

where

$$\Omega = \cos \delta,$$

$$\beta_r = v/c \text{ with } v \text{ being the electron velocity,}$$

$$|C|^2 = \left| \frac{\epsilon - 1}{\mu\epsilon + (\epsilon - 1 + \mu^2)^{1/2}} \right|^2,$$

$$\epsilon(\omega) = \text{complex dielectric constant,}$$

$$Z = \text{atomic number,}$$

and

$$a_f = \text{fine structure constant.}$$

This expression shows that the radiation is plane polarized in the plane containing the foil normal and the direction of propagation of the photon. To get a qualitative feeling for the physical meaning of this equation we separate the dielectric constant into real and imaginary components $\epsilon = \epsilon_1 + i\epsilon_2$ and consider limiting cases. If $\epsilon_1 = 1 - (\omega_p/\omega)^2$ corresponding to the case of the free electron gas, where ω_p is the plasma angular frequency, and $\epsilon_2 \ll 1$ there should be a maximum in the photon intensity distribution at the frequency $\omega = \omega_p/\Omega$ with a fairly rapid decrease in intensity on either side of this value. At $\omega = \omega_p$ an ideal metal changes from a totally reflecting to a totally transmitting medium. If $\omega > \omega_p$ the phase velocity of the photons within the medium is greater than the velocity of light within the medium, and photons leaving the surface will be deflected toward the surface normal. This indicates that there will be certain angles at which no photons will be observed. If $\omega < \omega_p$ photons are absorbed in the medium and only a relatively small emission can occur. One would expect that there would be a maximum in photon intensity at or near the plasma frequency, with a rather rapid decrease in intensity for wavelengths either greater or less than this value. This has been found to be true experimentally for silver foils^{47,49}, which show a very high intensity near 3300 Å (corresponding to the calculated plasma frequency). Similar behavior was found for magnesium⁵⁰ and aluminum⁴⁷ at their respective plasma frequencies.

Since the radiation observed in our experiments can be described by equation (57) the maximum number of photons that could be expected to be emitted can be calculated. Assuming the worst possible case, that all of the photons strike the cathode, a value can be obtained for the maximum photocurrent due to this radiation. Unfortunately, values for the optical constants for tungsten in the short wavelengths ($\lambda_p \approx 1300$ Å) have not been found. However, recent results for the optical constants of the similar metal molybdenum have been obtained in the ultraviolet down to 2480 Å by Waldron and Juenker⁵¹ who showed that, for the ultraviolet wavelengths, the optical constants of molybdenum were compatible with a free electron model for the metal. Using the values for the optical constants from the data of Waldron and Juenker, it was found that the value of $|C|^2$ in equation (57) increases as λ decreases or, conversely

$|C|^2$ decreases as ω decreases. Thus it appears that the number of emitted photons probably increases as λ approaches λ_p .

Very rough approximations of the maximum number of photons/electron were calculated using the theoretically determined value of the plasma wavelength for molybdenum and extrapolating the optical data of Waldron and Juenker⁵². A numerical value of 1.12×10^{-4} photons/electron was calculated for incident electrons of energy 20 kv integrating over all possible angles of emission. Letting all the photons strike the cathode, a value for the photocurrent can be found using recent results on measurements of photocurrent from plane-polarized radiation incident on clean molybdenum⁵². A maximum photoelectric yield of 1.0×10^{-3} electrons/photon was calculated for photons at the plasma frequency. The maximum photocurrent possible using the above approximations is 1.12×10^{-13} amperes when the current in the gap is 1.0×10^{-6} amperes. Since only metals having loosely bound valence electrons and tightly bound cores follow the free electron theory, the real number of photons would be far less than the calculated number. On the basis of these calculations, it seems very unlikely that there is any enhancement of the current due to the existence of the observed radiation. The conclusion of this investigation, based on results of both experimental and theoretical evidence, is that emission of transition radiation is not directly associated with the voltage breakdown process.

PROTRUSION GROWTH STUDIES

Several investigators have reported observing changes in geometry of electrodes in the presence of high fields and elevated electrode temperatures. Little and Whitney⁵³ show electron microscope shadowgraphs of whisker-like projections which were found on copper, stainless steel, and aluminum cathodes. Tomaschke⁵⁴ found similar projections on clean tungsten electrodes after operating for a period of fifteen minutes under conditions where the field emission current had become unstable (the actual field at which he noted instabilities is roughly the same as that at which instabilities were found to occur in our study), while no such projections could be found on electrodes that had only operated under stable field emission current conditions.

Since it has been shown previously¹ that instabilities in the I-V characteristics could be related to a change in the geometrical β factor, a cursory investigation has been made in an attempt to establish the conditions under which changes in the micro-geometry of electrode surfaces might occur. The experimental tube used was a simple field emission microscope in which the tip could be heated in the presence of both positive and negative fields. The procedure for positive fields was to apply field and temperature for very short time intervals, then reverse the field and observe changes in the room temperature field emission pattern. It was found that the pattern sequence initially

followed that observed in an earlier study⁵⁵, in which certain crystallographic planes were found to build up, causing the initially smoothly rounded field emission tip to assume a polyhedral form, until the field at the tip reached about 10^8 v/cm. When a positive field of this magnitude was applied while the tip was heated above 1000°K , small projections, which appear as small bright spots in the field emission pattern, were "nucleated" initially in the $\{100\}$ crystallographic regions. With increase in time at a constant temperature and applied voltage, spots appeared in the $\{111\}$ regions, reaching an equilibrium condition after sufficient time in which the entire tip was covered with spots except for the centers of the $\{110\}$ planes (see Figure 32.). The time required for the tip to come to this equilibrium condition with a positive applied field decreases rapidly as either the temperature or the field is increased.

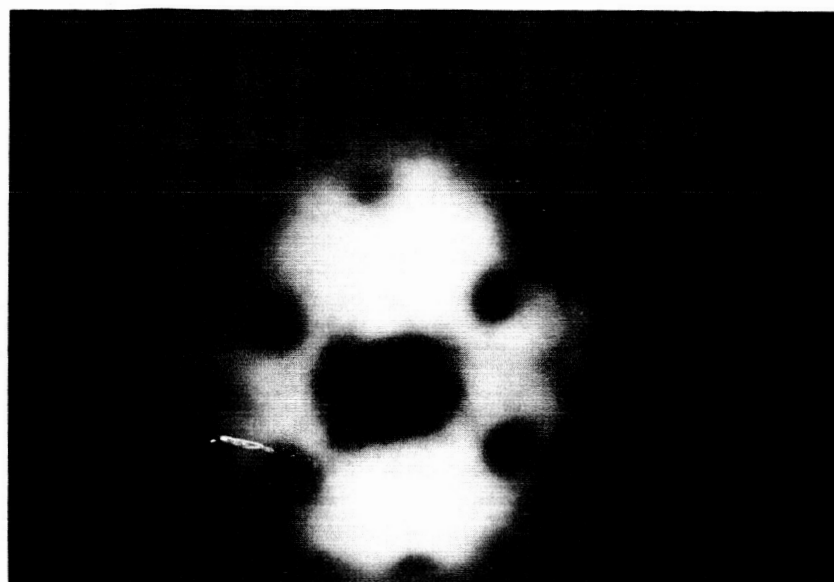
Nucleation of projections was accomplished with positive field; nucleation with negative fields was not possible because excessive field emission at negative fields of 10^8 v/cm cause an arc and gross geometrical changes. However, when a projection had been formed by application of a positive field, it could be caused to grow in the presence of negative fields of approximately 4.5×10^7 v/cm and, in some cases, even at room temperature.

It has been known for some time that surface migration causes changes in surface geometry³³. An expression for the change in protrusion length dx/dt due to surface migration has been derived and confirmed experimentally for several refractory metals³²; it is approximately

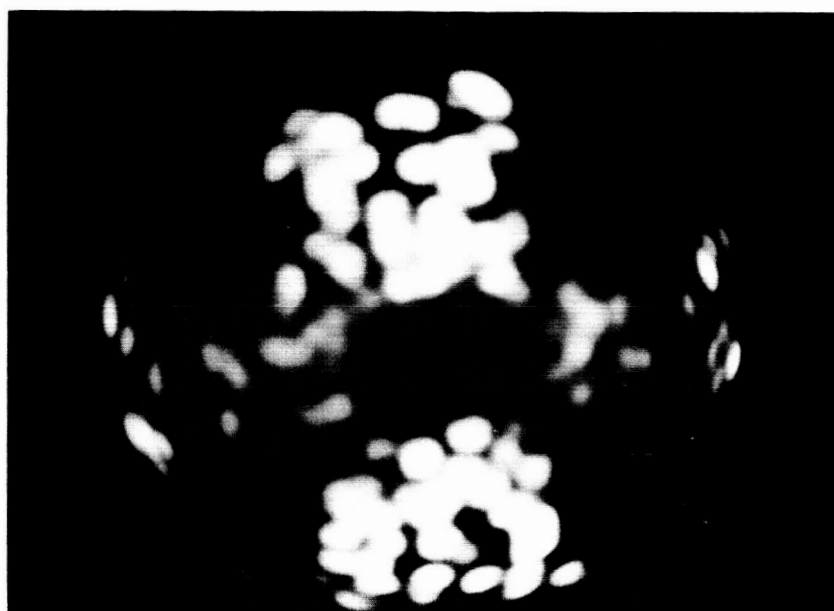
$$dx/dt = -1.25 \frac{S_t \Omega_o^2}{r^3 A_o} \frac{D_o e^{-E_d^F/kT}}{1 - \frac{rF^2}{8\pi S_t}} \quad (58)$$

where Ω_o and A_o are the atomic volume and surface atom density, respectively, D_o and E_d^F are the diffusivity constant and activation energy for surface migration, S_t is the surface tension of the protrusion material, r the radius of the protrusion tip, T the temperature, F the applied field, and k is Boltzmann's constant. When the field is zero, surface tension forces predominate and the protrusion's length decreases. Application of an electric field affects migration in two ways: (1) if the field is high enough, the resulting electrostatic stress reverses the direction of migration so that the protrusion tends to lengthen; and (2) the field reduces the activation energy E_d^F so that the migration rate increases⁵⁵. This suggests a mechanism that could lead to cathode-initiated electrical breakdown: at a critical field, depending upon the protrusion radius, the protrusion begins to lengthen due to surface migration of material toward the protrusion tip; this in turn increases the field, and also the emitted current, for a constant voltage. This process would be regenerative and would quickly lead to an arc by resistive heating.

It should be pointed out that the actual nucleation of protrusions on a clean cathode surface at room temperature by field alone has not been



A



B

Figure 32. Field emission patterns indicating the growth of protrusions: (A), initial pattern, $I = 10\mu\text{a}$, $V = 10\text{kv}$; (B), pattern after heating at 1600°K for 20 minutes with a positive field of 140 Mv/cm at the emitter surface, $I = 10\mu\text{a}$, $V = 3.4\text{ kv}$.

clearly established by our results, although nucleation by sputtering may be possible on contaminated surfaces as suggested by other work⁵⁴. On the other hand, it is interesting to note that our results suggest protrusion growth by field and temperature alone is possible on both anode and cathode surfaces, in accordance with the observations of others⁵⁴. In view of the proposed field-induced surface migration growth mechanism, it is conceivable that such a mechanism may occur at even lower fields and temperatures for cathodes of lower melting metals (e.g., copper, iron, etc.) and lead to large field enhancement factors and, hence, field emission currents at moderate gross field gradients.

SPUTTERING STUDIES BY FIELD ION MICROSCOPY

INTRODUCTION

Physical sputtering has attracted increasing interest in the last few years primarily for two reasons: (1) only recently have enough consistent and reliable data been collected to permit some insight into the mechanisms governing sputtering; and (2) questions and problems involving sputtering have arisen in a number of technical areas being emphasized at the present time. Among these latter are: (a) space physics, in which sputtering plays a role in such problems as the erosion of electrodes in electric propulsion devices, erosion of rocket nozzles, ion bombardment of missiles and satellites in the space environment, and the state of the surface of the moon; (b) thin film physics in which sputtering is often used in the formation of thin films for electric components and circuits; (c) high energy physics, in which sputtering is one of the mechanisms by which high energy bombardment causes radiation damage in solids; (d) plasma physics, in which sputtering is involved in the interaction of a plasma with the walls of its container; (e) surface physics, in which sputtering may be used to clean and smooth a surface or to roughen and contaminate it.

Despite much recent progress towards understanding the basic mechanisms involved in sputtering, there are many questions which remain to be answered⁵⁶. The questions which field ion microscopy may be helpful in answering are those related to individual sputtering events and to damage in refractory metal single crystals, because of the ability of the field ion microscope to resolve individual atoms in some cases.

Review

The type of sputtering being considered here is physical sputtering⁵⁷, which may be considered a special form of radiation damage. Neglected here is chemical (reactive) sputtering⁵⁸, which is confined to certain reactive ion and target material combinations and arises from the formation of volatile compounds on the surface. Physical sputtering, on the other hand, can result whenever ions or atoms of any element bombard a surface of any material with sufficient kinetic energy; target material is "evaporated", i. e., removed from the target, by the impact of the bombarding particles.

The development of an adequate theory of sputtering has been slow; there is still no quantitative theory which can explain in detail all experimental observations^{56, 57, 59}. However, there have been two basically different theoretical models that have been proposed to explain sputtering: (1) The first is based upon vaporization; according to this model the

impinging particle heats the target locally and evaporates target material from the created hot spot.⁶⁰ Thus the sputtering ratio, the number of ejected particles per impinging particle, should depend upon the energy of the incident particle, the binding energy of the target particles, and the temperature of the target, but not upon the mass ratio of the impinging and target particles, nor particularly upon the angle at which the impinging particle strikes the surface, nor upon the crystalline structure of the target; neither should the ejected particles have a preferred direction of emission. (2) The second model is based upon momentum transfer; according to this model the impinging particle undergoes an elastic collision with a target particle, transferring both energy and momentum to it.^{56,61} Particles may be ejected by the initial impact or by subsequent collisions between displaced atoms within the crystal lattice. The sputtering ratio for this model should depend not only upon the energy of the impinging particle but also upon the ratio of the masses of the impinging and target particles, upon the crystalline structure and orientation of the target, and upon the angle of incidence of the impinging beam.

Most experimental results support the momentum transfer model; some of the principal results are the following: (1) The sputtering ratio is found to depend upon the mass ratio of the impinging particle to the target particle⁶². (2) The target particles are ejected preferentially in the nearest neighbor directions of the lattice ($[110]$ directions in fcc crystals and $[111]$ directions in bcc crystals)^{57,63,64}. (3) At low primary energies atoms are ejected in the directions which involve least momentum change (i.e., to the sides for normal incidence and in a forward direction for oblique incidence of impinging particles)⁵⁷. (4) Target temperature has only a slight effect upon sputtering yield^{57,65}. (5) Average energies of ejected particles are of the order of 10 to 100 ev, much higher than for thermally evaporated particles^{57,64}.

Although many of the experimental results can be explained on the basis of classical transfer of momentum between hard spheres, others require more sophisticated theoretical treatment⁵⁶. Modification of the theory must be made in accordance with the energy of the impinging particle⁵⁶: (1) At low energies the hard sphere collision model applies. (2) At intermediate energies some penetration of the electron clouds surrounding the nuclei of the interacting particles occurs and the Bohr collision model must be used⁶⁶. (3) At higher energies the interactions are essentially Coulombic repulsions between nuclei, as originally investigated by Rutherford. In all energy ranges consideration must be given to the influence of the crystalline nature of the target upon the distribution of energy and momentum among the target atoms, in order to explain both preferential target particle ejection and the distances over which the interaction may take place^{67,68}; also the depth of bombarding particle penetration is a function of crystal orientation⁶⁹.

Many features of the sputtering process are not yet well understood^{56,57,59}. Conditions at the target surface are in general undetermined; this is probably one reason for the disparity among results from different authors and accounts for the difficulty of arriving at consistent sputtering threshold energies⁵⁶. The effect of sputtering upon the crystalline structure of the target is not well-known; there is evidence

that for some materials sputtering actually changes the crystal structure of the first few atom layers to a form different from the bulk structure⁷⁰. Although sputtering is thought to occur in the first few atom layers, it is known that both energy and the bombarding particles themselves may end up at depths of several hundred atom layers^{68, 69}; damage to the interior of crystals due to bombardment by energetic particles should be explored further. Consideration of these and many other problems, such as the energy distribution of the ejected particles, participation of trapped gas atoms in the sputtering process, etc., is necessary before all the essentials of sputtering are understood.

Application of Field Ion Microscopy to Sputtering Studies

Some of the problems mentioned in the previous paragraph may be investigated by field ion microscopy. The field ion microscope, first conceived by Muller⁷¹, is a device of great interest and importance in the study of metal surfaces, because of its ability to resolve individual atoms in a crystalline lattice. For its theory of operation and a fairly complete summary of the experimental results, the reader is referred to a review article⁷² by Müller. Only a brief discussion of its operation will be given here.

The field ion microscope (FIM) is a diode, like the field emission microscope (FEM), but with the voltages reversed. Ions instead of electrons are used to form the image. In order to have a supply of ions, gas is introduced into the tube; the gas molecules are attracted to the neighborhood of the tip by their dipole interaction with the inhomogeneous electric field. In the high field near the tip the molecules become ionized, producing ions that travel to the phosphor screen and form an image of the surface of the point anode. Although the magnification of the field ion microscope is about the same as that of the FEM, the resolution is much greater because diffraction effects are less for ions than for electrons, and at the temperatures employed the velocity components tangent to the surface of the point anode are less for ions. The resolution of the FIM is optimized by operation at low temperature, to reduce the transverse velocity components of the image-forming ions, and by the use of helium gas as the source of ions, since helium has the highest ionization potential of any gas and thus its ions are formed closer to the anode surface. By⁷² these means resolution of neighboring atoms 3 Å apart has been attained.

The FIM anode tip can be kept free of contaminants from the gas phase, if helium is used as the imaging gas, by maintaining a field of 300 Mv/cm or higher on its surface⁷³; since all other gases have ionization potentials less than that of helium, gas molecules other than helium will be ionized at a distance and will never reach the tip surface. At still higher fields (500 Mv/cm for tungsten) atom layers of the tip

material are removed from the tip surface, permitting examination of successive underlying atom layers⁷².

Thus the field ion microscope can be used advantageously in sputtering studies for several reasons: (1) Individual sputtering events may be examined. (2) Gross damage in the interior of the target crystal, as well as on its surface, may be examined in depth by removing atom layers from the anode tip by field evaporation. (3) The shape and structure of the target surface are known in atomic detail. (4) Since the tip surface is approximately hemispherical in shape, all the crystallographic directions associated with the crystal structure of the target can be viewed in its field ion pattern; by rotating the tip about its axis different crystal faces may be exposed to the bombarding beam. (5) If a beam of neutral atoms is used as the bombarding beam, the surface of the target may be kept absolutely free of extraneous contaminants during bombardment, so that effects due to surface contamination are eliminated. The FIM also has some disadvantages associated with it, the most serious of which is the high value of mechanical stress, due to the electric field, which is exerted on the tip surface; this can affect the apparent results due to bombardment by permitting migration of some types of defects to the surface, and also limits the choice of materials from which targets can be made.

Surprisingly, very little use of the field ion microscope has been made so far in studies of sputtering and radiation damage. The work that has been done in this area has been performed by Müller and Sinha (also by Brandon and Wald)⁷⁴, who have observed surface damage resulting from bombardment of W and Pt tips with 5.4 Mev alpha particles from a polonium source⁷³, with He or A ions of energies between 25 and 300 ev,⁷³ and bombardment of W with 20 kev He or Hg atoms⁷⁵. In their latter study they found that the surface damage due to He atoms consisted of vacancies, interstitials and clusters of these defects, and a disordering of the lattice in about a 50 to 100 Å diameter region, with some of the damage appearing on the side of the tip opposite to the bombarding beam (tip radius of 900 Å). Bombardment by Hg atoms caused even more extensive damage, permitting field evaporation of entire close packed net planes up to 200 Å in diameter.

The objective of the investigation undertaken in this laboratory is to study sputtering of clean tungsten surfaces by xenon ion bombardment, and to relate the information so gained to sputtering problems encountered in cesium ion propulsion systems. Xenon ions are used in this study instead of cesium ions because xenon is easier to handle experimentally; xenon films are nonconductive, and xenon can be pumped out of an evacuated tube easier than cesium. Other studies⁶⁴ have shown that the sputtering yields of xenon and cesium are very nearly equal, so that the results obtained using xenon should be directly applicable to those cases where cesium sputtering occurs.

EXPERIMENTAL TUBE AND TECHNIQUES

Ion Microscope Design

The field ion microscope shown in Figure 33 is the design used for this investigation, and is suitable for field emission microscopy as well. The metal to be studied is etched to a very small radius (ca. 500 Å) in order to obtain the high fields necessary for image formation at reasonable voltages (1-30 kv). The emitter is mounted by spot welding it to a 10 mil tungsten hairpin which, in turn, is inserted into nichrome sleeves for easy replacement. The surrounding cathode is a cone fashioned from 10 mil molybdenum sheet and slips over a protruding portion of a ground glass joint. The tube envelope is fabricated from pyrex glass with a screen diameter of 5 inches and an emitter to screen distance of 10 cm. Before applying the phosphor screen, a conducting layer of tin oxide is formed on the glass surface.

The emitter and the metal cone surrounding the emitter are cooled by a suitable refrigerant, in this case liquid nitrogen. The ions produced at the emitter reach the phosphor screen by passing through a hole in the metal cone.

The tube is evacuated and baked at 400°C for 24 hours resulting in a vacuum of better than 10^{-9} torr. Helium and xenon are then admitted to pressures of 5 and 0.5 microns respectively.

Ion Gun Design

The basic design shown in Figure 34 consists of three basic parts, the electron source, the ionization chamber, and the lens system.

The electron source is a small coil wound from 4 mil tungsten placed 3 mm from the entrance hole to the ionization chamber. This entrance hole has a diameter of 5 mm. The electron beam is collimated through this hole by an external axial magnetic field of 400 gauss. The ions are thus produced in a narrow region in the ionization chamber.

The ionization chamber is simply a molybdenum cylinder 1.7 cm in diameter 3.5 cm long with an extraction electrode at one end. This electrode is a molybdenum disk with a 1 cm diameter hole covered by a tungsten screen which has a transmission of 70%. The tungsten screen prevents the acceleration field from penetrating the ionization chamber.

After passing through the extraction electrode the ions are accelerated to their full energy before entering the Einzel lens system. The first and last lenses are constructed from 1.7 cm diameter molybdenum cylinders, 2 cm long, which have apertures of 8 mm diameter. The center lens is a 1.2 cm diameter cylinder 2 cm long with no aperture. The Einzel lens

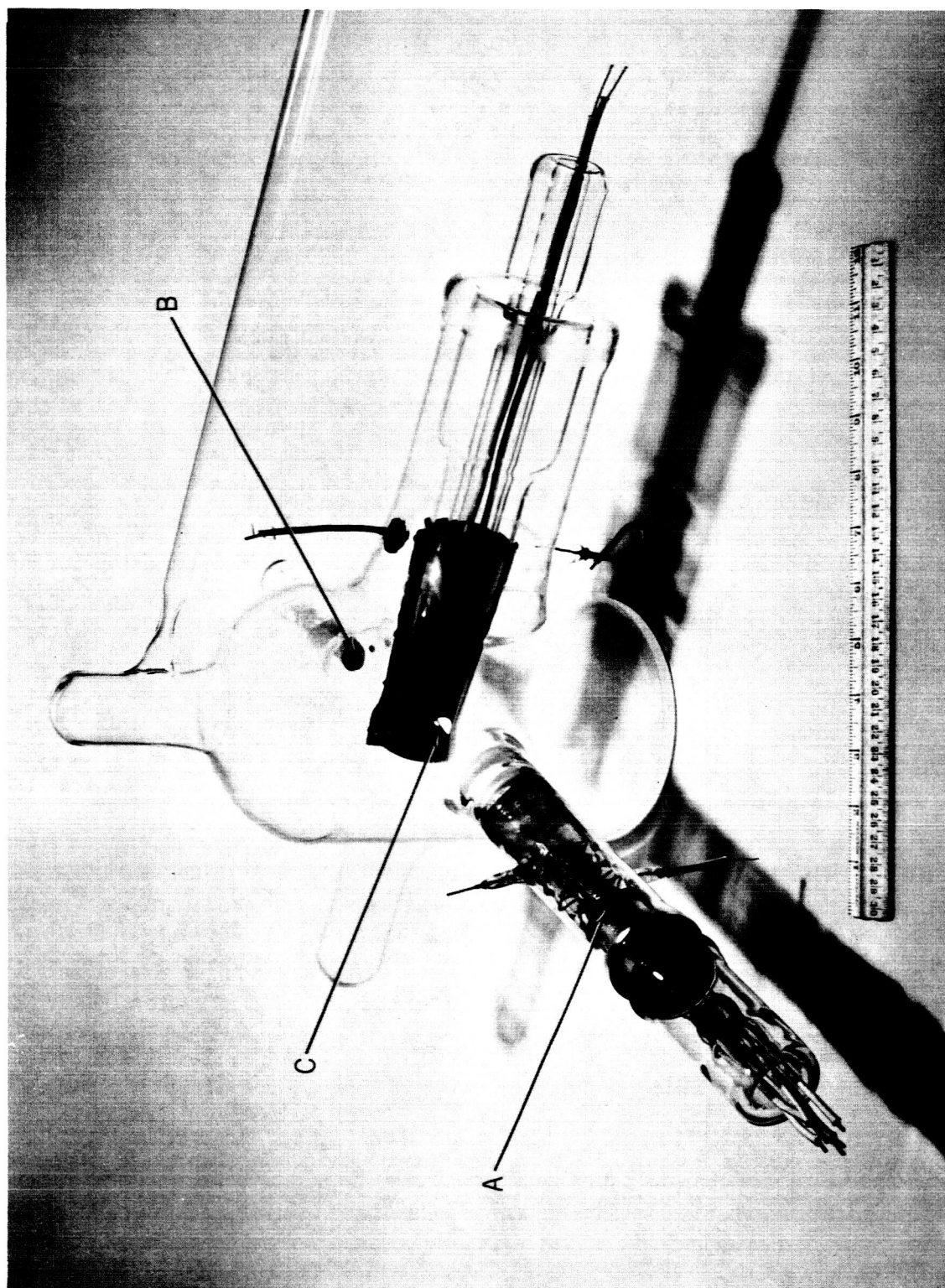


Figure 33. Completed field ion microscope with ion gun. (A) Ion gun, (B) Faraday collector, (C) Emitter.

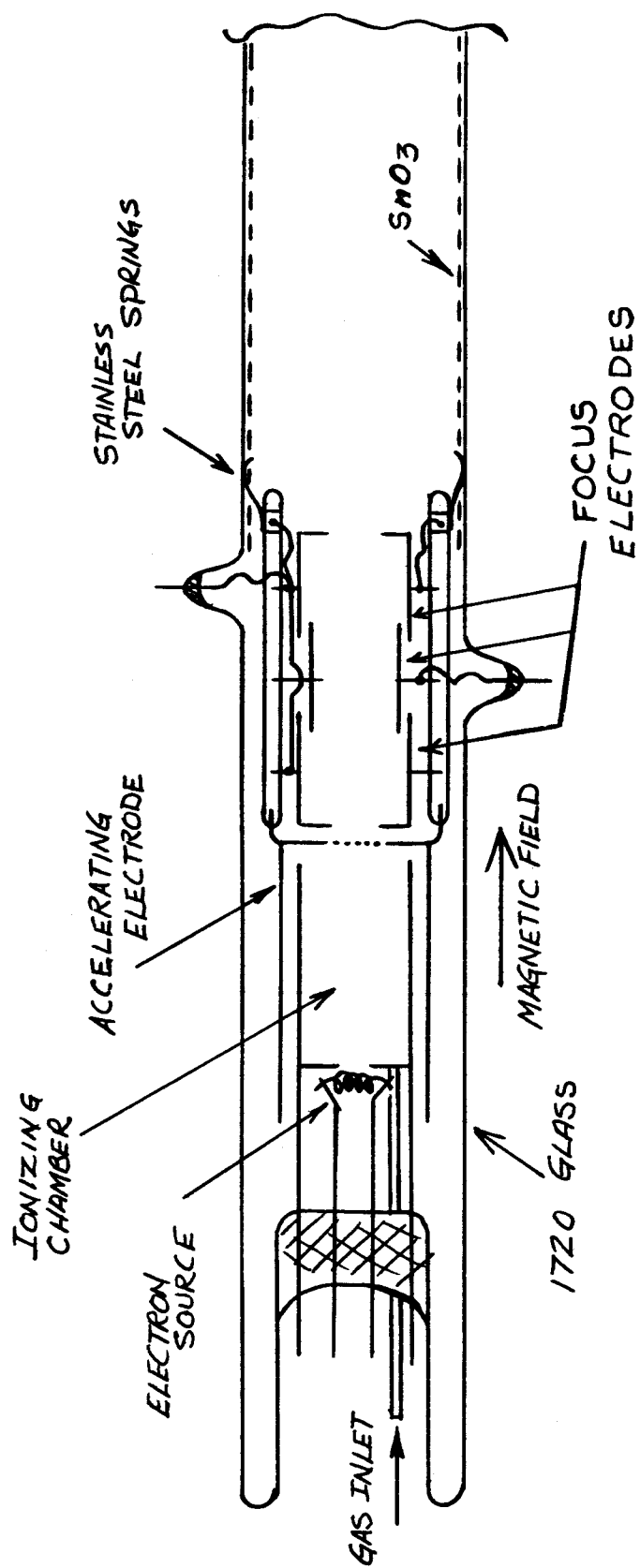


Figure 34. Schematic diagram of xenon ion gun used in xenon ion sputtering studies.

is a zero energy lens; that is, an ion leaves the lens at the same energy it enters.

The ion gun is designed, shown in Figure 35, so as to permit removal of the ion source without disturbing the lens structure.

Procedure

For all experiments reported here the microscope was used as a sealed off tube. The tube contained two gases, helium to form the ion image and xenon for the sputtering study. When the emitter and surrounding mantle were cooled to liquid nitrogen temperatures xenon was adsorbed on them to the extent that no interference in the formation of the helium image was observed. To generate a xenon ion beam the tube temperature was raised to room temperature and the electron energy in the ionization chamber was raised to a value below 12.4 volts to prevent the formation of helium ions. Xenon ion currents up to 10^{-8} amps are obtained at a pressure of 0.5μ . This corresponds to approximately 150 ion impacts per second on the surface visible in the ion image, assuming a beam diameter of 5 mm.

The ion current is collected and measured in a Faraday cup. The current indicated by the Faraday cup is not a true measure of the particle impact on the emitter since the beam also consists of neutrals formed by charge exchange. The cross section for $\text{Xe} \rightarrow \text{Xe}^+$ charge exchange is $5 \times 10^{-15} \text{ cm}^2$ at 1000 ev.⁷⁶ At a xenon pressure of 0.5μ for a beam path of 20 cm calculations show that at the collector 74% of the beam consists of neutral atoms. At the emitter the beam consists of 50% neutrals.

During operation the following procedure was followed. The emitter was heated to a dull red for a few seconds to clean and anneal it. After cooling to liquid nitrogen temperature the emitter was subjected to the process of field evaporation which produces an atomically smooth crystal surface. Field evaporation is brought about by raising the electric field high enough so that the barrier to evaporation is lowered sufficiently to allow evaporation even at liquid nitrogen temperatures. The evaporation is the most rapid over protrusions, where the field is the highest, thus smoothing the surface. The ion image of an atomically smooth and clean emitter is shown in Figure 36.

The anode tip was then bombarded by the xenon beam, with viewing field off for ion bombardment and on for neutral bombardment. The resulting damage was monitored visually, and periodically the xenon beam turned off and a photograph of the current ion pattern was taken. The ion images shown in this report were photographed with an F/1.2 lens on Kodak Spectroscopic Film Type 103-AG, with typical exposure times of about six minutes.

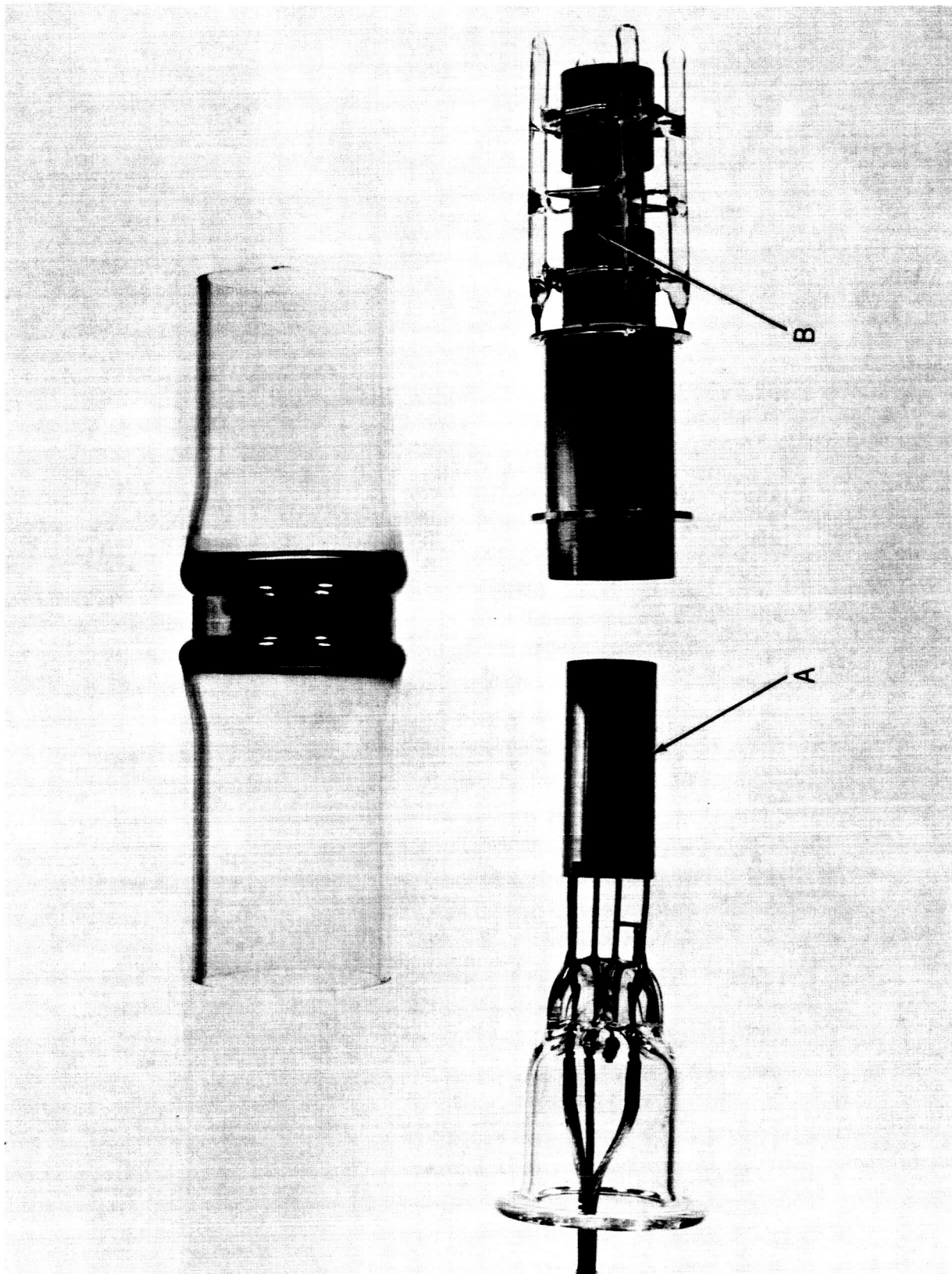


Figure 35. Exploded view of ion gun. (A) Ion source, (B) Einzel lens.

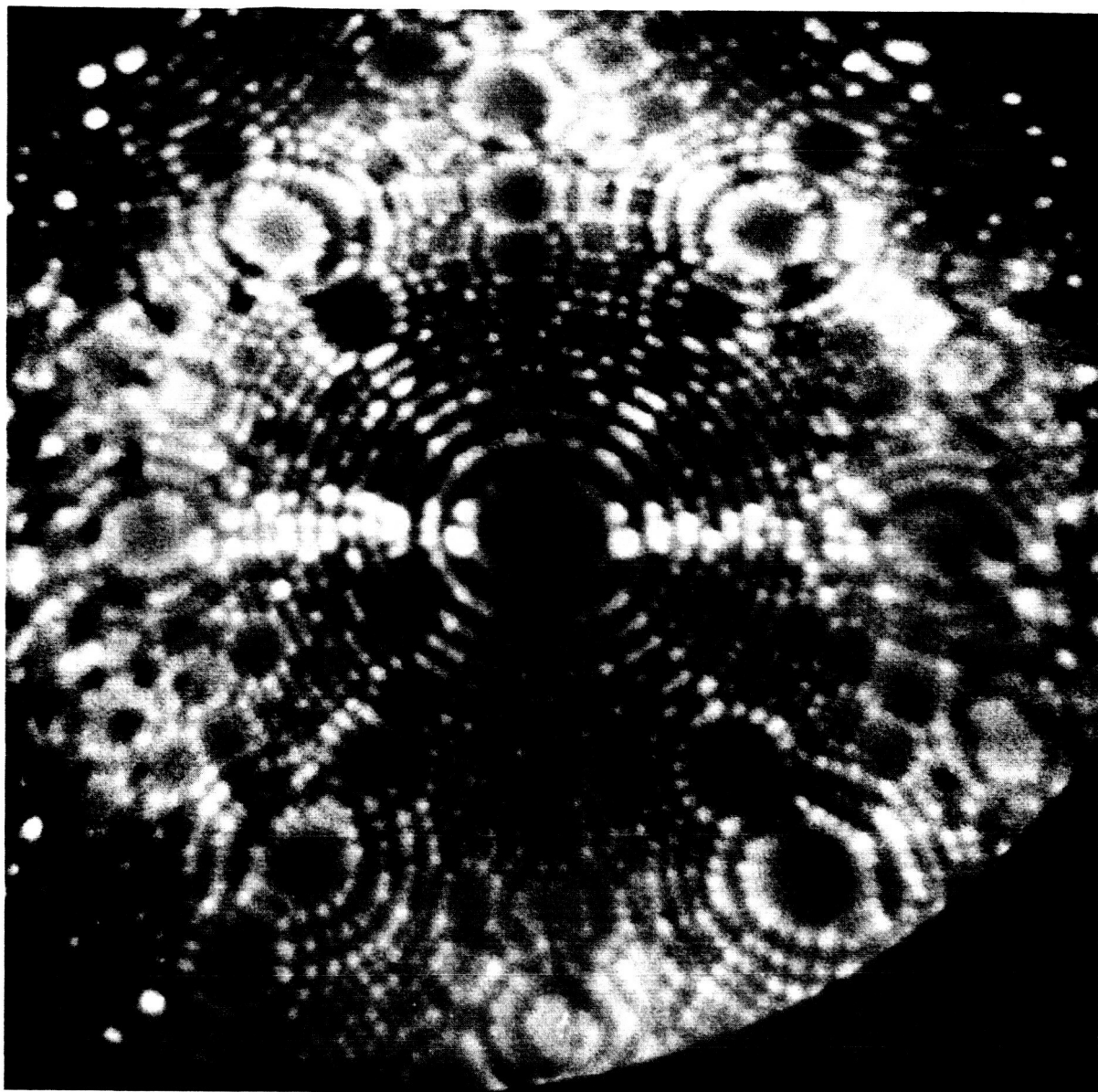


Figure 36. Helium ion image of a field evaporated tungsten emitter.
Voltage 14.85 kv.

PRELIMINARY RESULTS

The results so far are of a qualitative nature; quantitative results are expected later in the program.

Figure 37 was taken after a small amount of ion bombardment followed by field evaporation of approximately one atom layer of tungsten, and shows a few random bright spots in the (110) region that were not visible in the pattern before bombardment (Figure 36). Upon removal of additional atom layers from the surface by field evaporation, these spots disappeared and new spots appeared in new locations, the process repeating as long as field evaporation continued. These spots are believed to be due to xenon atoms buried just beneath the surface and causing a bulge in the uppermost tungsten atom layer (similar interpretations involving interstitial atoms have been made by Müller)⁷³. This would agree with the work of Kornelsen⁶⁹ which indicates that bombarding noble gas ions can be trapped in tungsten to depths of several hundred atom layers.

After heavy ion bombardment and slight field evaporation the pattern in Figure 38 was taken; heavy damage in the $\{111\}$ regions can be seen. Even after field evaporation of more than 30 atom layers the effect of sputtering could still be seen in the $\{111\}$ regions.

Another emitter after heavy ion bombardment is shown in Figure 39 A-D. The energy of the ion beam was 1 kv, and roughly 10^5 impacts were made on the emitter surface visible in the ion pattern. As the voltage was raised to the best image voltage large areas of the emitter surface were seen to be removed rather than individual emitting points, indicating a rather irregular and loosely bound surface. The best image voltage, an indication of emitter curvature, was also 10% lower, which indicates a change in emitter shape. Figure 39-B is after more field evaporation with the surface continuing to leave as large areas. Figure 39-C is after removal of 10 atom layers from the $[111]$ plane. A large amount of damage is visible in the upper lefthand portion of the image and also in the (111) region. Even after removal of 100 atom layers disorder is still evident (Figure 39-D). Damage in the (111) region is probably due to focusing type collisions in the close packed $\langle 111 \rangle$ direction.

The previously mentioned experiments were performed in a rather poor vacuum, 5μ , so that during the sputtering experiments the surface was covered by adsorbed gas. Using the method of maintaining a clean surface by applying a voltage necessary to form a helium image, mentioned previously, sputtering by neutral xenon atoms has been studied. Since the sputtering beam contains about 50% neutrals no difficulties are presented except in the measurement of the flux of these neutrals.

Figure 40 A-D shows the results of sputtering with neutrals with the image field applied to the emitter. Figure 40-A is the ion pattern before

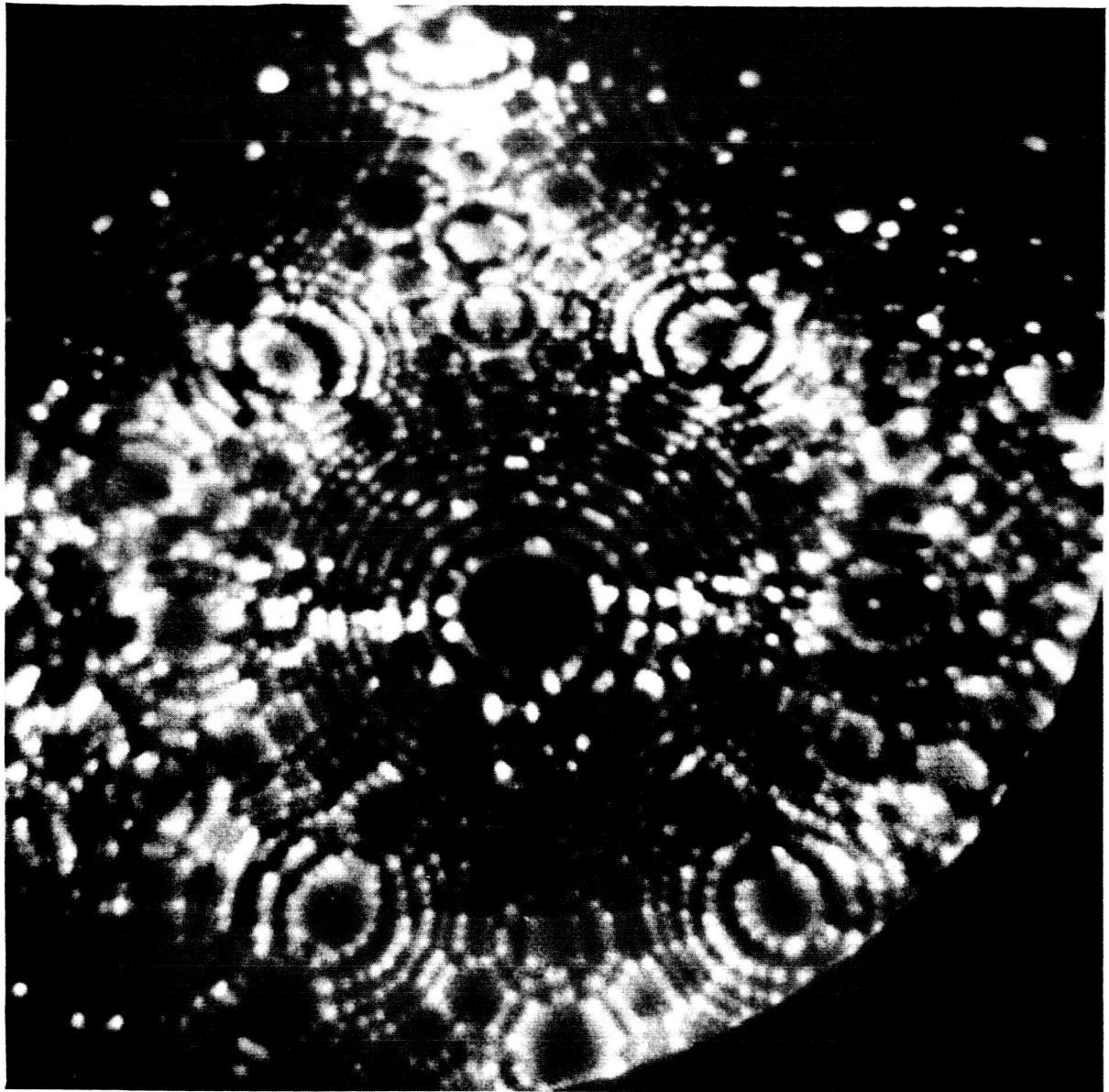


Figure 37. Tungsten emitter after slight xenon sputtering. Voltage 14.85 kv.
Ion beam enters from left.

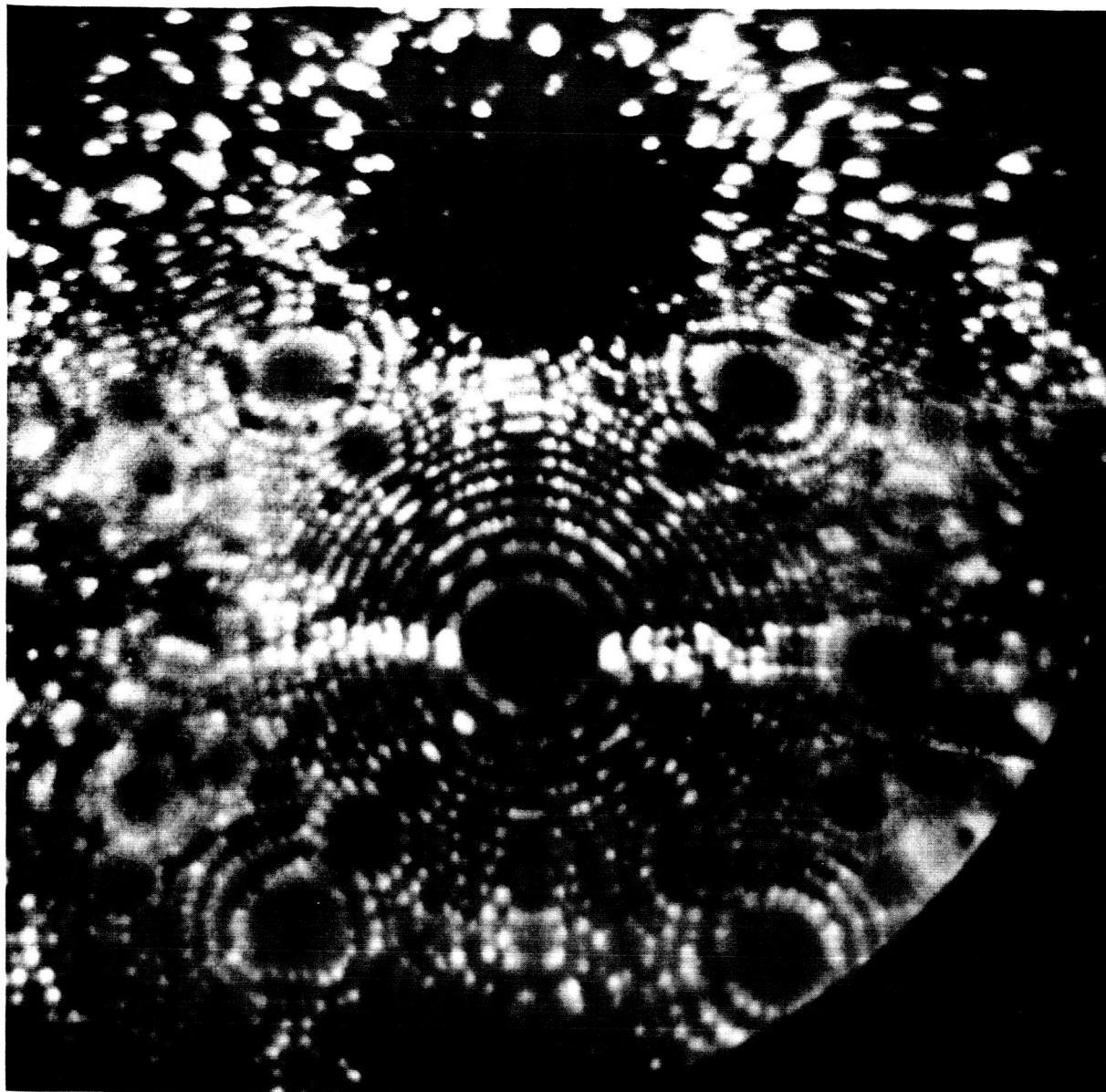
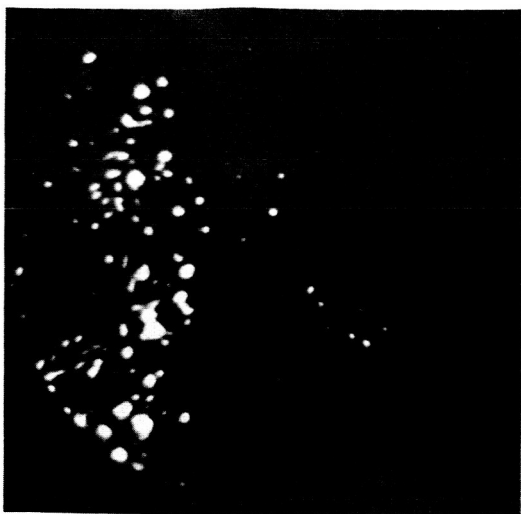
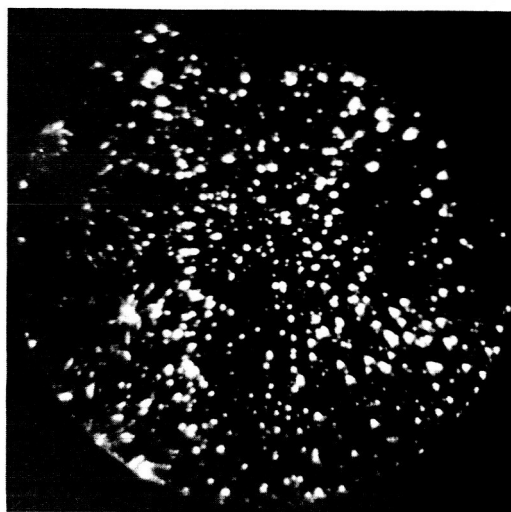


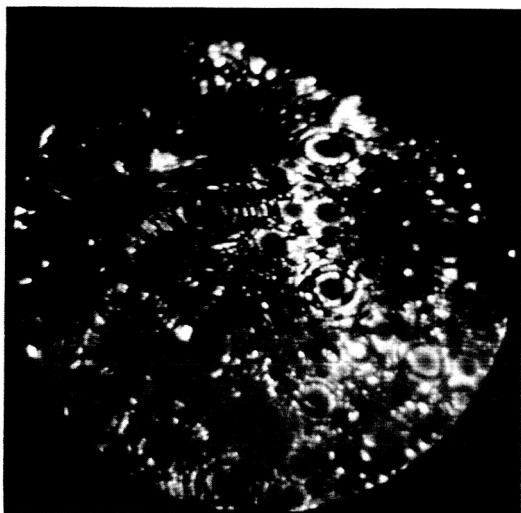
Figure 38. Tungsten image after sputtering with xenon and helium ions with energies to 10 kv, and slight field evaporation. Voltage 13.50 kv. Ion beam enters from left.



A



B

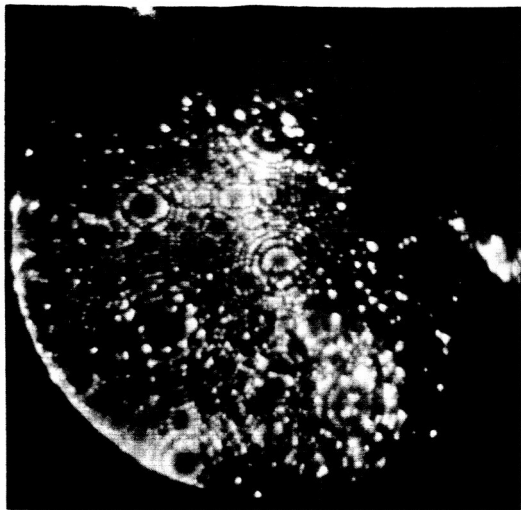


C

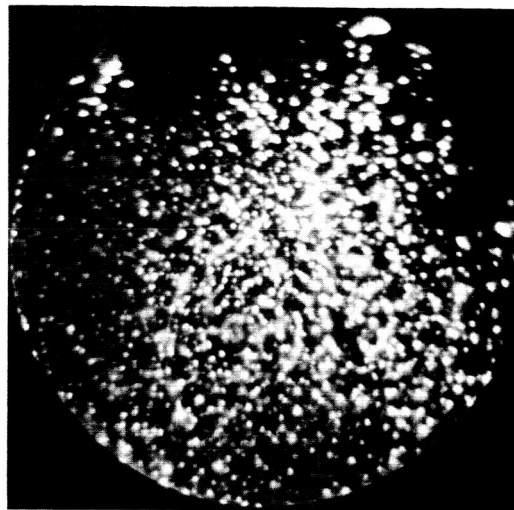


D

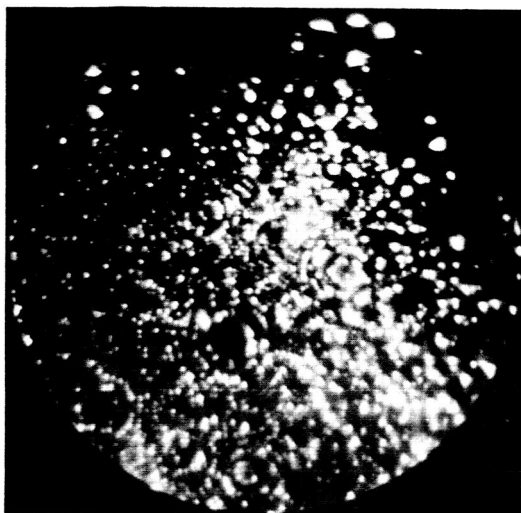
Figure 39. Tungsten image after sputtering, roughly 10^5 impacts at 1 kv energy. (A) Ion image immediately after sputtering. (B) After small amount of field evaporation. (C) Field evaporation of 10 atom layers. (D) After removal of 100 atomic layers. Ion beam enters from left.



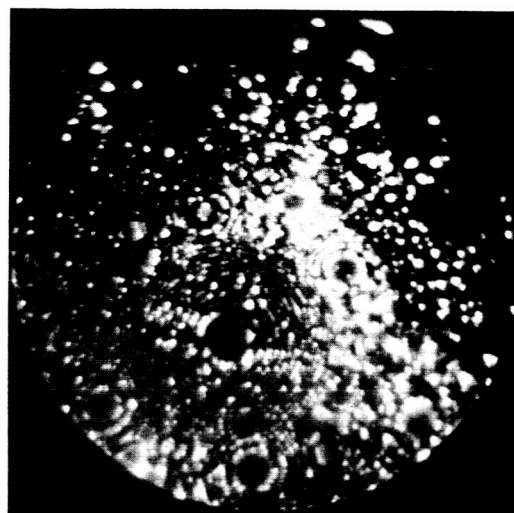
A



B



C



D

Figure 40. Tungsten image after sputtering with neutrals with the image field on. (A) Ion image before sputtering. (B) After roughly 10^3 impacts at 10 kv energy. (C) Field evaporation of 2 atomic layers. (D) Additional 2 layers. Ion beam enters from left.

sputtering. Figure 40-B shows the results of sputtering by neutrals while the image field is applied. About 10^3 impacts were made on the visible area of the emitter at an energy of 10 kv. Figures 40-C and 40-D are after field evaporation of 2 and 4 atom layers respectively. Notice that there is still considerable damage even after 4 atomic layers have been removed. The area toward the beam shows very little regularity. While the side away from the beam is more regular, it still shows many vacancies and interstitials.

CONCLUSIONS

These results show that, for particle energies as low as 1 kev, extensive damage takes place throughout the target crystal even though it is of the order of 1000 Å in diameter. A greater amount of damage seems to appear in the {111} regions than in other regions; this may be due to field evaporation of displaced and thus less tightly bound atoms.

It appears that more information will be gained if sputtering will be limited to a few impacts, 0-50, instead of the several hundred used so that damage from individual impacts may be studied. This will necessitate either sputtering with neutrals or working with high vacuum to maintain a clean surface.

REFERENCES

1. L. W. Swanson, et al, Annual Report, NASA Contract Nr. NASw-458, Field Emission Corp. (1963).
2. R. W. Strayer, et al, Final Report, NASA Contract Nr. NASr-19, Linfield Research Institute (1962).
3. J. B. Taylor and I. Langmuir, Phys. Rev. 44, 423 (1933).
4. R. Gomer, Field Emission and Field Ionization (Harvard University Press, Cambridge, 1961).
5. W. P. Dyke and W. W. Dolan, Adv. in Electronics and Electron Phys. 8, 89 (1956).
6. R. D. Young and E. W. Müller, J. Appl. Phys. 33, 91 (1962).
7. S. T. Martin, Phys. Rev. 56, 947 (1939).
8. E. W. Müller, J. Appl. Phys. 26, 732 (1955).
9. R. Gomer, J. Chem. Phys. 21, 1869 (1953).
10. R. Gomer, Field Emission and Field Ionization, p. 50.
11. J. A. Becker, Phys. Rev. 28, 341 (1926).
12. V. Shrednik, Radio Eng. and Electronics 5, No. 8, 10 (1960). (English Transl.)
13. L. V. Dobretsov, Electron and Ion Emission, NASA Technical Transl. F-73 (1952).
14. R. H. Good and E. W. Müller, Handbuch der Physik 21, 176 (1956).
15. L. W. Swanson and R. Gomer, J. Chem. Phys. 39, 2813 (1963).
16. E. P. Gyftopoulous and J. D. Levine, J. Appl. Phys. 33, 67 (1962).
17. J. Anderson, W. E. Danforth, and A. J. Williams, III, J. Appl. Phys. 34, 2260 (1963).
18. J. R. MacDonald and C. A. Barlow, Jr., J. Chem. Phys. 39, 412 (1963).
19. J. K. Roberts, Some Problems in Adsorption (Cambridge, New York, 1939).

20. A. Gel'berg, et al, Radio Eng. and Electronics 3, No. 8, 32 (1958) (English Transl.)
21. R. C. L. Bosworth, Proc. Roy. Soc. A162, 32 (1937).
22. R. Gomer and L. W. Swanson, J. Chem. Phys. 38, 1613 (1963).
23. R. Gomer and J. K. Hulm, J. Chem. Phys. 27, 1363 (1957).
24. T. H. George and P. M. Stier, J. Chem. Phys. 37, 1935 (1962).
25. F. C. Tomkins, Trans. Farad. Soc. 46, 569 (1950).
26. T. L. Hill, An Introduction to Statistical Thermodynamics (Addison-Wesley Publishing Co., Reading, Mass., 1960).
27. J. Topping, Proc. Roy. Soc. A114, 67 (1927).
28. H. Utsugi and R. Gomer, J. Chem. Phys. 37, 1706 (1962).
29. H. Utsugi and R. Gomer, J. Chem. Phys. 37, 1720 (1962).
30. A. Haumovets, Soviet Phys. -Solid State 5, 1668 (1964) (English Transl.)
31. L. W. Swanson, et al, Report Nr. 1, NASA Contract Nr. NAS3-2596, Field Emission Corp. (3 June 1963 to 30 November 1963).
32. J. P. Barbour, et al, Phys. Rev. 117, 1452 (1960).
33. J. L. Boling and W. W. Dolan, J. Appl. Phys. 29, 556 (1958).
34. W. P. Dyke, et al, J. Appl. Phys. 31, 790 (1960).
35. E. E. Martin and F. M. Charbonnier, Report Nr. 7, ARPA Contract No. DA-36-039 AMC-03266 (E), Field Emission Corp. (15 December 1963 to 15 March 1964).
36. W. P. Dyke, et al, Phys. Rev. 91, 1043 (1953).
37. W. W. Dolan, W. P. Dyke, and J. K. Trolan, Phys. Rev. 91, 1054 (1953).
38. D. J. DeGeeter, J. Appl. Phys. 34, 919 (1963).
39. E. M. Lyman, F. Konrad, and T. Casale, Coordinated Science Laboratory Progress Report, University of Illinois, 48 (December 1962 to February 1963).
40. H. Boersch, C. Radloff, and G. Sauerbrey, Z. Physik 165, 464 (1961).

41. J. E. Lilienfeld, Physik Z. 20, 280 (1919).
42. I. Frank and V. Ginsburg, J. Phys. (USSR) 9, 353 (1945).
43. G. Beck, Phys. Rev. 74, 795 (1948).
44. R. A. Ferrell, Phys. Rev. 111, 1214 (1958).
45. R. H. Ritchie and H. B. Eldridge, Phys. Rev. 126, 1935 (1962).
46. E. A. Stern, Phys. Rev. Letters 8, 7 (1962).
47. A. L. Frank, E. T. Arakawa, and R. D. Birkhoff, Phys. Rev. 126, 1947 (1962).
48. W. Steinmann, Phys. Rev. Letters 5, 470 (1960).
49. R. W. Brown, P. Wessel, and E. P. Trownson, Phys. Rev. Letters 5, 472 (1960).
50. W. R. Hunter, J. Opt. Soc. Am. 54, 208 (1964).
51. J. P. Waldron and D. W. Juenker, J. Opt. Soc. Am. 54, 204 (1964).
52. D. W. Juenker, J. P. Waldron, and R. J. Jaccodine, J. Opt. Soc. Am. 54, 216 (1964).
53. R. P. Little and W. T. Whitney, J. Appl. Phys. 34, 3141 (1963).
54. H. E. Tomaschke, Coordinated Science Laboratory Report R-192, University of Illinois (January 1964).
55. P. C. Bettler and F. M. Charbonnier, Phys. Rev. 119, 85 (1960).
56. E. Kay, Adv. in Electronics and Electron Phys. 17, 245 (1962).
57. G. K. Wehner, 1961 Trans. 8th Natl. Vacuum Symposium, 239 (1962).
58. N. Schwartz, 1963 Trans. 10th Natl. Vacuum Symposium, 325 (1963).
59. S. P. Wolsky, 1963 Trans. 10th Natl. Vacuum Symposium, 309 (1963).
60. C. H. Townes, Phys. Rev. 65, 319 (1944).
61. J. Stark, Z. Elektrochem. 14, 752 (1908); 15, 509 (1909).
62. W. J. Moore, Am. Scientist 48, 109 (1960).

63. G. K. Wehner, J. Appl. Phys. 26, 1056 (1955).
64. O. Almèn and G. Bruce, Nucl. Inst. and Methods 2, 257 (1961)
65. G. D. Magnuson, Report Nr. 1, NASA Contract Nr. NAS3-2591, General Dynamics Space Science Lab. (20 October 1963).
66. N. Bohr, Kgl. Danske Videnskab Selskab. Mat. -Fys. Medd. 18, No. 8 (1948).
67. R. H. Silsbee, J. Appl. Phys. 28, 1246 (1957).
68. G. Leibfried, J. Appl. Phys. 31, 117 and 1046 (1960).
69. E. V. Kornelsen, Can. J. Phys. 42, 364 (1964).
70. G. S. Anderson and G. K. Wehner, J. Appl. Phys. 31, 2305 (1960).
71. E. W. Müller, Z. Physik 131, 136 (1951).
72. E. W. Müller, Adv. in Electronics and Electron Phys. 13, 83 (1960).
73. E. W. Müller, Direct Observations of Imperfections in Crystals, ed. by J. B. Newkirk and J. W. Wernick (Interscience Publishers, New York, 1962), 77.
74. D. G. Brandon and M. Wald, Phil. Mag. 6, 1035 (1961).
75. M. K. Sinha and E. W. Müller, J. Appl. Phys. 35, 1256 (1964).
76. J. W. Sheldon, Phys. Rev. Letters 8, 64 (1962).

APPENDIX I

SOURCE OF MOVEMENT OF SPHERICAL ELECTRODE

It has been shown previously¹ that the electrostatic stress needed to account for an elongation of the filament that would result in the observed rise in current at constant voltage would be much greater than the force produced by the maximum applied gross field. If, however, the ball and its supporting structure are not perpendicular, but are inclined slightly with respect to the plane as shown in Figure 41-a much less force is required to pull this structure into the perpendicular position, thus bringing the ball closer to the plane and decreasing the gap.

Assuming the stress forces are responsible for the initial displacement that leads to oscillation, the lateral displacement should be:

$$z = \frac{f_s L^2}{G \omega_o^2} \quad (\text{I-1})$$

where: f_s is the force between a plane and a grounded sphere

L is the length of the supporting filament

G is the moment of inertia with respect to an axis parallel to the plane and passing through the pivot point 0 in the figure

ω_o is the angular frequency of oscillation.

Using the computed value of G , the measured values of f_s , ω_o , and L , a value of z can be found. This can be compared with a value derived from the known change in gap current. Assuming the change in I is due to a change in β at a constant voltage, equation (7) can be differentiated to give

$$\frac{\Delta\beta}{\beta} = \frac{\Delta I}{I} \frac{\beta V}{b_1 \phi^{3/2}}$$

It has been shown¹ that β is related to the enhancement factor γ , which is independent of gap spacing, by $\beta d = \gamma$. Differentiating this, a change in gap spacing $\Delta d = \frac{d}{\beta} \Delta\beta$. From strictly geometrical considerations, it can be seen from the figure that if z is small compared with L , z can be expressed as:

$$z = \sqrt{2L\Delta d} \quad (\text{I-2})$$

At a gap spacing of 2.5 mils, a value of z computed using equation (I-1) was found to be 1.78×10^{-2} cm. while the value of z computed from

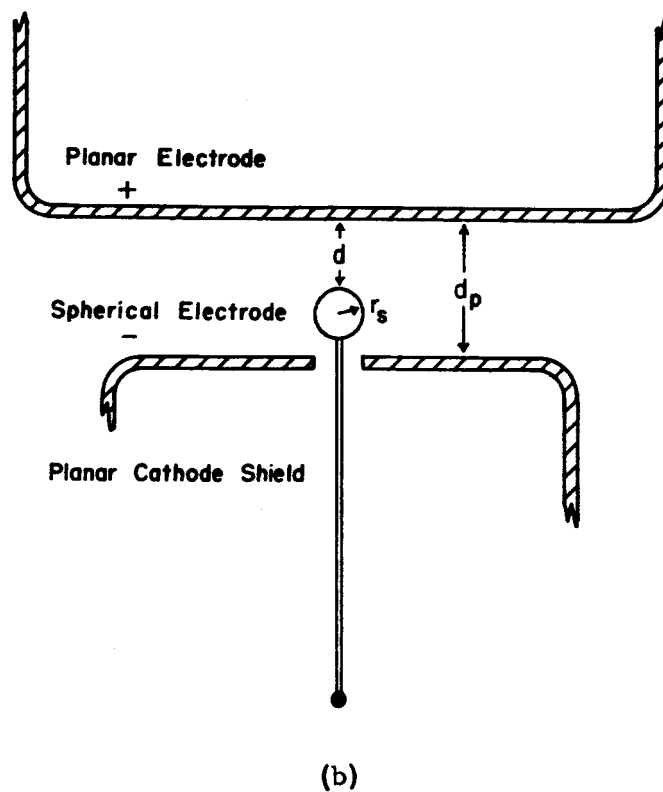
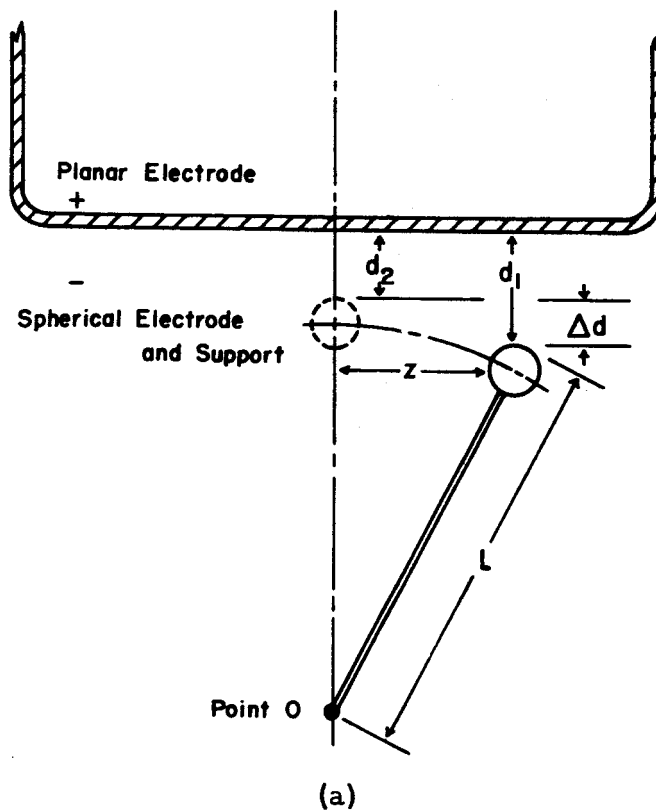


Figure 41. a) Cutaway view of tungsten electrode voltage breakdown tube showing, in exaggerated form, the initial position of the spherical electrode (solid line) and the position (dotted line) after movement.
b) Cutaway view of molybdenum tube.

equation (I-2) was found to be 2.8×10^{-2} cm. It seems plausible that the electrostatic forces acting on slightly non-symmetrical electrodes could account for a change in gap spacing which could lead to oscillatory motion as well as to instabilities in the I-V characteristics of the system.

APPENDIX II

SOURCE OF MOVEMENT OF PLANAR ELECTRODE

There are three forces due to electrostatic stresses acting on the planar electrode, one due to the electric field between the spherical electrode and the planar electrode, f_s , one due to the field between the planar cathode shield and the planar electrode, f_p , and one due to the field between emitting protrusions and the planar electrode.

The total force acting upon the planar electrode may be obtained by integrating the electric field stress over the areas of each part of the cathode structure and adding the resulting forces. Despite the high field, at the protrusion tips, the corresponding force is negligible, compared to the others, because the area over which it acts is extremely small.

Because of the very large area of the planar cathode shield, the dominant force will be f_p , which is given by, (in rationalized MKS units),

$$f_p = \frac{\epsilon_o V^2}{2 d_p^2} S_p \quad (\text{II-1})$$

where V is the applied voltage, d_p is the separation between planes as shown in Figure 41-b, and S_p is the area of the cathode shield. Since the distance d between sphere and plane is much smaller than the distance d_p even at maximum gap spacing, there will also be a contribution to the total force due to the field between the sphere and the plane despite the much smaller size of the sphere. For the case of a sphere and a plane the force is*

$$f_s = 2\pi \epsilon_o r_s^2 V^2 \left[\frac{1}{2(r_s+d)^2} + \frac{8 r_s (r_s+d)}{[4(r_s+d)^2 - r_s^2]^2} \right] \quad (\text{II-2})$$

where V is the applied voltage in volts, r_s is the radius of the sphere, d is the distance from the top of the sphere to the plane and ϵ_o is the permittivity.

A sample calculation using the experimentally measured values of V and d at which the planar electrode was seen to move towards gap closure will illustrate the magnitude of these forces. For the following values of the constants and variables,

*William R. Smythe, Static and Dynamic Electricity, 2nd Ed. (McGraw-Hill Book Company, Inc., New York, Toronto, London, 1950), p. 121.

$$V = 16.7 \text{ kv}$$

$$d = 10 \text{ mils}$$

$$r_s = 15 \text{ mils}$$

$$d_p = 50 \text{ mils}$$

$$\epsilon_o = 8.85 \times 10^{-12} \text{ (in MKS units)}$$

the values for f_p and f_s which add to give the total force can be expressed in grams as:

$$f_p + f_s = 7.80 \text{ gm} + 0.49 \text{ gm} = 8.26 \text{ gm} \quad (\text{II-3})$$

An effective spring constant was determined by suspending weights from the planar electrode of a similar tube and found to be 41 gm/mil. Using this value for the spring constant, the above force would move the electrode 0.2 mils, or cause a 2% change in d which will be monitored as a 22% change in emission current. The change in d will increase the force, and lead to a regenerative process if Δd is greater than some critical value (about .2 mils for the above values of V and d_p).

APPENDIX III

LIST OF SYMBOLS

<u>Page first Introduced</u>	<u>Symbol</u>	<u>Meaning</u>
82	A_o	surface atom density
26	A	intercept with vertical axis at $10^4/v = 0$ in a Fowler-Nordheim plot
27	A_s	Fowler-Nordheim intercept A for a clean surface
11	a	site-to-site separation for diffusion
26	B	a pre-exponential constant in the Fowler- Nordheim equation whose value depends upon geometry alone
26	b	a constant, with value 6.8×10^7 v/cm(ev) ^{3/2} , which appears in the Fowler-Nordheim equation
78	C	a constant defined by equation (57)
80	c	velocity of light (3×10^{10} cm/sec)
26	c_o	ratio of electric field at the equilibrium distance x_o of the ad-atom to the applied field F
49	c_1	equivalent fraction of an ad-atom's neighbors involved in a van der Waal's interaction
50	D	diffusion coefficient
45	D_o	diffusivity
77	d	inter-electrode spacing
108	d_p	distance from planar electrode to planar cathode shield
56	E	activation energy

Page first Introduced	Symbol	Meaning
10	E_a	activation energy for neutral desorption
50	E_b	heat of vaporization of cesium
10	E_d	activation energy for surface diffusion
33	E_p	activation energy for ion desorption
36	e	charge of an electron
19	F	applied field
25	F_o	applied field evaluated at x_o
71	F_{av}	average electric field on the surface of an electrode
65	F_s	applied field evaluated at x_s
50	$F_d(\theta, T)$	a complicated dimensionless function which multiplies the diffusion coefficient
47	f	two-dimensional spreading pressure
108	f_p	force due to electrostatic stress between planes
105	f_s	force due to electrostatic stress between sphere and plane
105	G	moment of inertia
77	H	half width of base of protrusion
77	h	height of protrusion
46	h'	Planck's constant (6.62×10^{-27} erg-sec)
10	I	current
80	i	$\sqrt{-1}$
77	J	current density
49	J_d	two-dimensional atom flux

<u>Page first Introduced</u>	<u>Symbol</u>	<u>Meaning</u>
76	J_{\max}	maximum current density before a tip is resistively heated to its melting point
11	k	Boltzmann's constant (8.62×10^{-5} eV/ $^{\circ}$ K)
58	k_p	rate constant for field desorption
27	$k(x, \sigma)$	a dimensionless factor, with values between 0 and 1, which accounts for the discreteness of an adsorbed layer of dipoles.
105	L	length of spherical electrode and its support
26	\ln	natural logarithm
5	\log	base 10 logarithm
46	M	atomic weight of cesium
5	m	slope of Fowler-Nordheim plot
5	m_s	slope of Fowler-Nordheim plot for clean surface
46	N	number of ad-atoms in the system whose partition function is Q
48	N_o	number of sites available for adsorption
48	\overline{N}_{11}	average number of nearest neighbors
78	n	number of photons
31	$P(T)$	T-F enhancement factor (relative increase in field emission current due to temperature T)
31	p	a complicated function of T , F , and ϕ , approximated by $9.3 \times 10^3 T \frac{\phi^{1/2}}{F}$, T in degK, ϕ in eV, F in v/cm.
46	Q	canonical partition function for a system of ad-atoms
46	q	single particle partition function

<u>Page first Introduced</u>	<u>Symbol</u>	<u>Meaning</u>
11	R	cesium dosage (amount of cesium crossing a plane normal to the cesium beam)
6	r	apex radius of emitting tip
108	r_s	radius of spherical electrode
108	S_p	surface area of cathode shield
46	S	surface area
46	S_o	total area occupied by N_o ad-atoms
46	S_f	free surface area
82	S_t	surface tension of protrusion material
58	s	a complicated function involving transition probabilities and/or entropy effects
11	T	temperature
34	t	time
26	$t(\emptyset, F),$ $v(\emptyset, F)$	tabulated functions in the Fowler-Nordheim equation, taking into account image corrections
10	V	applied voltage
34	V_I	ionization potential of the adsorbate
80	v	electron velocity
47	v_d	ad-atom two-dimensional velocity
47	w	intermolecular potential energy which a given ad-atom experiences
48	w_1	pair-wise mutual potential energy of nearest neighbors
48	w_a	attractive potential energy term involving dispersion forces

Page first Introduced	Symbol	Meaning
55	w_F	change in ad-atom potential energy due to applied field F
48	w_r	potential energy term due to Coulomb repulsion of adjacent dipoles
27	x	distance normal to the surface
25	x_o	equilibrium distance from the surface
62	x_c	distance from the surface at which ionic desorption and neutral desorption curves intersect
36	x_p	equilibrium bond distance of the adsorbate
64	x_s	distance of the Schottky saddle from the surface
82	dx/dt	change in protrusion length
11	y	diffusion distance on the surface
78	Z	atomic number
105	z	lateral displacement from plane normal of the spherical electrode
19	a	ad-atom polarizability
65	a_a	polarizability of atomic state
11	a_c	interior half angle of emitter cone
78	a_f	fine structure constant
65	a_i	polarizability of ionic state
5	β	geometric ratio of electric field F at the surface to the applied voltage V
78	β_r	ratio of electron velocity v to the velocity of light c
71	γ	electric field enhancement factor due to surface roughness

<u>Page first Introduced</u>	<u>Symbol</u>	<u>Meaning</u>
78	δ	angular separation from foil normal
108	ϵ_0	permittivity in vacuum
80	ϵ	complex dielectric constant
80	ϵ_1, ϵ_2	real and imaginary parts of ϵ respectively
47	θ	ratio of δ to δ_m
80	λ	radiation wavelength
46	λ_a	wavelength of vibrating ad-atom
80	λ_p	wavelength corresponding to plasma frequency ω_p
19	μ	effective dipole moment of the adsorbate
29	μ_0	dipole moment at zero coverage
49	μ_s	chemical potential of the adsorbed layer
34	ν	vibrational frequency of adsorbed atoms
6	σ	adsorbate surface density
25	σ_0	monolayer coverage of adsorbate
14	σ_∞	the highest adsorbate surface density investigated
40	σ_c	coverage at which the work function of the surface is equal to the ionization potential of cesium
14	σ_m	adsorbate surface density for which the change in work function is maximum
53	σ_s	adsorbate surface density on the emitter shank
53	σ_t	adsorbate surface density on the emitter tip

Page first Introduced	Symbol	Meaning
47	τ_g	time required for an ad-atom to travel one lattice-site distance a for a freely mobile two-dimensional gas
45	τ_s	time required for an ad-atom to travel one lattice-site distance a for a localized ad-layer of restricted mobility
5	ϕ	work function
19	ϕ_{100}	work function of the (100) plane
19	ϕ_{110}	work function of the (110) plane
14	ϕ_{av}	average work function
5	ϕ_c	work function at x_c
14	ϕ_m	minimum value of the work function
38	ϕ_{ow}	work function of oxygen-covered tungsten
5	ϕ_s	average clean substrate work function
78	\cap	$\cos \delta$
82	Ω_o	atomic volume
78	ω	frequency of emitted radiation
105	ω_o	frequency of oscillation of the electrode
80	ω_p	angular frequency of free electron plasma in metal

Superscripts:

o	no applied field
F	applied field F